

**DEVELOPING NEW TECHNIQUES TO SYNTHESIZE  
LAYERED CATHODE MATERIALS FOR LITHIUM-ION  
BATTERIES**

---

A Dissertation presented to  
the Faculty of the Graduate School  
University of Missouri

---

In Partial Fulfillment  
Of the Requirements for the Degree  
Doctor of Philosophy

---

by

**KHALEEL IDAN HAMAD**

Prof. Yangchuan Xing, Dissertation Supervisor

JULY, 2019

The undersigned, appointed by the Dean of the Graduate School, have examined  
the dissertation entitled:

**DEVELOPING NEW TECHNIQUES TO SYNTHESIZE  
LAYERED CATHODE MATERIALS FOR LITHIUM-ION  
BATTERIES**

Presented by

Khaleel Idan Hamad

a candidate for the degree of Doctor of Philosophy

and hereby certify that in their opinion it is worthy of acceptance.

---

Prof. Yangchuan Xing

---

Prof. David Retzloff

---

Prof. Zheng Yan

---

Prof. Jian Lin

## **DEDICATION**

I dedicate this work to my parents, Idan Hamad and Hasnah Hamdan, for inspiring me to dream about education to the highest level and to my wife, Kawther, for helping me make it come true.

## ACKNOWLEDGMENTS

Throughout my life and certainly during the time of my Ph.D. study at the University of Missouri-Columbia, I have had the privilege of working with supportive and resourceful individuals who have been an essential component to my success. Only through their guidance and support did I achieve my goals and attain the personal and professional progress for which I had aspired.

I would like to express my deep gratitude to Prof. Yangchuan Xing, my research advisor, for his patient guidance, enthusiastic encouragement, useful critiques of this research work, advice, and assistance in keeping my progress on schedule. I would also like to thank my committee members, Prof. David Retzloff, Prof. Zheng Yan, and Prof. Jian Lin, for their useful suggestions that improved my research. I appreciate the time they spent to revise the dissertation.

My thanks are also extended to Dr. Jinyun Liao for his help in giving me some general thoughts on my research, and to Prof. Saba Ghani, who encouraged me to do my best and never stop.

Thanks are also due to my sponsor and the hardworking staff at the “The Higher Committee for Education Development in Iraq (HCED)”, for providing the financial support during all the stages of my Ph.D. mission. Without their help, this work would not be possible.

I must express my gratitude to my wonderful family members, especially my fabulous father, **Idan Hamad Khalaf**, who was the light in my life. He dedicated all his life for us to be successful. Unfortunately, he passed away on November 27, 2017, before seeing me reach the goal of which he would be proud. I pray to my Lord to grant him Paradise and reward him the best (miss you so much dad). He and my mother, in Iraq, have, from great distance, been the unwavering support I have needed throughout this

challenging and rigorous program. I really appreciate the sacrifices they have made to fulfill my dreams in this life's journey. I am most grateful to them. I am grateful to my siblings, who have provided me moral and emotional support in my life. I am also grateful to my other family members and friends who have supported me along the way. Special thanks go to my life partner and wife, Kawther, who supported me in every way possible, starting from the first day of my mission which lasted five years far away from my country. She has encouraged and helped me where required to overcome all the obstacles during the years preceding graduation. I would also like to deeply thank my handsome sons, Osamah and Salman, and my lovely, beautiful daughters, Maryam and Rawan, for being with me, cheering me during my difficulties.

Finally, I extend thanks to all the faculty and staff of the department of chemical engineering at MU and the university at large.

## **Table of Contents**

ACKNOWLEDGMENTS .....	ii
List of Figures .....	viii
List of Tables .....	xii
Abstract .....	xiii
Chapter 1. Introduction .....	1
1.1 Overview .....	1
1.2 Lithium-ion battery components and working mechanism.....	3
1.2 Transition metal oxide.....	5
1.3 $\text{Li}_x\text{M}_y\text{O}_2$ (M=Mn, Co, Ni) developments .....	7
1.4 Lithium-ion batteries synthesis methods.....	12
1.5 Sol-gel synthesis method.....	14
1.6 Research Objectives .....	16
Chapter 2. Synthesis of layered $\text{LiMn}_{1/3}\text{Ni}_{1/3}\text{Co}_{1/3}\text{O}_2$ oxides for Li-ion batteries using biomass glycerol as solvent .....	20
2.1 Abstract .....	20
2.2 Introduction .....	21
2.3 Experimental Section .....	23
2.3.1 Powder synthesis .....	23
2.3.2 Materials Characterization.....	24
2.3.3 Electrode preparation and electrochemical characterization.....	24

2.4 Results and Discussion.....	25
2.4.1 ICP-MS analysis .....	25
2.4.2 Powder characterization .....	26
2.4.3 Particle size and morphology .....	28
2.5 Conclusions .....	38
2.6 Acknowledgements .....	39
 Chapter 3. The Effect of Cobalt and Nickel Contents on the Performance of Lithium Rich Positive Electrode Materials for Lithium-Ion Battery.....	 40
3.1 Abstract .....	40
3.2. Introduction .....	41
3.3. Experimental .....	43
3.3.1. Powder synthesis .....	43
3.3.2. Materials characterization.....	44
3.3.3. Electrochemical measurements .....	44
3.4. Results and discussion.....	45
3.4.1. ICP-MS analysis .....	45
3.4.2. Material characterization .....	46
3.4.3. Morphology characterization.....	48
3.4.4. Electrochemical characterizations .....	49
3.5. Conclusions .....	57
3.6 Acknowledgements .....	58

Chapter 4. Manganese-Based Li-rich Cathode Materials Prepared Using Precursor Salts with Acetate and Nitrate Anions.....	59
4.1 Abstract .....	59
4.2 Introduction .....	59
4.3 Experimental section .....	62
4.4 Results and discussion.....	64
4.4.1 Thermal analysis - TGA. ....	66
4.4.2 Materials Morphology .....	69
4.4.3 Phase analysis-XRD .....	70
4.4.4 Electrochemical characterizations .....	72
4.5 Conclusion.....	80
Chapter 5. High Retention-Rate NCA Cathode Material Synthesized Using Glycerol Solvent .....	81
5.1 Abstract .....	81
5.2 Introduction .....	81
5.3 Experimental .....	82
5.4 Results and discussion.....	83
5.5 Summary .....	89
5.6 Acknowledgements .....	89
Chapter 6. Conclusions and future work.....	90
6.1 Conclusions .....	90



6.2 Future Work .....	92
Bibliography .....	94
VITA.....	105

## **List of Figures**

Figure 1.1 Comparison between volumetric and specific energy densities for rechargeable batteries [4].	2
Figure 1. 2 The availability of metals as a fraction of Earth's crust with the prices for 5 years [3].	3
Figure 1. 3 The hierarchical structure of lithium-ion batteries [8].	4
Figure 1. 4 Charge- Discharge mechanism for lithium-ion batteries [9].	5
Figure 1. 5 Comparison of lithium-ion battery cathode materials in 2015 and 2025 [16].	6
Figure 1. 6 Electrode material for lithium-ion battery [17].	7
Figure 1. 7 Discharge profile of different lithium-ion batteries [3].	7
Figure 1. 8 Chronological evolution of the layered oxide LiCoO <sub>2</sub> chemistry fueled by cationic substitution within the metal layers (left) with i) partial replacement of Co with Ni and Mn (NMC phase) within the metal layer (purple) and ii) more recently with Li (yellow) to form Li-rich NMC phases [18].	8
Figure 1. 9 Comparison of ionic radii of alkaline species and TM ions in their stable valence states at synthesis operating temperatures and their influence on the 2D layered characters of AMO <sub>2</sub> phases. Dashed red rectangle shows ions leading to strictly 2D layered LiMO <sub>2</sub> structure and the partial cation mixing due to Ni reduction is schematically represented [18].	9
Figure 1. 10 A map of relationship discharges capacity (black), thermal stability (blue) and capacity retention (red) of Li/Li[Ni <sub>x</sub> Co <sub>y</sub> Mn <sub>z</sub> ]O <sub>2</sub> compounds with number in brackets corresponding to the composition (Ni Mn Co) [18,24].	11

Figure 1. 11 Structural representation of (a) O3-type layered oxides; (b) the overall cell of Li-rich layered oxides described as monoclinic and (c) M / Li ordering within LiM2 layer [18].	11
Figure 1. 12 Different synthesis techniques utilized to produce cathode Materials [27].	14
Figure 1. 13 Sol-Gel process [34].	16
Figure 1. 14 Schematic diagrams of the sol-gel technique to produce nanoparticles as a cathode material for lithium ion batteries.	19
Figure 2.1 XRD patterns of LMNC1, LMNC2, LMNC3, and LMNC4 material synthesized using the sol-gel method using glycerol as a solvent and cornstarch as gelling agent for temperatures (a) 10–85°, (b) 37–39°, and (c) 64–66°.	27
Figure 2.2 SEM images of (a) LMNC1, (b) LMNC2, (c) LMNC3, and (d) LMNC4 compounds, showing different particle sizes.	29
Figure 2.3 Particle size distributions of (a) LMNC1, (b) LMNC2, (c) LMNC3, and (d) LMNC4 compounds.	30
Figure 2.4 Voltage profile of (a) LMNC1, (b) LMNC2, (c) LMNC3, and (d) LMNC4 at initial, 10th and 100th cycles and current density C/10 with a potential range between 2.5 and 4.6V.	31
Figure 2.5 (a) Rate capability behavior of LMNC1, LMNC2, LMNC3, and LMNC4, (b) Discharge behavior of LMNC1, LMNC2, LMNC3, and LMNC4 cathodes (C/10 rate).	33
Figure 2.6 CV curves of (a) LMNC1, (b) LMNC2, (c) LMNC3, and (d) LMNC4 electrodes, with a potential range 2.5 - 4.6 V.	35

Figure 2.7 Impedance plots of LMNC1, LMNC2, LMNC3, and LMNC4 electrodes before the 1st cycle (a), after 10 cycles (b), and after 100 cycles (c), respectively. ....	37
Figure 3.1 XRD patterns of as prepared LR1 and LR2 cathode materials.....	47
Figure 3.2 SEM images of LR1 and LR2 at different magnifications.....	49
Figure 3.3 The initial, 30 <sup>th</sup> and 60 <sup>th</sup> charge-discharge profiles at 0.1 C of (a) LR1 and (b) LR2. The broken lines in (a) on the 60 <sup>th</sup> charge curve are to show that there still exist two regions, with the right indicative of existence of activation.....	50
Figure 3.4 (a) Cyclic performance at 0.1C, (b) rate capability at various C rates, .....	53
Figure 3.5 Cyclic voltammograms between 2.0–4.8 V at a scan rate 0.1 mV/s, (a) LR1 and, (b) LR2.....	56
Figure 3.6 Nyquist plots of EIS spectra of LR1 and LR2 materials at different cycles; (a) before the first cycle, (b) after the 10 <sup>th</sup> cycle and, (c) after the 100 <sup>th</sup> cycle.....	57
Figure 4.1 FTIR of (a) gel, and (b) dry powder.....	65
Figure 4.2 Acetylation mechanism of cornstarch with metal acetates.....	65
Figure 4.3 Thermal analysis of cornstarch with; (a) LRAC, (b) LRNI, and (C)LRACNI. ....	68
Figure 4.4 Typical SEM images of (a) LRAC, (b) LRNI, and (c) LRACNI, at different magnifications.....	70
Figure 4.5 XRD patterns of LRAC, LRNI and LRACNI in the 2 $\theta$ range of (a) 5-90 $^{\circ}$ and (b) 18-19.7 $^{\circ}$ . ....	72
Figure 4.6 (a) 1 <sup>st</sup> , (b) 5 <sup>nd</sup> , (c) 10 <sup>th</sup> , and (d) 30 <sup>th</sup> ; charge/discharge curves for LRAC, LRNI and LRACNI cathode materials.....	74

Figure 4.7 (a) Discharge capacities at 0.1C, (b) Columbic efficiency at 0.1C, (c) Discharge Capacities at 1C, and (d) Rate capability at different current densities; of LRAC, LRNI and LRACNI between 2.0-4.8V. ....	77
Figure 4.8 Cycle voltammeries of (a) LRAC, (b) LRNI, and (c) LRACNI; at a scan rate of 0.1 mV/s, between 2.0 - 4.8 V. ....	78
Figure 4.9 EIS spectra for LRAC, LRNI and LRACNI electrodes, after the 10 <sup>th</sup> cycle. ....	79
Figure 5.1 The SEM images of the dry powder (top), and the sintered one at 750°C/ 12hr (bottom). ....	83
Figure 5.2 XRD patterns for; (a) dry powder NCA (400 C), and (b) sintered powder at 750 °C/ 12hr. ....	85
Figure 5.3, (a) Initial charge/discharge capacity at 0.1C, (b) Discharge capacity at 0.3 and 1C, and (c) rate capability at different C-rates. ....	86
Figure 5.4, (a) Cyclic voltammetry for the 1 <sup>st</sup> , 2 <sup>nd</sup> and the 10 <sup>th</sup> cycles, (b) Nyquist plot after the 10 <sup>th</sup> cycle; of NCA cathode material. ....	88

## **List of Tables**

Table 2.1 Li, Mn, Ni and Co experimental quantities in mole fraction, analyzed by ICP-MS.....	26
Table 2.2 Lattice parameters, c/a ratios, I (003)/I (104) (R), and (I (102)+I (006))/I (101) (R') intensity ratios for the synthesized samples.....	28
Table 2.3 Discharge capacity, capacity retention, and electrode-electrolyte film resistance exhibited by LMNC1, LMNC2, LMNC3, and LMNC4.....	33
Table 2.4 Comparison of using different solvents in synthesizing $\text{LiMn}_{1/3}\text{Ni}_{1/3}\text{Co}_{1/3}\text{O}_2$ cathode materials via sol-gel method.....	38
Table 3.1 Mole fractions of Li, Mn, Ni, and Co analyzed by ICP-MS.....	46
Table 3.2 The crystal structure parameters of the prepared Li-rich cathode materials.....	48
Table 3.3. First, 30 <sup>th</sup> and 60 <sup>th</sup> charge and discharge capacities and capacity losses.....	51
Table 3.4. $R_{\text{SEI}}$ values of LR1 and LR2 materials at different cycles.....	56
Table 4.1 ICP-MS data for LRAC and LRAC and LRNI cathode materials.....	69
Table 4.2 Lattice parameters of LRAC, LRNI and LRACNI samples.....	72
Table 5.1 Comparison of NCA cathode material electrochemical performance with previous work.....	87

## Abstract

Many synthesis techniques like sol-gel, co-precipitation, hydrothermal, pyrolysis, and many more have been used to synthesize batteries' active electrode materials. High surface area cathode materials with smaller nanoparticles are favored for their higher reactivity compared to materials with particles of larger size. Sol-gel and co-precipitation methods have been primarily adopted because they can produce the desirable particle size easily and on a large scale.

This dissertation details an efficient and cost-effective process for using a newly developed sol-gel method that uses glycerol solvent instead of the conventionally used water. Glycerol has three hydroxyl groups (OH) instead of one in water. These can play an important role in nanoparticle formation at earlier stages by speeding up the reaction. One of the main reasons for capacity fade in batteries is cationic mixing between  $\text{Ni}^{2+}$  and  $\text{Li}^+$ . This results in blocking of the  $\text{Li}^+$  path and ultimately poor cyclability. This capacity fade has been successfully minimized in our current work by taking advantage of the high heat released from glycerol to get partially crystalline nanoparticles that could mitigate cationic mixing at high temperatures.

The first cathode material synthesized using glycerol solvent was  $\text{LiMn}_{1/3}\text{Ni}_{1/3}\text{Co}_{1/3}\text{O}_2$  (LMNC) layered oxide cathode material. Temperature's effects on the particles' morphologies, sizes, and electrochemical performances have been studied at four different temperatures. LMNC was annealed at  $900\text{ }^\circ\text{C}/8\text{hr}$  and shows desirable particles size of  $\sim 0.3\text{ }\mu\text{m}$ , an initial discharge capacity of  $177.1\text{ mAh/g}$  in the first cycle, and a superior capacity retention of  $83.7\%$  after 100 cycles. The process takes eight hours, rather than  $>12\text{hr}$  when using other solvents to prepare LMNC material at high

temperatures. The results also demonstrate the higher stability and lower cationic mixing after 100 cycles.

To increase capacity and voltage, lithium-rich cathode materials with the formula  $\text{Li}_{1.2}\text{Mn}_{0.51}\text{Ni}_{0.145+x}\text{Co}_{0.145-x}\text{O}_2$  ( $x = 0$  (LR2), 0.0725 (LR1)) have been successfully synthesized. In this material, cobalt (Co) content has been decreased by half and the larger produced particles have suppressed the total activation of  $\text{Li}_2\text{MnO}_3$  phase in the first charge cycle. The specific discharge capacity retention of LR1 at 1C between 2 and 4.8 V was more than 100% after 100 cycles.

Further improvements to LR1 cathode materials have led to an increase in the initial discharge capacity to 248 mAh/g at 0.1C. This is achieved by using an equimolecular combination of acetate and nitrate salt anions (LRACNI) with cornstarch. Cornstarch acts as a capping agent with the nitrate salt anions, and a gelling agent with acetate based anions. LRACNI shows an intermediate particle size with satisfactory capacity retention upon cycling and the lowest cationic mixing.

$\text{LiNi}_{0.8}\text{Co}_{0.15}\text{Al}_{0.05}\text{O}_2$  (NCA) is one of the most commercialized cathode materials for lithium-ion batteries. It is challenging to have a high Ni content with Li in one combination electrode because cationic mixing increases proportionally. The use of glycerol has diminished the cationic mixing. High capacity retentions of 97% at 1C after 50 cycles, 87.6% at 0.3C after 100 cycles, and 93.6% at 0.1C after 70 cycles have been successfully achieved, which are better than those previously reported.



# Chapter 1. Introduction

## 1.1 Overview

Out of all the kinds of batteries, lithium-ion batteries (LIBs) have an unmatched combination of high power density and energy. This has made them the essential choice in powering power tools, portable electronic devices, hybrid/full electric vehicles (HEVs), and electric vehicles (EVs) [1]. HEVs and EVs can eliminate greenhouse gas emissions [2], which are environmentally unfriendly. Lithium-Ion batteries can be used in electric grid applications due to their tremendous energy efficiency. They enhance the quality of energy gained from renewable sources like wind, solar and geothermal. The widespread use of lithium-ion batteries in different fields will be essential to building a future of sustainable energy.

Currently, there are some doubts that LIBs can meet the world's power demand for portable energy storage devices. For example, for some applications such as grid and transportations, the age of lithium is too short, the cost of lithium-ion batteries is pretty high. One day we will encounter issues in acquiring the transition metals which are currently used [3].

On the other hand, there are a lot of advantages of using LIBs rather than other batteries with different chemistries. First, they have the highest possible cell potential for ion-based material batteries because lithium has the lowest reduction potential compared to most elements. Second, lithium-ion based materials have the highest power density, volumetric capacity and gravimetric capacity because Li is the third lightest element and has the smallest single charged ion radius. It is hard to develop a substitute element as illustrated in Figure 1.1 [4].

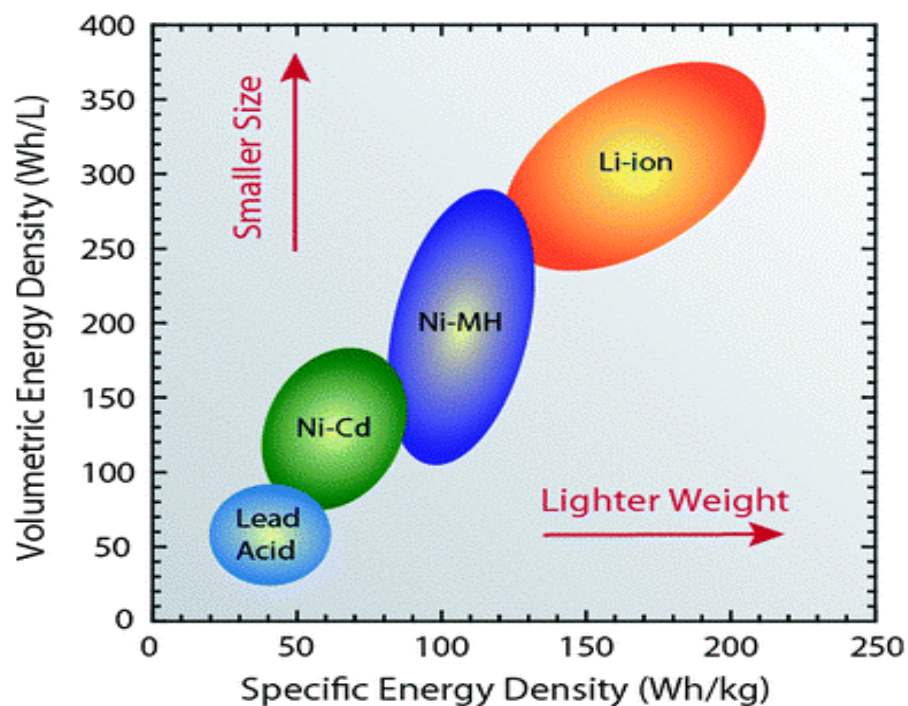


Figure 1.1 Comparison between volumetric and specific energy densities for rechargeable batteries [4].

Although a high charge capacity per ion can be gained by using multivalent cations, the extra charge on the multivalent ions will decrease their mobility, as well as cause battery power performance to be determined by ionic diffusion in solid electrodes. Despite the fact that LIBs cannot meet the world's power demand for some applications, the amount of lithium available in terms of absolute quantities is sufficient to provide enough power for automobiles [3]. The problem is the total price of the electrode materials, which has hindered the expansion of these materials. The cost of lithium is small compared to the cost of the other electrode materials that make up the battery. Besides the processing cost, the most significant contributor to cost is Cobalt (Co) in the cathode material. Incorporating other metal oxides, such as Manganese and Nickel (see Figure 1.2), in the cathode material with cobalt will help decrease the total cost and lead to other advantages that will be discussed later in this work. Consequently, Li-ion will be the dominating source of portable electrochemical energy storage for many years to come

[6,7]. Choosing Li-ion batteries as the primary source of portable electrochemical energy storage motivates a large group of researchers to improve their performance and cost. Our goals will help expand the usage of these batteries and the applications for which they can be used.

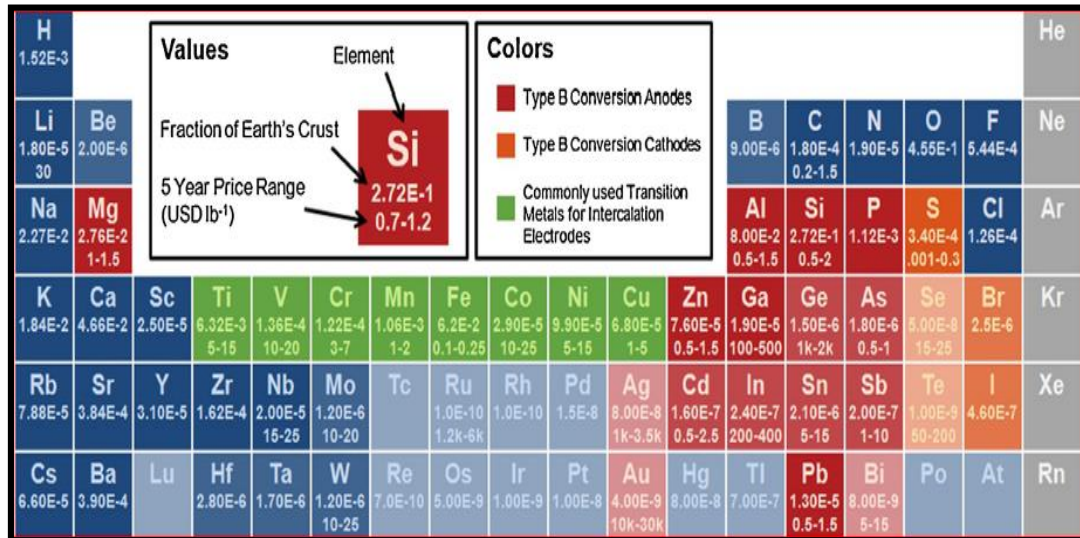


Figure 1. 2 The availability of metals as a fraction of Earth’s crust with the prices for 5 years [3].

## 1.2 Lithium-ion battery components and working mechanism

Batteries are systems that are used for electrochemical energy storage and conversion. In such systems, chemical redox reactions occur at anode and cathode and are converted into electrical energy. The reaction at the cathode takes place at a higher potential than that at the anode, giving the terms positive and negative electrodes. Due to the participation in energy storage and conversion, electrodes are not only a charge transfer medium, but also the active element. The main components of lithium-ion batteries are, the cathode (positive electrode), the anode (negative electrode), the separator that is made from porous plastic film to prevent contact between the electrodes, and the electrolyte.

The cathode material should meet the minimum requirements to be a good host for  $\text{Li}^+$  during intercalation/deintercalation processes. They should have low lithium diffusion barrier, low lithium chemical potential, high electronic conductivity, high delivered capacity, and good structural stability that helps to keep the battery performance satisfied over cycling. The aforementioned advantages are found in lithium metal oxides [7]. Likewise, the anode materials should have the same characterizations as the cathodes. Graphite was used as an anode material in lithium-ion batteries due to its low cost and low operation voltage. However, its low chemical potential of  $\sim 0\text{V}$  has led to some safety issues, and other materials have been introduced to replace it. The electrolytes are mainly made of lithium salts like  $\text{LiBF}_4$  or  $\text{LiPF}_6$  that dissolve in a high electronic and ionic conductive solvent mixture of organic alkyl carbonates like ethylene (EC), diethyl (DEC), dimethyl (DMC), or ethyl methyl (EMC). Figure 1.3 shows the hierarchical structure of lithium-ion batteries.

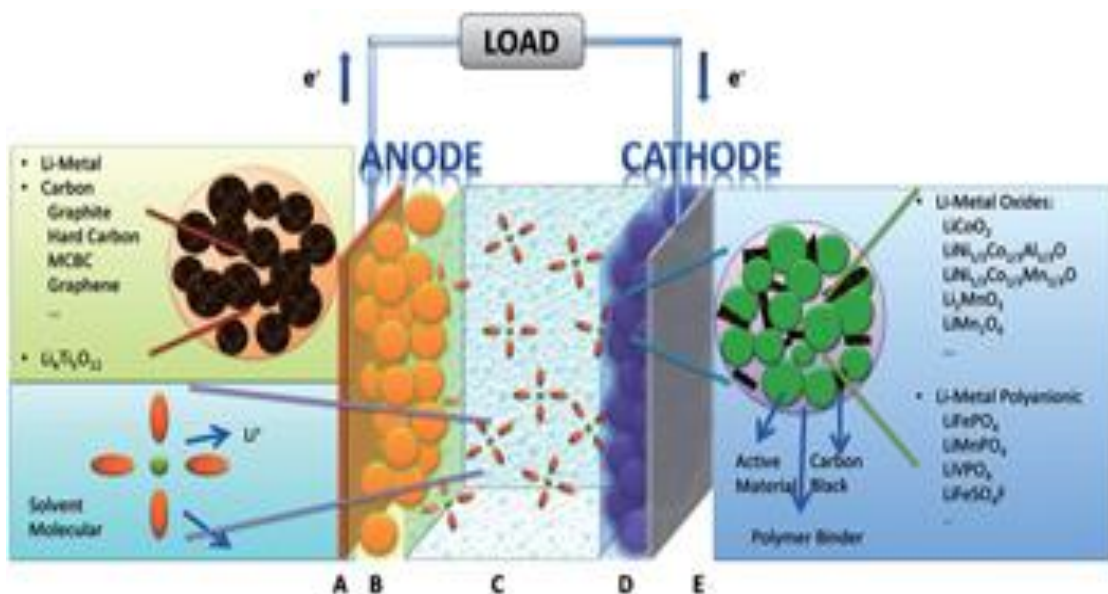


Figure 1. 3 The hierarchical structure of lithium-ion batteries [8].

LIBs are unlike the metallic lithium that is used in non-rechargeable lithium batteries. They use an intercalation cathode and a solid network as hosts for a  $\text{Li}^+$  guest. During

the charge,  $\text{Li}^+$  moves from the host network (cathode) to the anode through the electrolyte, while electrons move throughout the circuit in the same direction, and vice-versa during the discharge. Figure 1.4 shows the charge-discharge mechanism for LIBs [9].

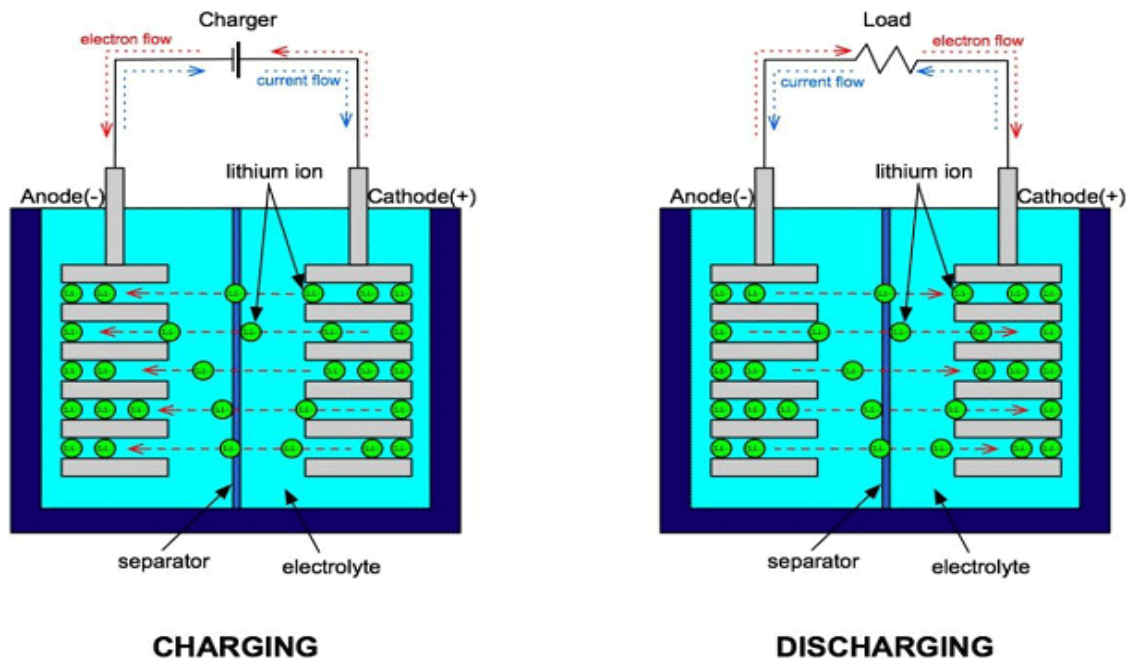


Figure 1. 4 Charge- Discharge mechanism for lithium-ion batteries [9].

## 1.2 Transition metal oxide

The first layered transition metal oxide  $\text{LiCoO}_2$  (LCO) was introduced by Goodenough, and first commercialized in LIBs by Sony. Due to its high theoretical specific capacity of 273 mAh/g, good cyclability, low self-discharge, and high discharge voltage, LCO is still used for commercialized LIBs [8,9]. However, people are investigating other transition layered materials that have less toxicity and higher thermal stability than those using cobalt when heating LCO, the resulting release of oxygen causes a runaway reaction that makes the cell burst into flames. Due to that,  $\text{LiNiO}_2$  (LNO) was introduced as a cathode material in LIBs. LNO has the same theoretical specific

capacity as LCO at a value of 275 mAh/g. Compared to LCO, LNO has a high energy density and low cost. However,  $\text{Ni}^{2+}$  has approximately the same radius as  $\text{Li}^+$ , which leads to  $\text{Ni}^{2+}$  blocking  $\text{Li}^+$  diffusion pathways [11]. Moreover,  $\text{Ni}^{3+}$  is more radially reduced than  $\text{Co}^{3+}$ , making it even more thermally unstable than LCO [12].

$\text{LiMnO}_2$  (LMO) is another promising cathode layered material. The presence of Mn can induce a structure change during cycling. Mn has less toxicity compared to Ni and Co and is much cheaper [13]. On the other hand, unsatisfactory cycling performance is likely to happen in all LMO cathode materials due to the structure changes (layered to spinel) during Li-ion deintercalation [13] and the leaching out of Mn during cycling [14]. A combination of LCO, LNO, and LMO in one layered metal oxide, in the form  $\text{LiMn}_x\text{Co}_y\text{Ni}_z\text{O}_2$ , can decrease the toxicity and price for Co, decrease the quantity of  $\text{Ni}^{2+}$  and  $\text{Li}^+$  cation mixing, and takes advantage of Mn as a structure stabilizer during cycling [15]. The world's demand for NMC materials will increase by the end of 2025 as shown in Figure 1.5.

Cathode active materials in 2015      Cathode active materials in 2025

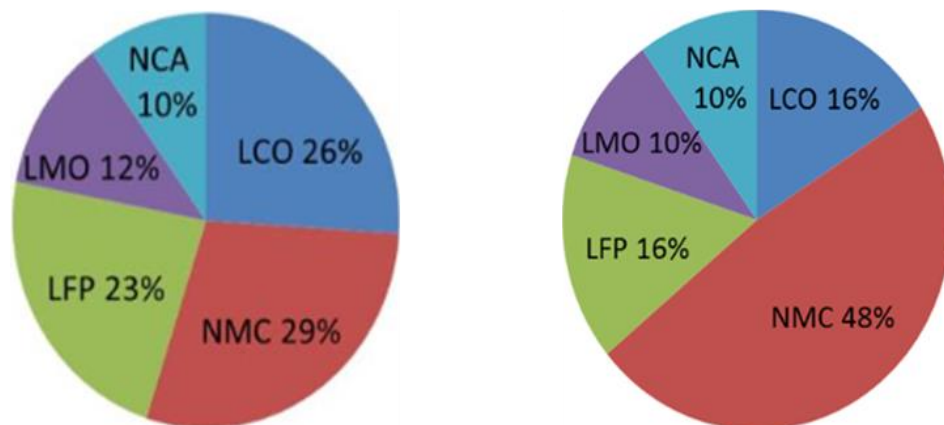


Figure 1. 5 Comparison of lithium-ion battery cathode materials in 2015 and 2025 [16].

Besides the layered-structure cathode materials for lithium-ion batteries, there are spinel and olivine structures as shown in Figure 1.6. However, these kinds show lower

working voltage and lower specific discharge capacity compared with layered structure

Figure 1. 7.

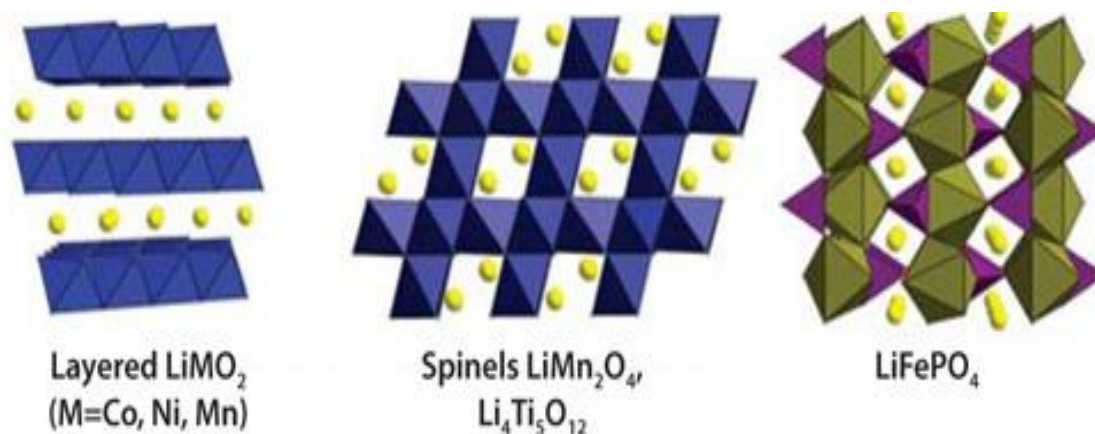


Figure 1. 6 Electrode material for lithium-ion battery [17].

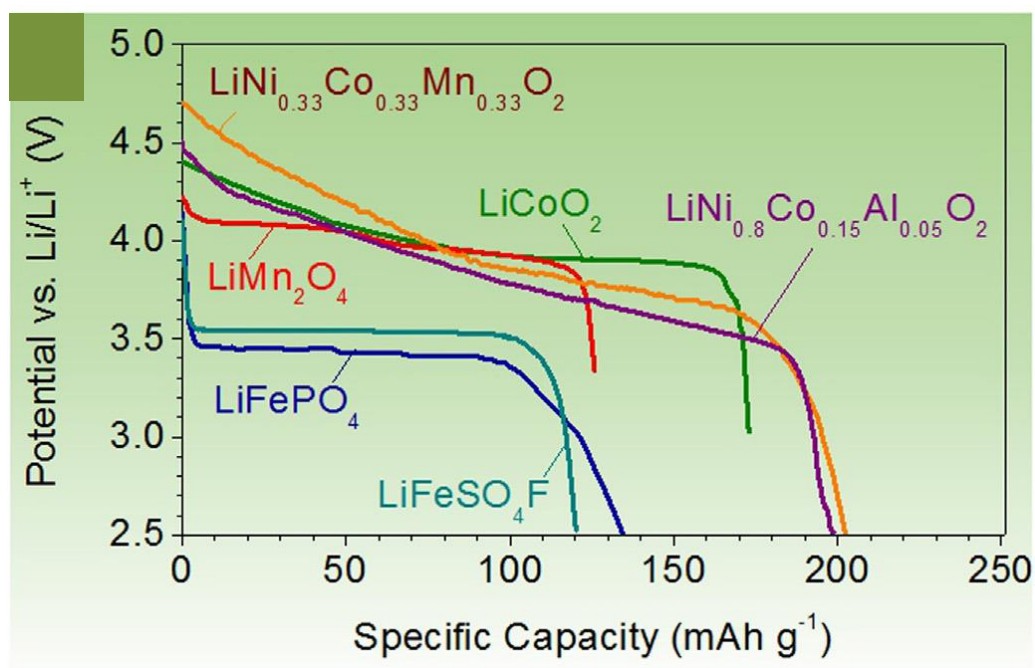


Figure 1. 7 Discharge profile of different lithium-ion batteries [3].

### 1.3 $\text{Li}_x\text{M}_y\text{O}_2$ (M=Mn, Co, Ni) developments

Since the time of the first commercialized layered cathode materials for Lithium-ion batteries,  $\text{LiCoO}_2$  (LCO), a ternary metal mixture of Mn, Co, and Ni, has been studied

and developed for 28 years as shown in Figure 1.8. The capacity has increased from 150 mAh/g to 180 mAh/g, in addition to the other advantages of safety, cost, and toxicity. The ever-growing demand for energy has motivated researchers to develop new layered cathode materials with a ternary combination of transition metals that could adopt more Li ions in the layered structure.

Transition metals (TM) including Mn, Co, and Ni have a great impact on the physical and electrochemical properties of the working electrode. The presence of  $\text{Co}^{3+}$  and  $\text{Mn}^{4+}$  is important to stabilize the structure.  $\text{Ni}^{3+}$  is easily reduced to  $\text{Ni}^{2+}$ , which destabilizes the cathode structure by moving to the Li layer. These ions have almost the same ionic radius, which leads to impeded  $\text{Li}^+$  transport and eventually poor cyclability, as shown in Figure 1.9.

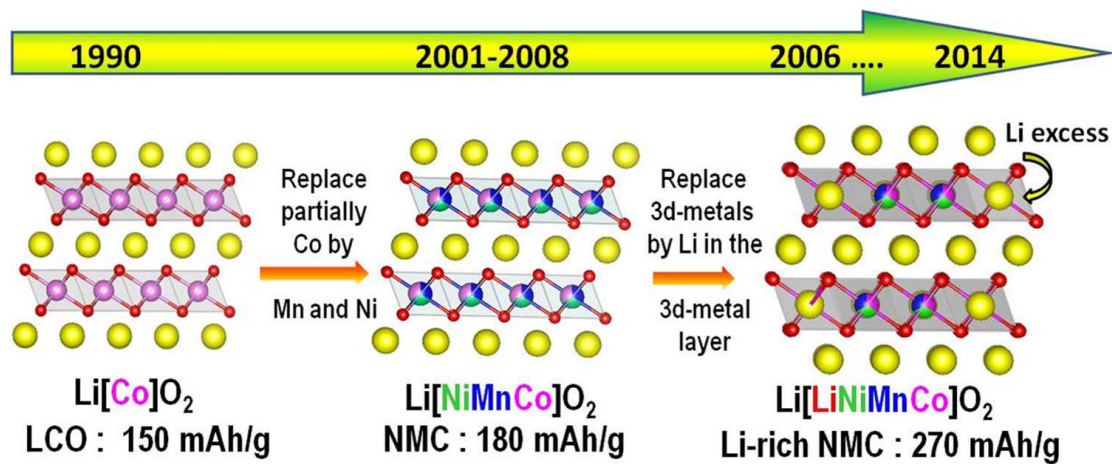


Figure 1. 8 Chronological evolution of the layered oxide  $\text{LiCoO}_2$  chemistry fueled by cationic substitution within the metal layers (left) with i) partial replacement of Co with Ni and Mn (NMC phase) within the metal layer (purple) and ii) more recently with Li (yellow) to form Li-rich NMC phases [18].



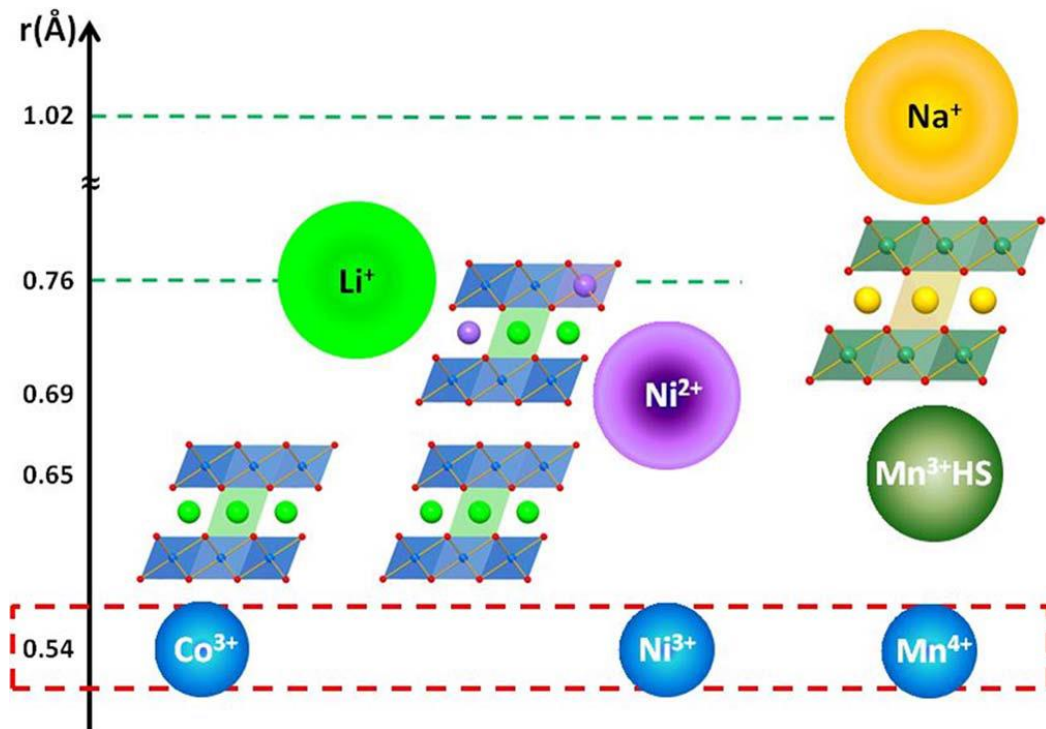


Figure 1. 9 Comparison of ionic radii of alkaline species and TM ions in their stable valence states at synthesis operating temperatures and their influence on the 2D layered characters of AMO2 phases. Dashed red rectangle shows ions leading to strictly 2D layered LiMO2 structure and the partial cation mixing due to Ni reduction is schematically represented [18].

Figure 1.10 explains the role of each of the three elements; Mn increases the thermal stability, Ni increases the discharge capacity, and Co increases the capacity retention. However, increasing the contents of each one of them will affect the other two properties. It is challenging to have all three advantages, high thermal stability, high discharge capacity, and high capacity retention, in one material. Efforts have been made to establish a new cathode material that could supply more capacity by increasing the Li content rather than the other TM.

Starting in 2006, Lithium-rich cathode materials with the formula of  $\text{Li}_{1+x}\text{M}_{1-x}\text{O}_2$  have been investigated. An interestingly high initial discharge capacity of 270 mAh/g was reached. It is believed that the excess  $\text{Li}^+$  substitution for the  $\text{M}^{3+}$  in the [MO2] layers is the deriving of the Li-rich layered structure formation (Figures 1.11a-b). The valance

state increase of the remaining M elements guarantees the charge compensation following the formula of  $\text{Li} [\text{M}^{3+}_{1-2x}\text{M}^{4+}_x \text{Li}_x] \text{O}_2$ . Notably, that occurs at a limit of  $x=1/3$  and solely in the M valance state of  $1/4 \text{Li}[\text{Li}_{1/3}\text{M}_{2/3}]\text{O}_2$ . Among all the abundant structures,  $\text{Li}_2\text{MnO}_3$  is the most investigated to date.  $\text{Li}_2\text{MnO}_3$  monoclinic phase with the space group of C2/m takes into account the distortion induced by the ordered distribution of the  $\text{Mn}^{4+}/\text{Li}^+$  cations in the mixed  $[\text{Li}_{1/3}\text{Mn}_{2/3}]\text{O}_2$  layer [19]. In this way,  $\text{Li}^+$  will be surrounded by six M, as shown in Figure 1.11c [20–22].  $\text{Li}_2\text{MnO}_3$  is inactive at low voltage without acid treatments. The activation at high voltage ( $>4.5\text{V}$ ) [23] shows better performance than the conventional one of  $\text{LiMO}_2$ .

Despite the higher working voltage up to 4.8V and the superior discharge capacity of Li-rich cathode materials, there are capacity and voltage fades upon cycling. To overcome these issues, some surface treatments were proposed.

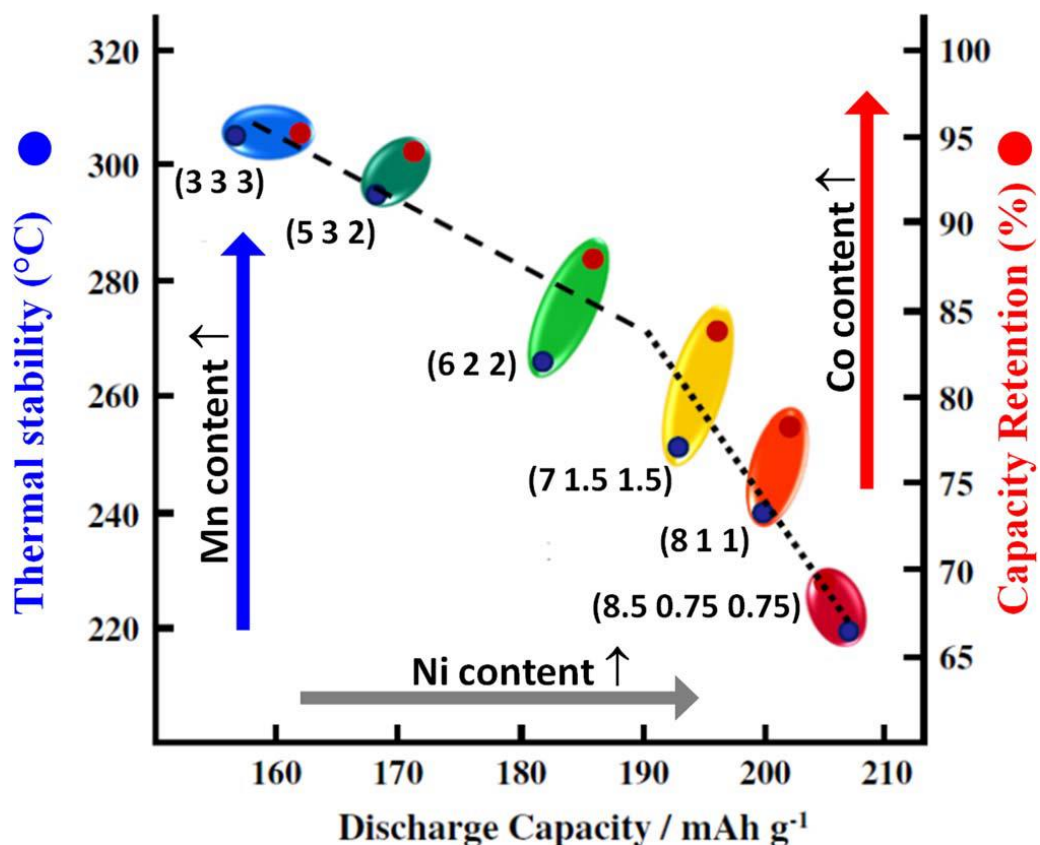


Figure 1. 10 A map of relationship discharges capacity (black), thermal stability (blue) and capacity retention (red) of Li/Li[Ni<sub>x</sub>Co<sub>y</sub>Mn<sub>z</sub>]O<sub>2</sub> compounds with number in brackets corresponding to the composition (Ni Mn Co) [18,24].

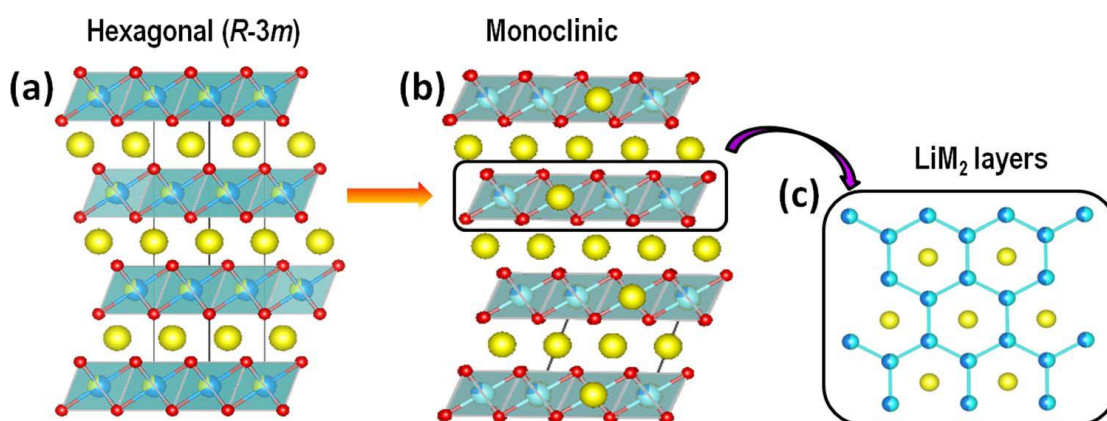


Figure 1. 11 Structural representation of (a) O3-type layered oxides; (b) the overall cell of Li-rich layered oxides described as monoclinic and (c) M / Li ordering within LiM<sub>2</sub> layer [18].

## 1.4 Lithium-ion batteries synthesis methods

Many synthesis techniques were developed to produce cathode materials for Lithium-ion batteries, like sol-gel, solid state, combustion, co-precipitation, and many others, as shown in Figure 1.12. Particles' size, morphology, cationic ordering, electrochemical properties, and eventually, electrode performance will be affected accordingly. For example, the solid state synthesis approach requires extreme conditions (temperature and pressure) to prepare the materials.

Despite the advantages of portability, high voltage, safety, and cycleability of the growing LIBS products, their future applications in HEVs and EVs require a high charge-discharge rate. Some features in the electrode materials are essential to the determination of their limitations at higher rate working processes, including slow insertion/extraction of  $\text{Li}^+$  in/from the cathode material, and low electronic and ionic conductivity in the electrode materials. Selecting the preparation process of LIB cathode materials is important to the synthesis of phase-pure and fine-sized cathode materials, as these are strongly affected by synthesis approach.

Recently, researchers have used high surface area (Nano-sized particles) cathode materials, because of their higher reactive sites that provide high charge/discharge transfer and shorter  $\text{Li}^+$  diffusion path. However, higher reactivity of the nanosized materials may negatively impact the inter-particle electrical contact, and surface-side reactions may be detrimental. The tendency of nanoparticles of the spinel cathode materials toward reactivity with the electrolyte is much higher than that of micro-sized particles, which will result in dissolution of the metal ions from the nanosized particles [25].

The world's demand for energy, and the search for a substitute for fossil fuels has motivated many researchers to modify the energy storage devices that harvest energy from the renewable resources like wind, solar, and geothermal. Among all of the reported synthesis methods, sol-gel (SG) and co-precipitation (CP) have been adopted widely. Because these methods are powerful and ensure large scale production in an easy way, they lower cost compared to other production methods [26]. The particles' size has an important role at higher rate charge/discharge processing. Comparing to the CP method, SG produces smaller sized nanoparticles and shows better electrochemical properties at low rates of current density. However, the CP method has a larger particle size and better capacity retention at high current density working [26]. The SG method could be easily improved to produce larger particle sizes that would improve the efficiency at high rates, by using modified techniques like controlling the heat treatment at high temperatures and using other solvents rather than the traditionally used ones. We will discuss this deeply in our presented works.



Figure 1. 12 Different synthesis techniques utilized to produce cathode Materials [27].

### 1.5 Sol-gel synthesis method

Synthesis procedure plays an essential role in particle morphology, cation ordering, and ultimately, the electrochemical properties [15–17]. Several synthesis approaches have been reported to produce  $\text{LiMn}_{1/3}\text{Co}_{1/3}\text{Ni}_{1/3}\text{O}_2$  (LMNC), such as hydroxide precipitation [31], carbonate co-precipitation [32], microwave [33], and modified sol-gel [28]. Of all of these, sol-gel and co-precipitation synthesis approaches have been the most widely adopted. In this particular study, the sol-gel synthesis approach is adopted. It can ensure uniform particle distribution at an atomic level, and a phase pure, ultra-fine powder with a reduced particle size as a final product.

This synthesis method involves dispersing nanoparticles in liquid, which are constantly undergoing hydrolysis processes with heating. For some nanoparticles, functional groups are created when water molecules evaporate out of the solution. Most of them

have at least two reactive sites. As nanoparticles bounce and bump each other in random motions (Brownian motion), it makes another strong bond with each other. For other nanoparticles, this doesn't work. Some additives can be added to enhance the nanoparticles surface reactivity or remove something from the surface, so that they can stick together. The gelling point starts when a series of three-dimensional nanoparticle networks are created and span the liquid. Further heating is necessary to get amorphous or crystalline nanoparticles.

Many researchers report the synthesis of  $\text{LiMn}_{1/3}\text{Co}_{1/3}\text{Ni}_{1/3}\text{O}_2$  lithium-ion cathode materials using water as a solvent with some additives can help gel formation. Figure 1.13 illustrates the schematic diagram of the sol-gel technique to produce nanoparticles as a cathode material for lithium ion batteries.

The glycerol solvent is totally different from water and will form deep eutectic solvent with metal acetate salts. Therefore, there may not be sol formation in the traditional sense in our new process. For the lack of a better way to describe the synthesis process, we still call it a sol-gel process.

## The Sol-Gel Process

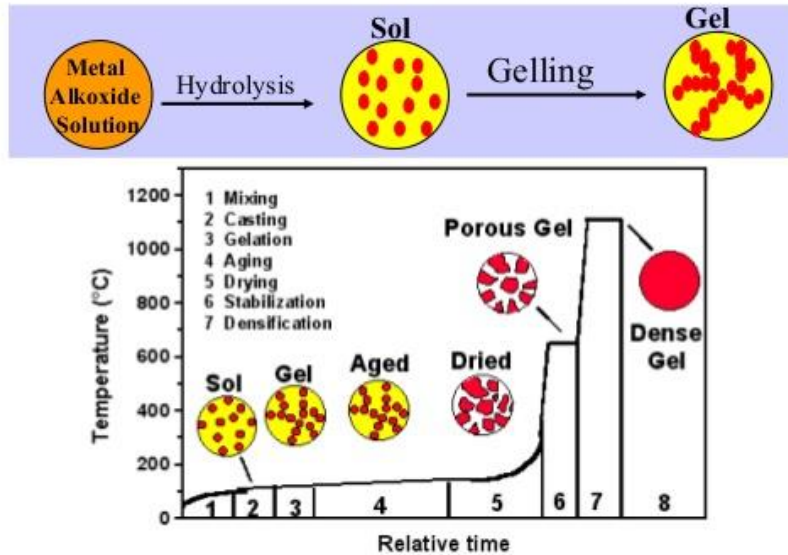
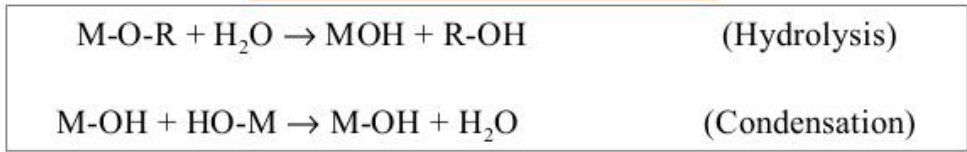


Figure 1. 13 Sol-Gel process [34].

### 1.6 Research Objectives

With the increase of world population, energy consumption has increased. In search of an economical method to produce energy storage devices, a lot of researchers seek to modify these devices. Therefore, they will be safer, easier to use, easier to transport, and able to work long term. However, the long term of heat treatment and the issues related to cell performance are still not satisfactory.

Previously, water was used as a solvent in the sol-gel method to synthesize cathode materials for lithium-ion batteries. The sol-gel method is a hydrolysis process; therefore; the more OH groups there are in the solvent, the faster the formation of amorphous or crystalline nanoparticles will be. This results in shorter heat treatments to synthesize electrode materials.



In this study, glycerol has been demonstrated to be an alternative, green solvent in the sol-gel synthesis approach. Glycerol has three hydroxyl groups that can participate in gel formation, which makes the process faster than those with other solvents. The heat of combustion of glycerol is much higher than that of water, making another heat source that can decrease the duration of heat treatment.

The process is environmentally friendly and has been proven to be a good producer of nanocrystalline cathode materials for lithium-ion batteries. Figure 1.14 shows the schematic diagram of the sol-gel method using glycerol as a solvent to synthesize layered structure cathode materials for lithium-ion batteries.

This work consists of four parts; the first part focuses on the synthesis procedure of  $\text{LiMn}_{1/3}\text{Ni}_{1/3}\text{Co}_{1/3}\text{O}_2$ .  $\text{LiMn}_{1/3}\text{Ni}_{1/3}\text{Co}_{1/3}\text{O}_2$  (layered oxide cathode material) was successfully synthesized in about 2/3 the time required to synthesize the same material using water as a solvent. The material was synthesized at different temperatures and characterized using various techniques. Additionally, the electrode performance improved over 100 cycles.

The second part is mainly about producing cathode material with higher working voltage and higher productivity. Cathode materials with higher lithium quantities have been produced to increase the delivered capacity (lithium rich cathode materials). In contrast to conventional lithium-rich cathode materials, which undergo performance depletion over cycling, the synthesized electrodes demonstrate increasing discharge capacity over several cycles. Moreover, the total amount of cobalt is decreased to decrease the toxicity and cost of the electrodes.

In the third part, we studied manganese-based Li-rich cathode materials prepared using precursor salts with acetate and nitrate anions. The effect of the cornstarch (gelling agent), when used with different salts, was comprehensively studied. Cornstarch is a

combustible fuel and a gelling agent in different applications. Different morphologies and particles sizes will be produced for the final products, accordingly.

Fourier-transform infrared spectroscopy (FTIR) results show that formation of acetyl groups with acetate-based salt prevents cornstarch from capping the nanoparticles, and the particles' size will still increase proportionally with heat. However, smaller particles will form with nitrate-based salt due to the capping of the nanoparticles with the cornstarch.

Taking advantage of the higher stability of the larger particles of the acetate salt and the higher productivity of the smaller particles (higher surface area) of the nitrate salt by mixing them in one precursor was studied. The produced powder exhibits an effective way to improve the electrochemical performance and physical characteristics.

In the last part of the dissertation, we successfully synthesized  $\text{LiNi}_{0.8}\text{Co}_{0.15}\text{Al}_{0.05}\text{O}_2$  (NCA) cathode material. NCA is as one of the most commercialized cathode materials nowadays. Higher delivered energy, which is associated with the highest content of nickel in the composite, has drawn a lot of researchers' attention.

However, the presence of too much Ni could cause problem by increasing the cationic mixing, resulting in capacity deterioration over cycling. Glycerol has been proven to be a structural stabilizer and lead to lower cationic mixing in our previous works. The NCA cathode material prepared using our modified way shows superior capacity retention after 100 cycles at different current rates.

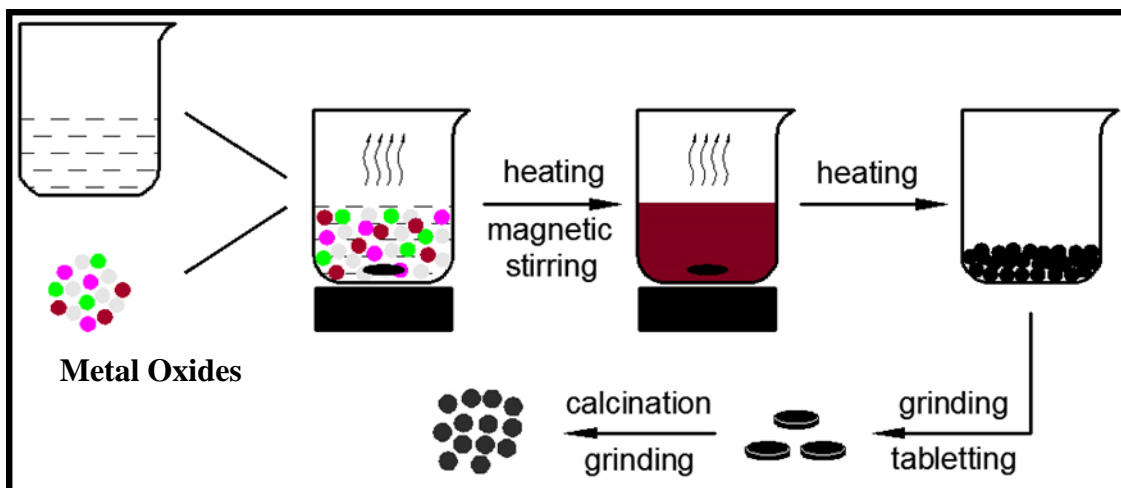


Figure 1. 14 Schematic diagrams of the sol-gel technique to produce nanoparticles as a cathode material for lithium ion batteries.

## **Chapter 2. Synthesis of layered $\text{LiMn}_{1/3}\text{Ni}_{1/3}\text{Co}_{1/3}\text{O}_2$ oxides for Li-ion batteries using biomass glycerol as solvent**

Published in Energy Technology journal, 2017, DOI: 10.1002/ente.201700646

### **2.1 Abstract**

In an attempt to exploit biomass glycerol as a solvent, a sol-gel method was used to synthesize  $\text{LiMn}_{1/3}\text{Ni}_{1/3}\text{Co}_{1/3}\text{O}_2$  (LMNC) layered oxide cathode materials for Li-ion batteries. The effects of different annealing temperatures on the particle size and structure of the layered oxide materials have been studied. The chemical compositions, cationic ordering, and particle morphology were obtained by various advanced techniques. Electrochemical performance of the layered oxides was analyzed by cycling testing, cyclic voltammetry, and electrochemical impedance spectroscopy. A comparison of four LMNC samples in this study shows that the LMNC annealed at  $900^\circ\text{C}$  exhibits the most promising electrochemical properties. In particular, an initial discharge capacity of 177.1 mAh/g has been achieved, with a retention of the discharge capacity over 83.7% after 100 cycles. Furthermore, the sample shows good rate capability up to 5C, making it well qualified for lithium-ion battery applications. This study demonstrates the possibility of using glycerol, a byproduct in biodiesel production, as a solvent instead of water in the sol-gel method to synthesize layered-structure cathode materials.

## 2.2 Introduction

Lithium-ion batteries (LIBs) are presently the chemistry of choice for powering portable electronic devices and are growing in popularity for use in electric vehicles (EV), hybrid electric vehicles (HEV), and as storage units in solar energy systems [1]. Despite the success LIBs have achieved in commercial applications, research continues in the search for better electrode materials [1,35].

Layered structures with the formula LMNC are one of the most promising cathode materials used in Li-ion batteries. LMNC, first introduced by Ohzuku *et al.* [36] in 2001 as a layered mixed transition metal oxide with a hexagonal structure, has become a replacement candidate for  $\text{LiCoO}_2$  due to its high specific capacity, low cost, reduced toxicity, and good thermal stability [32]. Each individual element in LMNC has properties beneficial to the overall cathode material. The presence of cheap, environmentally friendly manganese in the structure helps reduce the total cost and toxicity while also helping overcome the problems related to the structural stability that arise upon cycling. The presence of cobalt results in the increased ordering of lithium and transition metal oxides in the layered structure. With nickel, the charge/discharge capacity of the structure is increased because of the two possible electron transfers,  $\text{Ni}^{2+} \leftrightarrow \text{Ni}^{4+}$ . On the whole, LMNC material exhibits excellent electrochemical behavior, particularly if the adopted valance states of Mn, Ni, and Co are +4, +2, and +3, respectively [28,37–42].

The synthesis method of LMNC plays an important role in the particle size, morphology, cation distribution, and mechanical properties of the resulting material [30,43,44]. Within the last decade, many approaches have been used to synthesize layered structure cathode materials for LIBs, such as the solid state method [45], the

use of microwaves and solution combustion [33], hydroxide precipitation [32], carbonate co-precipitation [32], inverse micro emulsion [39], and modified sol-gel technique [43]. Of these processes, the co-precipitation and sol-gel techniques have proven most popular due to their reduced time and low energy requirements. Furthermore, the sol-gel technique can ensure uniform particle distributions at the atomic level and yield phase-pure and ultra-fine powders [34], making it ideal for producing battery materials.

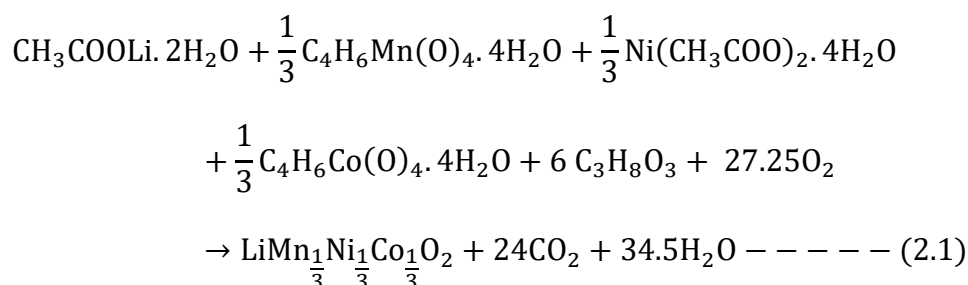
In this work, the synthesis of LMNC layered structure cathode material is carried out by adopting a sol-gel synthesis method and using glycerol as a solvent and cornstarch as a gelling agent. The sol-gel synthesis involves liquid dispersion of nanoparticles, which are constantly undergoing hydrolysis processes while being heated. For some nanoparticles, functional groups are created when water molecules evaporate out of the solution. Most of these functional groups have at least two reactive sites, and as nanoparticles collide with each other in random motion (Brownian motion), they can form strong bonds [34]. Using glycerol as a solvent can reduce the reaction time of the atoms that form nanoparticles due to the presence of three hydroxyl groups in glycerol. It can also speed up gel formation, and the heat generated from the chemical reaction can increase the reaction rate. Corn starch was used as a gelling agent for LMNC due to its two types of polymeric chains (linear of amylose and branched of amylopectin) and its extensive use as a gelling agent in the soap and food industries [46,47].

## 2.3 Experimental Section

### 2.3.1 Powder synthesis

LMNC was prepared by dissolving stoichiometric amounts of  $\text{Li}(\text{CH}_3\text{COO})\cdot 2\text{H}_2\text{O}$  (Sigma-Aldrich, reagent grade),  $\text{Mn}(\text{CH}_3\text{COO})_2\cdot 4\text{H}_2\text{O}$  (Sigma-Aldrich, 99%),  $\text{Ni}(\text{CH}_3\text{COO})_2\cdot 4\text{H}_2\text{O}$  (Sigma-Aldrich, 99%), and  $\text{Co}(\text{CH}_3\text{COO})_2\cdot 4\text{H}_2\text{O}$  (Sigma-Aldrich, reagent grade) in glycerol, with the molar ratio of metal to glycerol being 1:3.

The chemical reaction of the synthesized materials can be written as follows:



To compensate for the lithium loss which occurs at high annealing temperatures during powder processing, a 15% excess of lithium (Li/M=1.15:1) was added for all experiments. The metal acetates were mixed and then dissolved in glycerol with continuous stirring for about 2 hours to form a clear solution, to which an appropriate amount of corn starch was added at 80°C (corn starch/M=1:4 molar). After four hours of continued heating and stirring a thick gel was formed, at which point the temperature was increased to 250 °C for 6 hours until the thick gel had dried to an ultrafine powder. The dried powder was then pelletized and introduced into a heating furnace in the presence of air (using an alumina crucible) for 10 hours at 400°C to get rid of any organic residues and unevaporated water molecules. This was followed by further heating for 8 hours at a set of temperatures: 850°C (sample LMNC1), 900°C (LMNC2), 950°C (LMNC3), and 1000°C (LMNC4), all with a heating rate of 5°C/min and cooling

at room temperature. The resulting powders were then ground with a mortar and pestle, and subjected to characterization studies.

### 2.3.2 Materials Characterization

The concentrations of Li, Mn, Ni, and Co were measured by NexION 350D ICP-MS (PerkinElmer). The phase characterization of the synthesized LMNC materials was carried out using X-ray diffraction (XRD) measurement on a PANalytical X'Pert Multi-Purpose Diffractometer with the following measurement conditions: no monochromatic, nickel-filtered Cu  $k\alpha$  radiation ( $k\alpha_1=1.5405980 \text{ \AA}$  and  $k\alpha_2=1.5444 \text{ \AA}$ ) in the  $2\theta$  range from  $10^\circ$  to  $80^\circ$  with a scan rate  $0.02^\circ/\text{s}$ . The powder morphology and particle size of the synthesized materials were determined using an FEI Quanta 600 FEG Environmental Scanning Electron Microscope (SEM).

### 2.3.3 Electrode preparation and electrochemical characterization

The electrodes were prepared by mixing 80 wt.% of synthesized active material, 10 wt.% of carbon black (Vulcan XC-72) and 10 wt.% of polyvinylidene fluoride (PVDF) binder in N-methyl-2-pyrrolidinone (NMP). This slurry was mixed thoroughly and doctor-bladed onto a thin sheet of aluminum metal, then dried in a furnace ( $60^\circ\text{C}$  for 2 h), followed by drying in a vacuum oven ( $120^\circ\text{C}$  for 12 h) prior to assembling coin cells in an argon-filled glove box [48]. An 11-mm circular shape of the dried electrode was then cut and pressed (10 kN) over an Al mesh. The electrochemical characterizations were performed in CR 2032 cells. The coin cell was composed of the synthesized electrode as the cathode, lithium metal foil as the anode, and a porous



polypropylene separator (Celgard). 1.0 M  $\text{LiPF}_6$  in dimethyl carbonate (DMC) and ethylene carbonate (EC) was used as the electrolyte (DMC:EC = 1:1, v/v).

Electrochemical performance was tested using a charge-discharge study at a C/10 rate (up to 100 cycles), along with a rate capability test conducted at different current rates (C/10, C/5, 1C, 2C, 5C and back to C/10, where 1C=200 mA/g) and performed at room temperature over the potential range between 2.5 and 4.6 V using an Arbin battery tester. The other electrochemical characterizations, cyclic voltammetry (CV) in the potential range 2.5 to 4.6 V at the scanning rate of 0.1 mV/s, and electrochemical impedance spectroscopy (EIS) in the frequency range from 0.05 Hz to 1 MHz were performed using Gamry Reference 3000 Potentiostat/Galvanostat.

## 2.4 Results and Discussion

### 2.4.1 ICP-MS analysis

ICP-MS analysis results for LMNC1, LMNC2, LMNC3, and LMNC4 composites are shown in Table 2.1. The experimental data of Mn, Ni, and Co elements in one mole of the synthesized samples are in good agreement with the nominal values, Mn=0.33 mole, Ni=0.33 mole, and Co=0.33 mole. Non-stoichiometric lithium values are seen due to the 15% excess Li added to all samples in order to compensate for Li loss during calcination at high temperatures. As temperature increases from 850°C (LMC1) to 900°C (LMNC2), 950°C (LMNC3), and 1000°C (LMNC4), Li content decreases due to increased Li loss at high temperatures.

Table 2. 1 Li, Mn, Ni and Co experimental quantities in mole fraction, analyzed by ICP-MS.

Elements	LMNC1	LMNC2	LMNC3	LMNC4
Li	1.1105	1.1059	1.0782	1.0371
Mn	0.3422	0.3387	0.3423	0.3355
Ni	0.3218	0.3246	0.3243	0.3251
Co	0.3360	0.3367	0.3334	0.3394

#### 2.4.2 Powder characterization

Figure 2.1 (a) shows the XRD patterns of LMNC1, LMNC2, LMNC3, and LMNC4 layered structure cathode materials. Here the diffraction peaks are sharp and well defined and can be indexed based on the hexagonal  $\alpha$ -NaFeO<sub>2</sub> type that defines a metal oxide layered structure with an  $R3m$  space group. The formation of an ordered layered structure can be observed by the separation of (006)/(102) and (108)/(110) peaks of the hexagonal structure [49], as shown in Figure 1 (b) and (c). The separation of these peaks increases gradually with increasing temperature due to the proportional relationship of the nucleation growth rate to temperatures.

Lattice parameters  $a$  and  $c$  of the synthesized materials were estimated using PANalyticalX'Pert High Score and tabulated in Table 2.2 From the tabulated data in Table 2.1 it is clearly seen that the lattice parameter  $a$  for all four compounds increases with increasing the calcination temperature [32]. The lattice parameter  $c$  refers to the average metal inter-slab distance. A  $c/a$  ratio of 4.9 or greater, which all four samples possess, is found to be preferred for a well-defined hexagonal layered structure [50–

52]. In addition, the ratio of  $c/a$  increases gradually with increasing temperature from 900°C to 1000°C, which in turn increases the hexagonal layer orderliness of LMNC. Cationic mixing has been reported as the main cause of electrochemical performance deterioration in layered structures [53,54]. Ratios of  $[I(003)/I(104)]$  (R) and  $[(I(102)+I(006))/I(101)]$  (R') were calculated in Table 2.2, as these two parameters are sensitive to the degree of cation mixing in the lattice. Low cationic mixing can be obtained at an R-value of 1.2 or higher, and a lower R' [44].

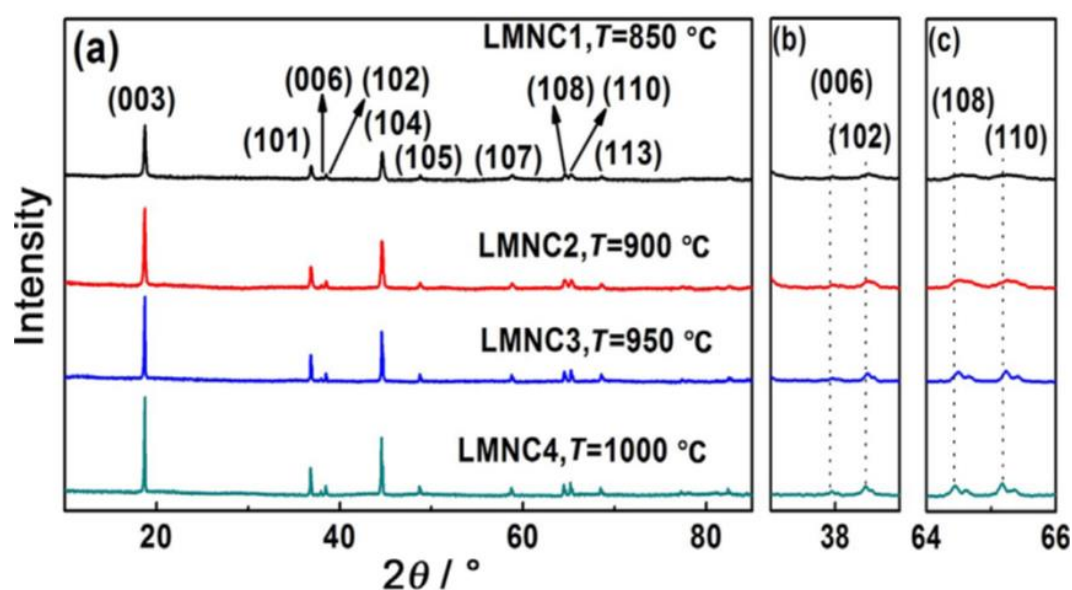


Figure 2. 1 XRD patterns of LMNC1, LMNC2, LMNC3, and LMNC4 material synthesized using the sol-gel method using glycerol as a solvent and cornstarch as a gelling agent for temperatures (a) 10–85°, (b) 37–39°, and (c) 64–66°.

These four samples show R values much greater than 1.2, which is favorable for low cationic mixing. The lowest R' (0.281) value was obtained from the LMNC1 sample along with the highest R (1.775); however, this sample also showed the lowest  $a$  value, indicating poorer Ni transport [37]. Of the other three samples, LMNC2 shows the highest R-value as well as the lowest R' value. It is clear from the R and R' values that the sample annealed at 900°C has the best-layered structure and is expected to have the best stability over cycling among the compounds chosen for this study.

Table 2. 2 Lattice parameters,  $c/a$  ratios,  $I(003)/I(104)$  (R), and  $(I(102)+I(006))/I(101)$  (R') intensity ratios for the synthesized samples.

Compound	$a$ (Å)	$c$ (Å)	$c/a$	R	R'
LMNC1	2.849653	14.218204	4.989	1.775	0.281
LMNC2	2.858029	14.213809	4.973	1.614	0.339
LMNC3	2.858292	14.219232	4.975	1.588	0.413
LMNC4	2.859232	14.226801	4.976	1.612	0.339

### 2.4.3 Particle size and morphology

The surface morphology of the LMNC1, LMNC2, LMNC3, and LMNC4 materials was examined with the use of SEM, as seen in Figure 2.2. In these images, ultrafine particles with grain boundaries are readily observed. The particle size appears to increase linearly with temperature, and spherical particles  $\sim 0.1$ -  $0.4 \mu\text{m}$  in size are seen in the LMNC1 and LMNC2 samples (Figure 2.2 (a, b)). For the LMNC3 and LMNC4 samples, the particle size increases significantly to  $\sim 0.4$  -  $3.2 \mu\text{m}$ , as seen in Figure 2 (c, d). The electrochemical reaction normally occurs at the particle surface and the ions are transported to the electrode materials afterward, so the higher surface area and shorter Li-ion diffusion path that small particles can provide [55] make them desirable [56]. However, in terms of safety and stability, nanosized particles are less ideal due to their high reactivity [7,57]. An intermediate particle size has therefore been shown to provide higher performance and longer cycling life for LMNC materials. Based on these results, and to be consistent with the trends observed from the XRD analysis, the synthesized material calcined at  $900^\circ\text{C}$  (LMNC2) with a nominal particle diameter of

0.3  $\mu\text{m}$  was expected to have the best electrochemical behavior over the other three samples tested.

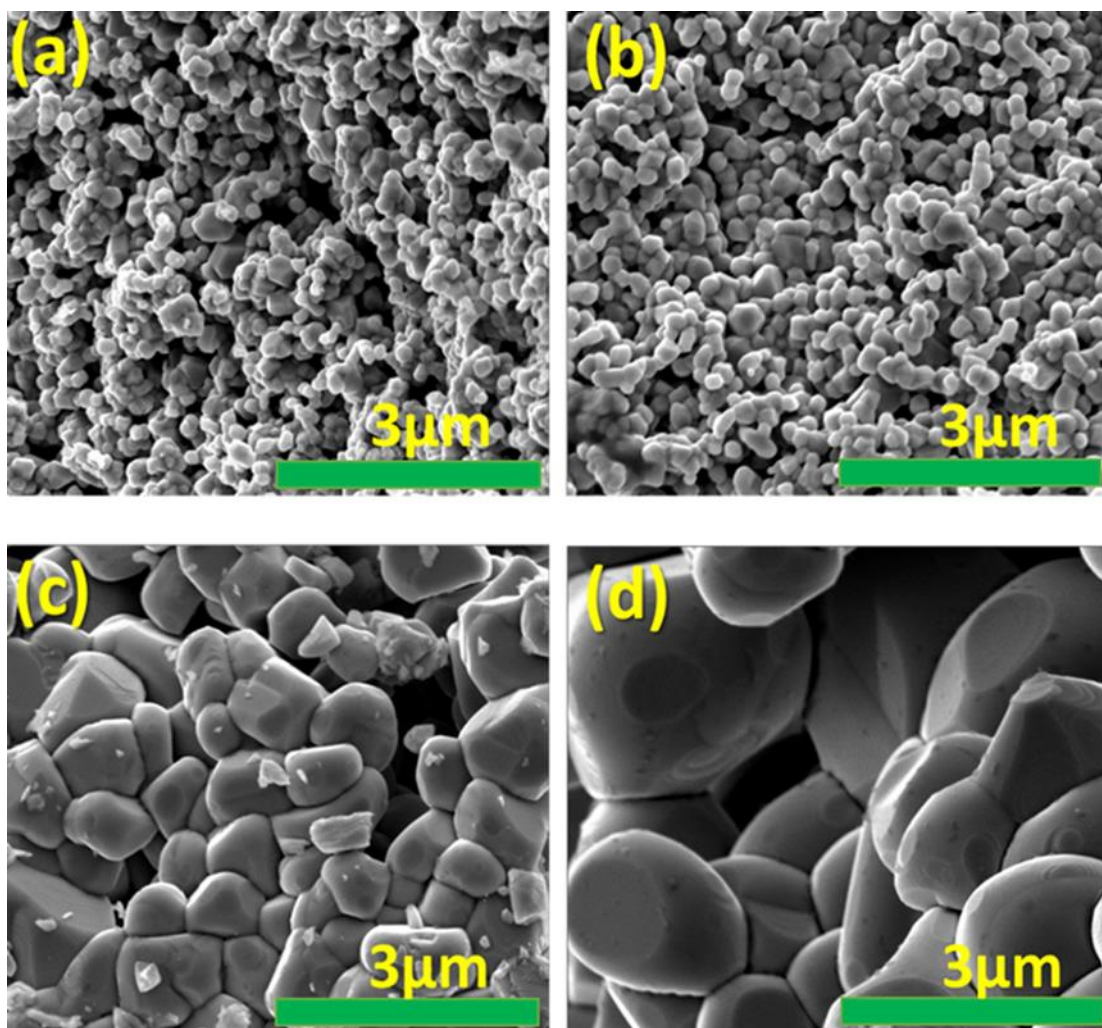


Figure 2. 2 SEM images of (a) LMNC1, (b) LMNC2, (c) LMNC3, and (d) LMNC4 compounds, showing different particle sizes.

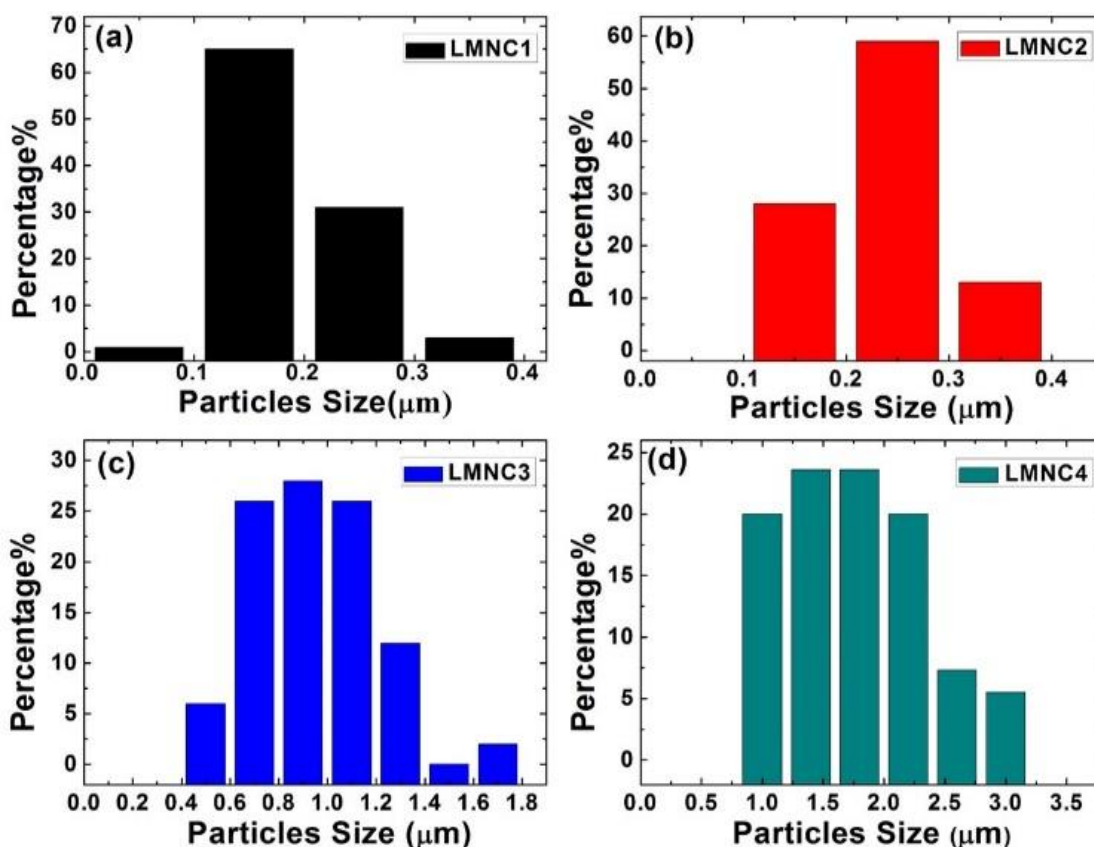


Figure 2. 3 Particle size distributions of (a) LMNC1, (b) LMNC2, (c) LMNC3, and (d) LMNC4 compounds.

The LMNC lithium-ion cathode materials synthesized via the sol-gel method have a broad particle size distribution. Figure 2.3 illustrates the particle size analysis of the four samples. It is clearly seen from this figure that LMNC2 has the highest intermediate particle size distribution at  $\sim 0.3 \mu\text{m}$  (Figure 2.3b). These size-reduced particles help to facilitate lithium ion diffusion in and out of the layered structure during discharge and charge cycling [58–60].

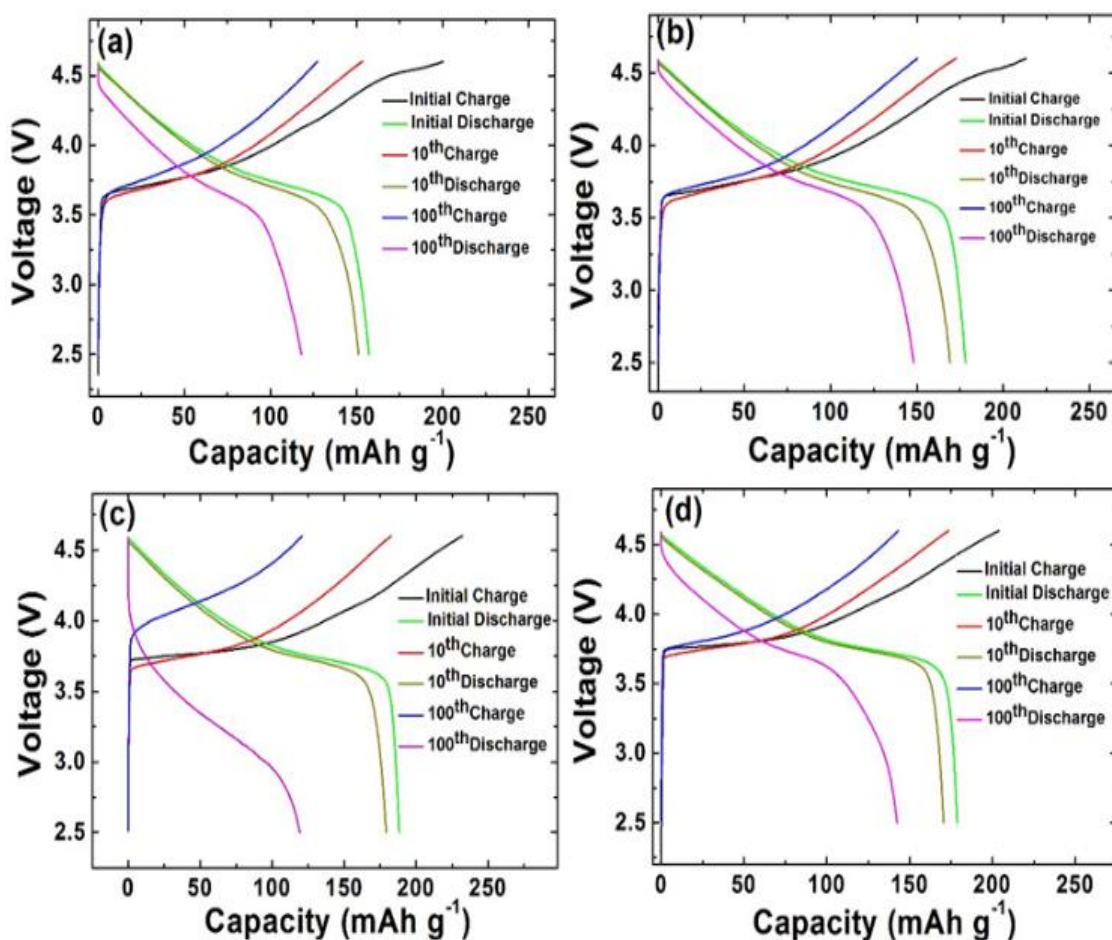


Figure 2. 4 Voltage profile of (a) LMNC1, (b) LMNC2, (c) LMNC3, and (d) LMNC4 at initial, 10th and 100th cycles and current density  $C/10$  with a potential range between 2.5 and 4.6V.

Similarly, the columbic efficiencies for LMNC1, LMNC2, and LMNC3, and LMNC4 after the 1<sup>st</sup>, 10<sup>th</sup>, and 100<sup>th</sup> cycles are (78.6, 98.7, 92.8) %, (83.6, 98.0, 100.0) %, (81.1, 98.1, 98.7) %, and (87.7, 98.3, 99.5) %, respectively. This indicates that LMNC2 has superior columbic efficiency over the other three cathode materials. Furthermore, all of the samples showed the ability to maintain a discharge plateau at  $\sim 3.8$  V and the absence of a charge plateau at  $\sim 4.0$  V over 100 cycles, with these being the main causes of structural changes [49,61]. The absence of a charge plateau at  $\sim 4.0$  V and the presence of a discharge plateau at  $\sim 3.8$  V eliminates the possibility of a layered to spinel structure change. It also demonstrates that  $Mn^{4+}$  contributed to the LMNC structural

stability [49,61]. To further investigate the rate capability and cycling performance, the coin cells were charged and discharged at C/10, C/5, 1C, 2C, 5C, and then back to C/10 between 2.5 and 4.6 V for 10 cycles each. Figure 5(a) illustrates the effect of discharge current on cell performance. LMNC2 shows the best discharge capacity at 5C, giving a value of 80.9 mAh/g, or about 45.4% of the C/10 value, which is much higher than that of LMNC1 (40.2%), LMNC3 (21.2%), or LMNC4 (31.3%). These results can be interpreted as electrode polarization being most affected by the particle size. The solid electrolyte interphase (SEI) layer thickness has been found to decrease linearly with increasing particle size [62]. Consequently, the coulombic efficiency of the synthesized materials increases proportionally with the particle size for LMNC1, LMNC2, and LMNC3 samples in the 1<sup>st</sup> cycle at C/10. For LMNC4, however, it starts decreasing again; this might be related to the very low surface area this material has. At a high rate, LMNC2, with optimum structural dimensions confirmed by XRD analysis and its intermediate nanoparticle size distribution (Figure 2.3(b)), gives the most desirable discharge capacity. Similarly, the cyclic performance of the coin cells charged and discharged over 100 cycles between 2.5 to 4.6 V at room temperature shows that the LMNC2 and LMNC4 samples retain nearly 83.7 and 79.7% of their capacity, respectively, while LMNC1 and LMNC3 samples show 74.5 and 63.4% retention, respectively (see Figure 2.5(b) and Table 2.3). Looking back to the parameters measured by XRD in Table 2.2 and excluding LMNC1 (lowest *a* value), LMNC2 and LMNC4 have the lowest cationic mixing, while LMNC3 has the highest. These results are consistent with the electrochemical performance of these samples. Thus, the discharge capacity depletion over cycling can be attributed to the side reactions between the active particles and the electrolyte [63].



Table 2. 3 Discharge capacity, capacity retention, and electrode-electrolyte film resistance exhibited by LMNC1, LMNC2, LMNC3, and LMNC4.

Compound	1 <sup>st</sup> Discharge (mAh/g)	10 <sup>th</sup> Discharge (mAh/g)	100 <sup>th</sup> Discharge (mAh/g)	Efficiency after 10 cycles (%)	Efficiency after 100 cycles (%)	Before 1 <sup>st</sup> cycle ( $R_{CT1}$ ) (ohm)	After 10 <sup>th</sup> cycle ( $R_{CT2}$ ) (ohm)	After 100 <sup>th</sup> cycle ( $R_{CT3}$ ) (ohm)
LMNC1	158.28	153.22	117.97	96.9	74.5	575.4	26.9	121.4
LMNC2	177.17	169.28	148.22	95.5	83.7	735.8	29.2	45.6
LMNC3	188.22	179.13	119.28	95.2	63.4	458.7	35.3	87.3
LMNC4	178.69	170.47	142.39	95.4	79.7	135.7	16.7	73.8

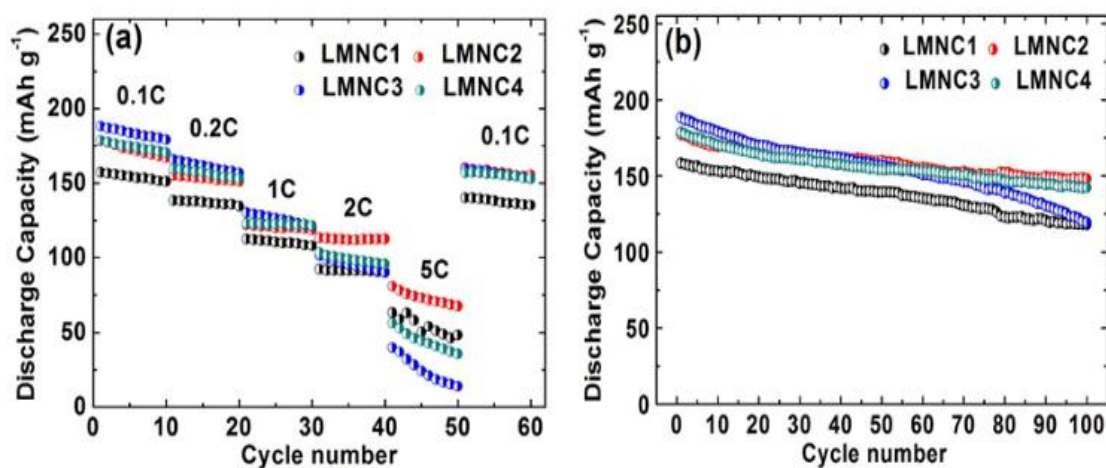


Figure 2. 5 (a) Rate capability behavior of LMNC1, LMNC2, LMNC3, and LMNC4, (b) Discharge behavior of LMNC1, LMNC2, LMNC3, and LMNC4 cathodes (C/10 rate).

Cyclic voltammetry (CV) tests were carried out between 2.5 and 4.6V with a 0.1 mV/s scan rate. These results are shown in Figure 6 and clearly demonstrate the presence of 3.8/3.7 and 4.6/4.5 couples (excluding the forming cycles), which are attributable to Ni<sup>2+</sup>/Ni<sup>4+</sup> / Ni<sup>4+</sup>/Ni<sup>2+</sup> and Co<sup>3+</sup>/Co<sup>4+</sup> / Co<sup>4+</sup>/Co<sup>3+</sup>, respectively.[31] These peaks confirm the presence of Ni and Co with 2+ and 3+ valence states, while Mn with a 4+ valence state is inactive, contributing to the absence of the plateau at 4.0 V (Figure 2.6 (a, d)).

LMNC1 shows the highest oxidation reaction after 4.5 V due to the insufficient diffusion time of  $\text{Li}^+$  within the layered structure, which results in an oxygen loss from the structure, accompanied with lithium. Consistent with the ICP-MS results in Table 1, the maximum peak after 4.5 V is associated with LMNC1 (with the highest amount of Li) and it starts decreasing in the samples until LMNC4 (lowest amount of Li), confirming our earlier speculation about Li loss during calcination in the form of  $\text{Li}_2\text{O}$  from the layered structure. Furthermore, the peak current densities of LMNC3 are larger than those of the other samples, confirming that LMNC3 has the highest discharge capacity within the first 10 cycles. LMNC1, on the other hand, gives the smallest current peak density due to the high amount of Li lost in the first cycle, a result of incomplete diffusion of the lithium ion inside the hexagonal layered structure (Figure 2.6 (b)). This further explains the result seen in Figure 2.4 (a), where a 21.4% capacity loss is associated with the LMNC1 sample.

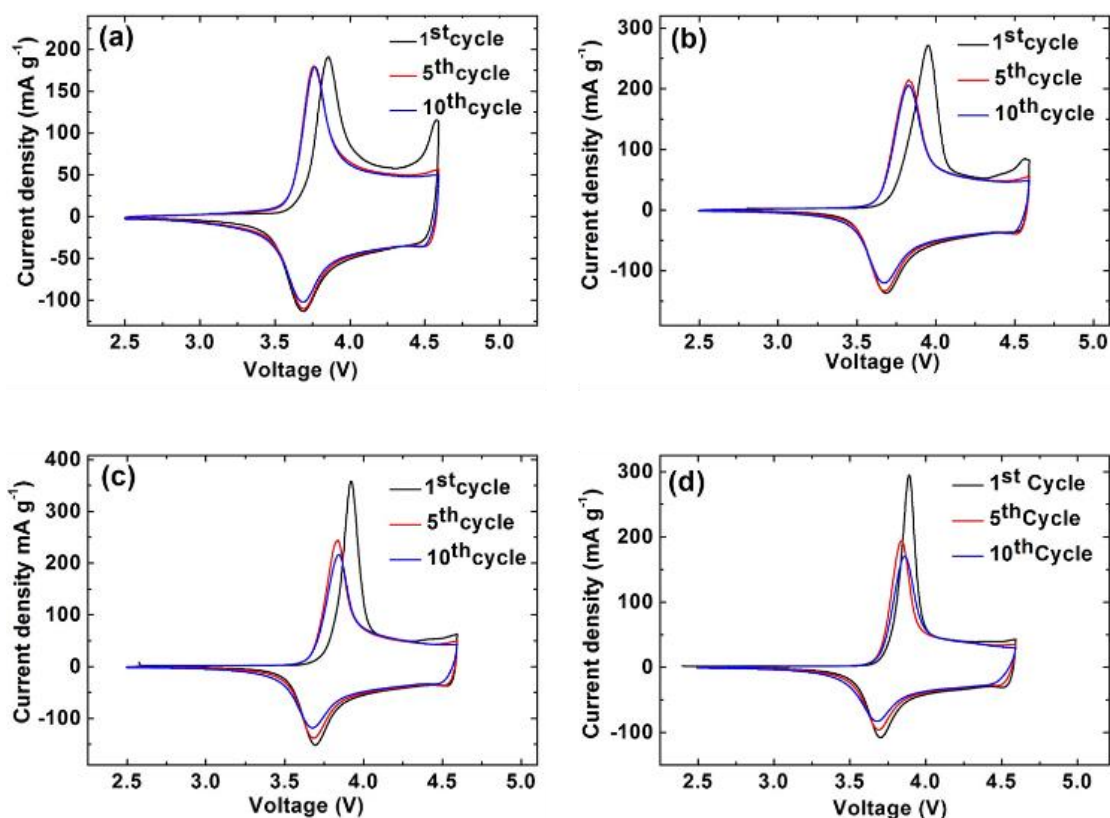


Figure 2. 6 CV curves of (a) LMNC1, (b) LMNC2, (c) LMNC3, and (d) LMNC4 electrodes, with a potential range 2.5 - 4.6 V.

To provide additional information about the electrochemical behavior of the synthesized materials and the differences between them after cycling, electrochemical impedance spectroscopy (EIS) was carried out, for which the results are presented in Figure 2.7 and Table 3. Although LMNC4 material exhibits the lowest charge transfer resistance ( $R_{CT}$ ) before the 1<sup>st</sup> cycle ( $R_{CT1}$ ) and after the 10<sup>th</sup> cycle ( $R_{CT2}$ ) ( $135.7 \Omega$  and  $16.7 \Omega$ , respectively), the lowest ( $R_{CT3}$ ), or charge transfer resistance after 100 cycles, of was observed for the LMNC2 electrode ( $45.6 \Omega$ ).

It should also be noted that using glycerol as a solvent in the synthesis, as compared to water, was demonstrated to be more advantageous in both electrochemical efficiency and energy consumption as shown in Table 2.4. In general, the time required for heat treatment of NMC material from a water-based process is around 12 hours or more.

Using glycerol as a solvent decreases the heat treatment time to 8 hours, and therefore requires much less energy consumption. Additionally, the capacity fade was reduced to about 16.3% over 100 cycles for LMNC2. This can be attributed to the additional heat produced from combustion during the glycerol preparation steps, making partially crystalline nanoparticles more likely to be obtained before calcination at high temperature. Because of this, shorter heat treatments are needed to have fully crystalline nanoparticles, as compared with water which produces amorphous nanoparticles needing long-term heat treatment to get the desired structures. The time factor in high-temperature heat treatment is critical, as it not only affects the feasibility but can also increase Ni<sup>2+</sup> migration in the Li<sup>+</sup> layer since both have a similar ionic radius. This can result in blockage of the Li<sup>+</sup> diffusion path and cause deterioration in capacity retention during long-term cycling.

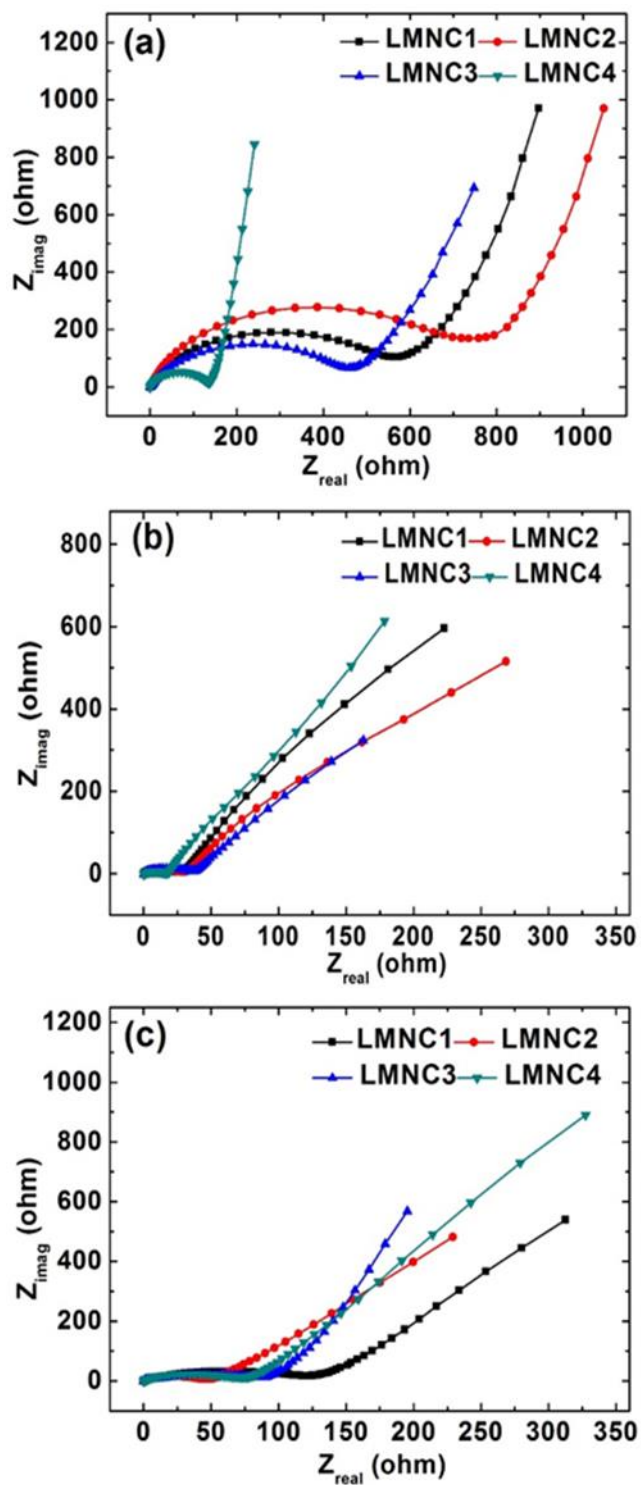


Figure 2. 7 Impedance plots of LMNC1, LMNC2, LMNC3, and LMNC4 electrodes before the 1st cycle (a), after 10 cycles (b), and after 100 cycles (c), respectively.

Table 2. 4 Comparison of using different solvents in synthesizing  $\text{LiMn}_{1/3}\text{Ni}_{1/3}\text{Co}_{1/3}\text{O}_2$  cathode materials via sol-gel method.

Solvent	Gelling agent	Temperature (°C) / Time (hr.)	Initial discharge Capacity (mAh/g)	Final discharge Capacity (mAh/g)	Number of cycles	Capacity fade (%)	References
Glycerol	Cornstarch	900/8	177.17	148.22	100	16.3	This study
Water	Citric acid	850/16	199.9	143.6	80	28.2	Wang, et al. / 2016 [64]
		900/16	188.9	138.7		26.6	
Water	Citric acid	850/12	167	129	30	22.8	N. Kalaiselvi, et al. /2014 [65]
Water	Cornstarch	850/12	171	141	100	17.5	N. Kalaiselvi, et al./2013 [66]

## 2.5 Conclusions

Layered  $\text{LiMn}_{1/3}\text{Ni}_{1/3}\text{Co}_{1/3}\text{O}_2$  (LMNC) cathode material was successfully synthesized using glycerol as a solvent via a sol-gel method. With heat treatments at different temperatures, it was demonstrated that the sample treated at 900° C (LMNC2) gave the best electrochemical performance. LMNC2 showed a particle size distribution ranging from 0.1 - 0.3  $\mu\text{m}$ , desirable for allowing isotropic lithium-ion transport during intercalation/de-intercalation through charge-discharge processes. This material exhibited excellent crystallinity with a highly ordered layered structure that is necessary for optimal performance. LMNC2 showed an exceptional initial discharge capacity of 177.1 mAh/g at C/10, and a discharge capacity of 148.2 mAhg-1 after 100 cycles, with 83.7% capacity retention. Furthermore, it shows an 80.9 mAh/g discharge capacity after 50 cycles at 5C. These results indicate that using glycerol as a solvent to produce

LMNC cathode materials via the sol-gel method along with a 900°C heat treatment can significantly improve the electrochemical performance of LMNC materials.

## 2.6 Acknowledgements

The authors would like to thank Dr. Eric Bohannon for his help in obtaining XRD results and Dr. Honglan Shi with ICP-MS analysis. They acknowledge partial financial support from the Vehicle Technologies Office of the U.S. Department of Energy (under grant #DE-EE0007282) and the University of Missouri. K.I.H. would like to thank the Higher Committee for Education Development in Iraq (HCED) for providing a scholarship.

## **Chapter 3. The Effect of Cobalt and Nickel Contents on the Performance of Lithium Rich Positive Electrode Materials for Lithium-Ion Battery**

Published in the Journal of the Electrochemical Society doi: 10.1149/2.0311811jesJ. Electrochem. Soc. 2018 volume 165, issue 11, A2470-A2475

### **3.1 Abstract**

Lithium-rich cathode materials in the form of  $\text{Li}_{1.2}\text{Mn}_{0.51}\text{Ni}_{0.145+x}\text{Co}_{0.145-x}\text{O}_2$  ( $x = 0$  (LR2), 0.0725 (LR1)) have been successfully synthesized by a sol-gel method using glycerol as a solvent. These materials were characterized by X-ray diffraction (XRD), scanning electron microscopy (SEM), and electrochemical measurements. XRD patterns showed that both materials have typical diffraction peaks of a Li-rich material with a well-crystallized structure, but the LR1 sample with less Co has a well-distinguished  $\text{Li}_2\text{MnO}_3$  peak between  $20^\circ$ – $25^\circ$ . SEM images show that LR1 also has a more uniform particle distribution. Electrochemical measurements revealed that LR2 has a higher initial discharge capacity of 223 mAh/g than that of LR1 of 185 mAh/g at 0.1 C between 2 and 4.8 V. However, LR1 was observed to have an increasing capacity over several dozen cycles. The specific discharge capacity of LR1 increased from 185 to 213 mAh/g after 20 cycles. This is ascribed to a gradual activation of the Li-rich phase from the surface of the particles. It is shown that the smaller Co/Mn ratio (1:7.134) of LR1 plays an important role in its continuous activation. Its capacity retention is 98% at 100 cycles at a 1C rate, better than that of LR2 and most previously reported lithium-rich materials.



### 3.2. Introduction

Rechargeable lithium-ion batteries (LIBs) with more manganese contents have been introduced as a candidate for power storage in portable electronic devices, electric vehicles, and hybrid electric vehicles [67,68]. Due to their high capacity, less toxicity and lower cost comparing with LiCoO<sub>2</sub>, layered lithium metal oxides with a LiMO<sub>2</sub> (M = Mn, Ni, Co) formula have been widely used with a discharge capacity between 160 and 180 mAh/g [26,69–71]. The global demand for energy has increased so rapidly that developing new cathode materials for LIBs as energy storage devices are in great need. Li-rich materials that can provide higher specific capacities have motivated many researchers to work on them. In this aspect, extensive studies have revealed that using Li<sub>2</sub>MnO<sub>3</sub> along with LiMO<sub>2</sub> can enhance its discharge capacity by extracting more lithium as this material can be activated between 4.5 and 4.8 V. It was also proved to be a structural stabilizer for LiMO<sub>2</sub> [72]. Due to their high capacity of over 200 mAh/g with a potential higher than 3.5 V, Li-rich materials with a formula of xLi<sub>2</sub>MnO<sub>3</sub> · (1-x)LiMO<sub>2</sub> (M = Co, Fe, Ni, Mn, etc.) have been investigated. The Li<sub>2</sub>MnO<sub>3</sub> phase with a C<sub>2/m</sub> space group can be highly integrated with R $\bar{3}$ m in LiMO<sub>2</sub> phase. The Li-rich cathode materials are electrochemically activated when they initially charge to above 4.5V by removal of lithium accompanying oxygen (Li<sub>2</sub>O)[73–75]. Releasing of irreversible lithium ions in Li<sub>2</sub>O because of Li<sub>2</sub>MnO<sub>3</sub> activation thus provides a higher initial specific discharge capacity, followed by a significant increase in the following cycles. This sudden change in specific discharge capacity is attributed to the activation process of Li<sub>2</sub>MnO<sub>3</sub> in the first cycle accompanied with irreversible oxygen loss from the Li<sub>2</sub>MnO<sub>3</sub> lattice, reducing the oxidation states of the transition metals in the second cycle [76,77]. Although the remarkable specific capacity in lithium-rich materials has

been achieved, Li-rich cathode materials still face challenges, such as safety problems from the releasing of nominal “Li<sub>2</sub>O” during Li<sub>2</sub>MnO<sub>3</sub> activation in the first charge cycle [77], poor long term cycling stability, voltage fade over cycling [78], and low rate capability caused by the insulation nature of Li[Li<sub>1/3</sub>Mn<sub>2/3</sub>O<sub>2</sub>] [79]. Fortunately, using a suitable molar ratio of (Ni+Co)/Mn was shown to enhance the structural stability during cycling [73,79]. Cycling stability and rate performance have been significantly improved by making “smart microstructures” or by using an efficient surface coating [71–73]. However, understanding the mechanism of structure evolution during cycling accompanied by the ultrahigh reversible capacity have not been fully understood, partly due to the complicated compositions and crystalline structures of Li-rich materials [80,81]. Attention has recently been paid to reducing the Co contents due to its relatively high toxicity and cost; a low Co/Mn ratio of 1/6 was studied [82]. This small molar ratio was found to be beneficial in enhancing electrochemical behavior and specific capacity in the Li-rich cathode materials. The phenomenon of capacity increase upon cycling (CIUC) has been observed in Li-rich materials. It was also observed in Fe<sub>3</sub>O<sub>4</sub> [83] and CoO [84], but the reasons for the CIUC are different from the Li-rich cathode materials [85–88]. For instance, a recent study suggested that the increment in specific discharge capacity from 187 to 194 mAh/g in the first 20 cycles was due to continuous activation of the remaining Li<sub>2</sub>MnO<sub>3</sub> upon cycling [89]. Another study proposed that the increase in discharge capacity was due to particle size effect in the first 40 cycles in Ni-doped Li-rich cathode materials [85]. In this study, we reported the synthesis of Li<sub>1.2</sub>Mn<sub>0.51</sub>Ni<sub>0.145+x</sub>Co<sub>0.145-x</sub>O<sub>2</sub> (x = 0 (LR2) or 0.0725 (LR1)), using a newly developed sol-gel technique with glycerol as a solvent and cornstarch as a gelling agent [90]. It was previously observed that morphology of semi-spherical particles can be produced with a 1:1 ratio [90], and rectangular nanorods can be made with more Ni

content than Co [91,92]. The two specific compositions were chosen to study the morphology changes where the Co/Ni molar ratios are 1:1 in LR2 and 1:3 in LR1. In such a way the shape of the particles is expected to change from semi-spherical to rectangular prism nanorod and hexagonal prism nanorod particles, which would shorten the Li<sup>+</sup> diffusion path and enhance the electrochemical performance. The two samples also have different Co/Mn molar ratios, with LR1 at 1:7.134 and LR2 at 1:3.520 from compositional chemical analysis. The influence of the different Co/Mn molar ratios on particle size, and ultimately on the electrochemical performance, was studied and reported herein.

### 3.3. Experimental

#### 3.3.1. Powder synthesis

$\text{Li}_{1.2}\text{Mn}_{0.51}\text{Ni}_{0.145+x}\text{Co}_{0.145-x}\text{O}_2$  (LR2 with  $x = 0$  or LR1 with  $x = 0.0725$ ) cathode materials were synthesized by a previously developed sol-gel method using glycerol as a solvent to replace water [90]. This technique was demonstrated to be a viable technique to prepare transition metal oxide powders for Li-ion battery. Briefly, glycerol is used to dissolve metal salts to form a salt solution and cornstarch is used as a gelling agent. In the current work stoichiometric amounts of  $\text{Li}(\text{CH}_3\text{COO})_2 \cdot 2\text{H}_2\text{O}$  (Aldrich, reagent grade),  $\text{Mn}(\text{CH}_3\text{COO})_2 \cdot 4\text{H}_2\text{O}$  (Aldrich, 99%),  $\text{Ni}(\text{CH}_3\text{COO})_2 \cdot 4\text{H}_2\text{O}$  (Aldrich, 99%) and  $\text{Co}(\text{CH}_3\text{COO})_2 \cdot 4\text{H}_2\text{O}$  (Aldrich, reagent grade) were used without further purification. These chemicals were dissolved in glycerol at 100°C with magnetic stirring. To the colored but clear solution, an appropriate amount of cornstarch (molar ratio of cornstarch/M<sup>+</sup> = 1/4) was added at 80°C with a high-speed mixing. Sol-gel forms after 3–4 hours. The temperature was further increased to 250°C to make a dry powder. The dry powder was then pelletized and subjected to a high-temperature heat-

treatment in two consecutive stages with a 5°C/min temperature ramping in heating and allowing natural cooling. The first stage was carried out at 400°C for 8 hours to get rid of unevaporated organic components, followed directly by the second stage annealing at 900°C for 12 hours to obtain the desired crystalline structure of the Li-rich cathode materials. The synthesized powder afterward was grounded and used for further testing.

### 3.3.2. Materials characterization

The Li, Mn, Ni, and Co content in the materials were measured by NexION 350D ICP-MS (induction coupled plasma –mass spectroscopy) (PerkinElmer). To identify the crystalline phase and cationic ordering, X-ray diffraction (PANalytical X'Pert Multi-Purpose Diffractometer) was used. The XRD spectra were detected with the following measurement conditions: nickel-filtered Cu  $k\alpha$  radiation ( $k\alpha_1 = 1.5405980 \text{ \AA}$  and  $k\alpha_2 = 1.5444 \text{ \AA}$ ) and  $2\theta$  values ranging from 10° to 80° with a scan rate of 0.02°/s. An Environmental Scanning Electron Microscope (SEM, FEI Quanta 600 FEG) was used to observe particle size distribution and morphology of the synthesized cathode materials. The surface area of powders was characterized by BET surface analysis using a surface analyzer (3Flex, Microtronics).

### 3.3.3. Electrochemical measurements

The electrochemical measurements were carried out using CR 2032 coin cells. The cathodes materials were prepared by mixing 80% (by weight) active material, 10% carbon black and 10% polyvinylidene fluoride (PVDF) binder, with a suitable amount of N-methyl-2-pyrrolidinone (NMP). The mixed materials were cast on Al foil with a current collector and dried in a vacuum furnace at 60°C for 2 hr, followed by drying in

a vacuum furnace at 120°C for 12 hr. Prior to final assembly, 7/16 inch of the prepared electrode was punched and pressed (10 kN) between two aluminum meshes. Cell assembly was carried out in an argon-filled glove box (MBRAUN). The synthesized electrode was used as the cathode and lithium metal foil as the anode. The cathode and the anode were separated by a porous polypropylene separator (Celgard); the electrolyte was composed of 1.0 M LiPF<sub>6</sub> in dimethyl carbonate (DMC) and ethylene carbonate (EC) with a volume ratio of DMC: EC = 1:1. The electrode loading was 2.48 mg for LR1 and 2.56 mg for LR2. The charge-discharge cycles were carried out using an Arbin battery tester (Model BT-2043) at room temperature. The voltage ranged from 2.0 V to 4.8 V with a current density at 0.1 C (1C = 200 mA/g). Rate capabilities were studied at different current densities (0.1C, 0.2C, 1C, 2C and 5C). Cyclic voltammograms (CVs) were obtained in the potential range of 2 to 4.8 V at a scanning rate of 0.1 mV/s using a potentiostat/galvanostat (Camry Reference 3000). Electrochemical impedance spectroscopy (EIS) in the frequency range from 0.05 Hz to 1 MHz was used to investigate the impedance of the synthesized materials.

### 3.4. Results and discussion

#### 3.4.1. ICP-MS analysis

ICP-MS analysis results of LR1 and LR2 composites are shown in Table 3.1. The experimental data of mole fractions of both samples are in good agreement with the nominal values. The consistent chemical compositions demonstrate the successful synthesis of the new sol-gel method using glycerol to replace water as a solvent. The Co/Mn ratios from the chemical analysis are 1:7.134 and 1:3.520 for LR1 and LR2, respectively.

Table 3. 1 Mole fractions of Li, Mn, Ni, and Co analyzed by ICP-MS

Element	LR1		LR2	
	Nominal	Experimental	Nominal	Experimental
Li	1.2	1.178	1.2	1.193
Mn	0.51	0.5201	0.51	0.514
Ni	0.2175	0.2070	0.145	0.140
Co	0.0725	0.0729	0.145	0.146

### 3.4.2. Material characterization

The XRD patterns of LR1 and LR2 are shown in Figure 3.1. Based on the  $\alpha$ -NaFeO<sub>2</sub> structure, the strong showing typical diffraction peaks of Li-rich materials. diffracted peaks can be indexed to the layered hexagonal lattice with  $R\bar{3}m$  space group. The region between 20° and 25° shows a weaker peak, identified as the (020) reflection of the super lattice structure. It is indicative that the in-plane ordering of Li/Mn is similar to those of Li<sub>2</sub>MnO<sub>3</sub>[93–95]. The clear splitting of (006)/(012) and (108)/(110) doublets of the as-prepared cathode materials indicates that they have a well-organized layered structure [96]. The intensity ratio of I(003)/I(104) (>1.2) was found to be related to the low cation mixing [96]. Due to their similar ionic radii, Ni<sup>2+</sup> and Li<sup>+</sup> can substitute in each other's position in the layered structure, leading to blocking of the Li<sup>+</sup> diffusion path and decreasing electrochemical performance over cycling. Compared with the LR2 material, LR1 exhibits better cationic ordering due to the higher ratio of I(003)/I(104) (= 1.7736).

Table 3.2 shows the lattice parameters for the synthesized cathode materials. The lattice parameters (*a*, *b* and *c*) were calculated using Lattice parameters *a* and *c* of the synthesized materials were calculated using PANalytical X'Pert High Score, where *a*

represents the interlayer metal-metal distance and  $c$  corresponds to the inter-slab distance [97]. The “ $a$ ” parameter is related to the Ni and Co compounds in the layered structure and found to be proportional to Ni content and reciprocal to Co content [98]. The data reveal that the “ $a$ ” parameter of LR1 is higher than that of LR2, in good agreement with the initial stoichiometric quantities of Ni and Co in LR1 and LR2. The inter-slab distance “ $c$ ” is also higher in LR1 than in LR2 because of the larger ionic radius of  $\text{Ni}^{2+}$  (0.69 Å) than that of  $\text{Co}^{3+}$  (0.545 Å). Consequently, LR1 has better  $\text{Li}^+$  insertion and extraction diffusion paths and is expected to have better performance during the charge-discharge processes than LR2. Furthermore, the  $c/a$  ratio greater than 4.9 was found to be preferred for well-ordering cations [95]. Both materials show values larger than 4.9 with good ordering.

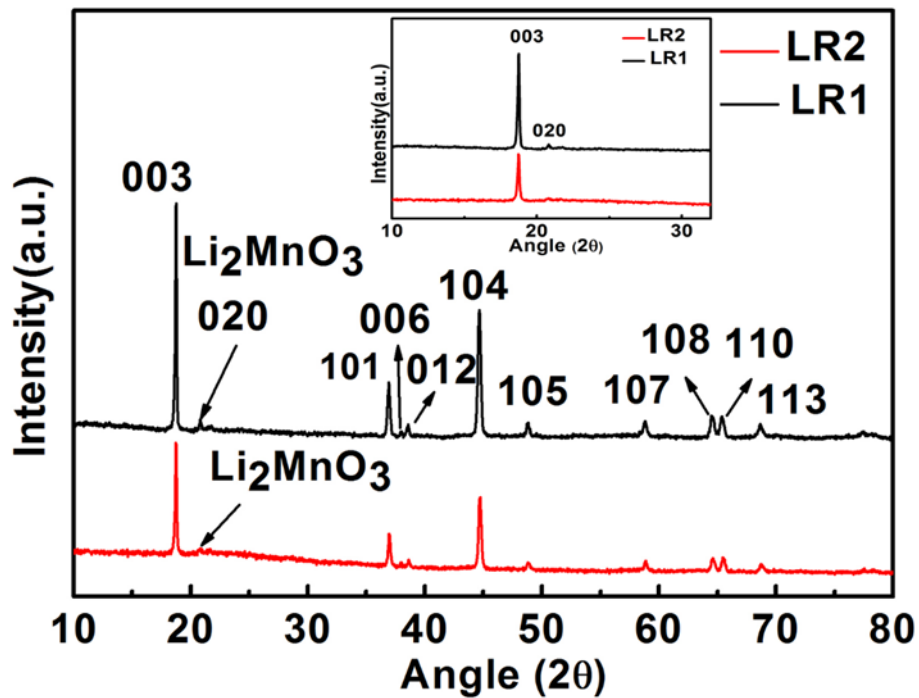


Figure 3. 1 XRD patterns of as prepared LR1 and LR2 cathode materials.

Table 3. 2 The crystal structure parameters of the prepared Li-rich cathode materials

Component	$a$ (Å)	$c$ (Å)	$c/a$	$I_{(003)}/I_{(004)}$
LR1	2.8552	14.2299	4.984	1.7736
LR2	2.8525	14.2193	4.985	1.6406

### 3.4.3. Morphology characterization

The particle sizes and size distributions of the as-prepared cathode materials were analyzed by SEM with different magnifications as shown in Figure 3.2. The SEM images illustrate that LR1 has rectangular prism nanorod and hexagonal prism nanorod particles ranging from 0.35 to 0.88  $\mu\text{m}$  in agglomerates, while LR2 has semi-spherical particles between 0.18 and 0.36  $\mu\text{m}$ . The rectangular and hexagonal prism nanorods with a short b-axis distance were found to be advantageous for  $\text{Li}^+$  diffusion path during charge/discharge cycles [99]. Although LR1 has larger particle sizes (thus lower surface area) than LR2, LR1 has a desirable morphology favoring a smooth path for  $\text{Li}^+$  diffusion in the host material. BET surface analysis results show that this newly developed technique produces a proportionally lower surface area of 1.73  $\text{m}^2/\text{g}$  for LR1 and of 3.45  $\text{m}^2/\text{g}$  for LR2. The BET results show that they are consistent with the particle sizes obtained from the electron microscopy imaging and are larger than other Li-rich cathode materials [100]. In this regard, the relatively larger particle size with the smaller surface area would suppress the phase transformation and improve the cycling stability.



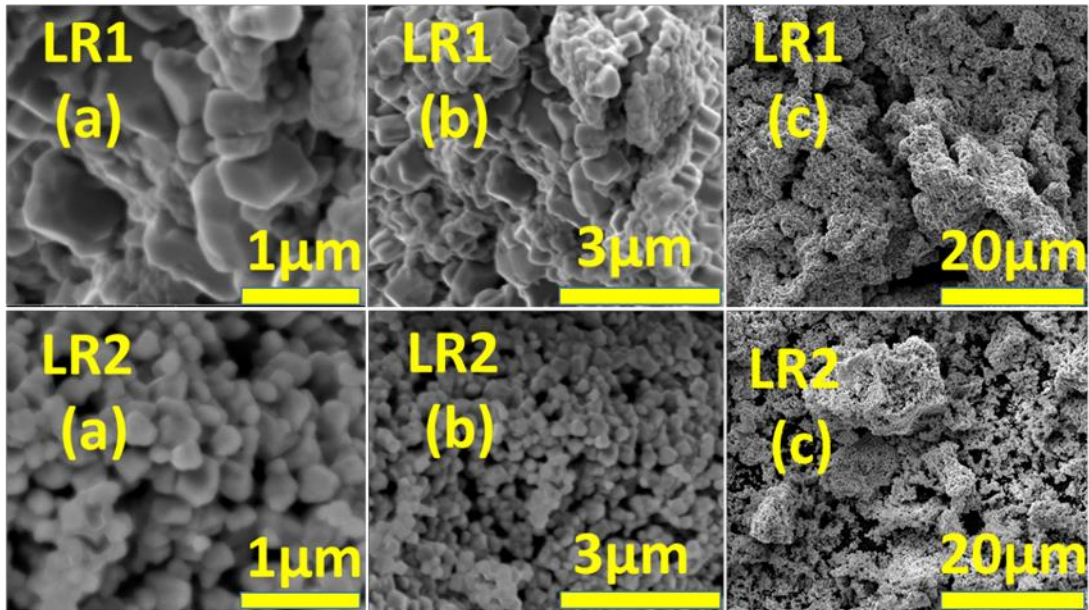


Figure 3. 2 SEM images of LR1 and LR2 at different magnifications.

#### 3.4.4. Electrochemical characterizations

The first, 30<sup>th</sup>, and 60<sup>th</sup> charge and discharge curves of LR1 and LR2 at a 0.1C rate and a potential range of 2.0–4.8 V are shown in Figure 3.3. It can be clearly seen that the initial charge capacity is divided into two regions corresponding to different chemical reactions for both materials. The first region below 4.5 V corresponds to transition metal oxidation reaction ( $\text{Ni}^{2+/4+}$  and  $\text{Co}^{3+/4+}$ ) [101,102]. The other reaction region appeared above 4.5 V is related to the activation process of  $\text{Li}_2\text{MnO}_3$ , resulting in releasing irreversible  $\text{Li}^+$  from both layered structure and  $\text{Li}_2\text{MnO}_3$  sites along with oxygen in the form of  $\text{Li}_2\text{O}$  [103,104]. As it is clearly seen from this figure, the second plateau of LR2 material is longer than that of LR1, which means that the oxidation reaction of transition metals in LR2 is better than in LR1. This can be attributed to the  $\text{Co}^{3+/4+}$  eg band that is partly overlapped with the top of the  $\text{O}^{2-}$  2p band, making it possible to extract more  $\text{Li}^+$  from both phases (Li-rich phase and Li-layered phase) in the first charge cycle [105–107].

Due to its higher specific surface area based on SEM images and BET, LR2 has a relatively higher initial charge capacity of 315.2 mAh/g and a discharge capacity of 223.4 mAh/g with less irreversible capacity loss of 29.1%, while LR1 has 275.9 mAh/g initial charge capacity and 185.1 mAh/g initial discharge capacity with 32.9% capacity loss during the first cycle as shown in Table 3.3. For the subsequent cycles, however, unlike normal cathode materials which would experience full activation of the  $\text{Li}_2\text{MnO}_3$  phase in the first charge cycle, both LR1 and LR2 still have the two plateau regions in the subsequent charging cycles. LR1 show a little longer reaction distances in both regions than those in LR2 on the 60<sup>th</sup> cycle as seen in Figure 3.3. This result in contrast to that observed in the 1st cycle is indicative of slow activation indeed occurred better in LR1 than in LR2.

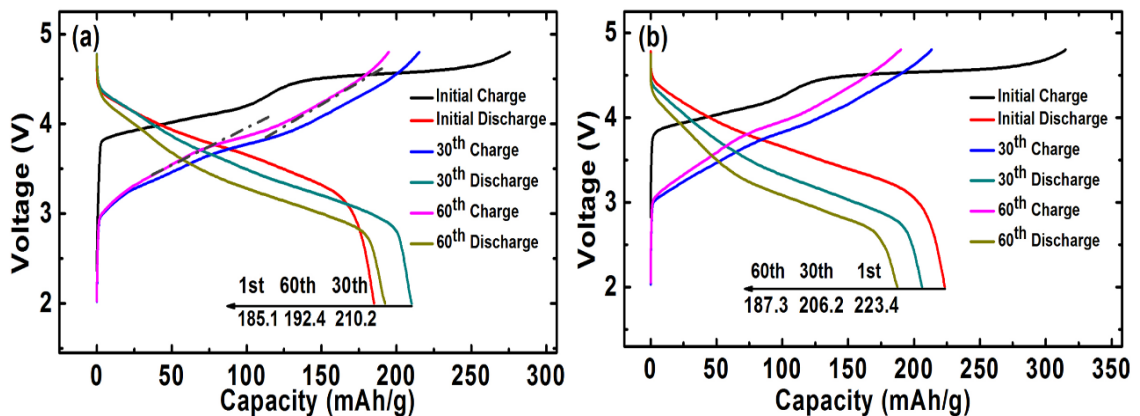


Figure 3. 3. The initial, 30<sup>th</sup> and 60<sup>th</sup> charge-discharge profiles at 0.1 C of (a) LR1 and (b) LR2. The broken lines in (a) on the 60<sup>th</sup> charge curve are to show that there still exist two regions, with the right indicative of the existence of activation.

Table 3. 3. First, 30<sup>th</sup> and 60<sup>th</sup> charge and discharge capacities and capacity losses.

Material	First cycle			30 <sup>th</sup> cycle			60 <sup>th</sup> cycle		
	Charge (mAh/g)	Discharge (mAh/g)	Capacity lost (%)	Charge (mAh/g)	Discharge (mAh/g)	Capacity lost (%)	Charge (mAh/g)	Discharge (mAh/g)	Capacity lost (%)
LR1	275.9	185.1 ± 5.0	32.9	215.3	210.3 ± 0.6	2.32	194.9	192.4 ± 1.3	1.29
LR2	315.2	223.4 ± 1.5	29.1	213.4	206.2 ± 2.8	3.37	190.1	187.3 ± 1.3	1.46

The larger particles in LR1 material also played an important role in inhibiting total activation of Li<sub>2</sub>MnO<sub>3</sub> in the first cycle, which led to an increase in specific capacity in subsequent cycles. Accordingly, the discharge capacity of LR1 in the 30<sup>th</sup> cycles jumped to 210.3 mAh/g with 2.32% capacity loss, while the LR2 discharge capacity decreased to 206.2 mAh/g with 3.37% capacity loss. The irreversible capacity decreased even further in the 60<sup>th</sup> cycle in LR1 to 1.29%, as compared to 1.46% in LR2. This observation is in agreement with a previous report suggesting that large particle sizes can suppress the total structural change in the first cycle in Li-rich cathode materials [85].

The cycling performances at 0.1 C in the potential range of 2.0–4.8 V are shown in Figure 3.4a. Although LR2 delivers the higher initial discharge capacity of 223.4 mAh/g than LR1 of 185.1 mAh/g, the first 15<sup>th</sup> cycles showed that LR1 discharge capacity increased to 214.86 mAh/g, while the discharge capacity of LR2 material increased to 228.17 mAh/g in the first 3 cycles and then started to decrease. The capacity retention of LR1 from 15<sup>th</sup> to 48<sup>th</sup> (200.86 mAh/g) cycles is about 93.5%, while in LR2 from 3<sup>rd</sup> to 48<sup>th</sup> (186.63 mAh/g) cycles it is only about 81.8%. The exceptional capacity retention in LR1 is better than similarly structured Li-rich materials prepared through different routes and reported previously [108–110].

The rate capabilities of both materials have been studied in the potential range of 2.0–4.8 V as shown in Figure 3.4b. The results indicate that both materials have the same tendency of discharge behavior up to 10 cycles at 0.1C with a discharge gap between LR1 and LR2 of 12 mAh/g (209.25 mAh/g of LR1 and 221.274 mAh/g of LR2) at the end of the first 10 cycles. As the discharge rate increases to 0.2C in the following second 10 cycles, the gap decreased to about 5 mAh/g (193.06 mAh/g of LR1 and 198.38 mAh/g of LR2). At the end of 3rd, 4th and 5th tens cycle the gaps continue to decrease: to –17mAh/g (155.99 mAh/g LR1, 139.14 mAh/g LR2), to –22 mAh/g (132.13 mAh/g LR1, 109.44 mAh/g LR2), and to –34 mAh/g (89.02 mAh/g LR1, 54.74 mAh/g LR2) at 1C, 2C and 5C, respectively.

The discharge capacities of LR1 and LR2 at 1C were further studied up to 100 cycles as displayed in Figure 3.4c. LR1 shows interesting specific discharge stability started from 127 mAh/g in the initial discharge capacity and ended up to 149 mAh/g in the 100<sup>th</sup> cycle. In contrast, LR2 delivers 139 mAh/g and 128 mAh/g in the 1<sup>st</sup> and 100<sup>th</sup> cycles, respectively. The less Co content can suppress the total phase transformation in the first cycle and give a clear interpretation for these Li-rich cathode materials from two aspects. On the one hand, the Co<sup>3+/4+</sup> eg band is partly overlapped with the top of the O<sup>2-</sup> 2p band [105–107], which makes the covalent bond in metal oxide stronger and easier for oxidation of O<sup>2-</sup> to O<sub>2</sub> in the layered lattice, and thus enhances the phase transformation of the Li-rich layered phase. On the other hand, based on the calculations previously reported [111], when most of the Li ions are deintercalated in the high potential region during charge process, the transition metal ions would diffuse into the Li layer, leading to the formation of a spinel-like phase. Consequently, the less amount of Co in the Li-rich cathode materials can play an important role in suppressing the total phase transformation in the first cycle and display wider reacted regions in LR1 than in

LR2 over subsequent cycling. Importantly, LR1 also shows a noticeably higher discharge capacity retention (98% at 100<sup>th</sup> cycle) than most other Li-rich cathode materials in the literature. For instance, an 88.3% capacity retention at 1C and 100<sup>th</sup> cycle was reported in one study [112], and a 70.3% capacity retention was reported at 0.5C and 80<sup>th</sup> cycle in another [109].

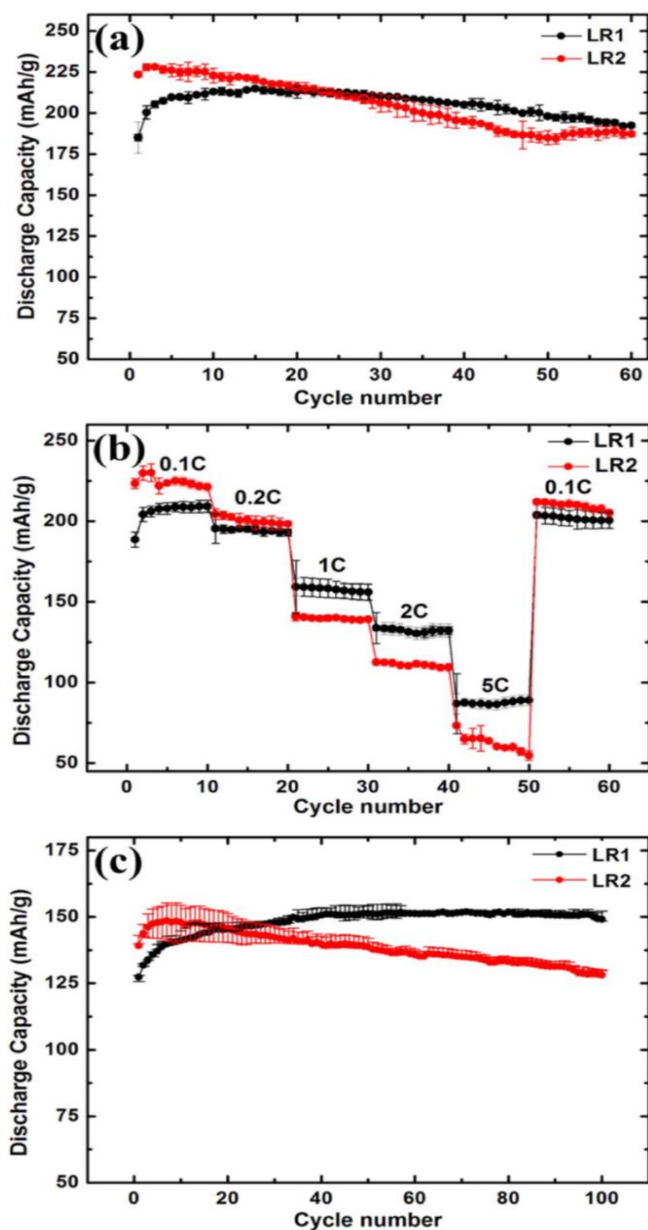


Figure 3. 4 (a) Cyclic performance at 0.1C, (b) rate capability at various C rates, and (c) cyclic performance at 1C.

To further characterize the electrochemical properties of LR1 and LR2, cyclic voltammetry was performed on the cathode materials. The current vs. voltage plots corresponding to the 1<sup>st</sup>, 2<sup>nd</sup>, 5<sup>th</sup> and 10<sup>th</sup> cycles at a scan rate of 0.1 mV/s from 2.0 to 4.8 V are displayed in Figure 3.5. The first cycle of both materials from 3.6 V to 4.8 V displayed the same electrochemical behavior since both have the same amount of Li<sub>2</sub>MnO<sub>3</sub>.

There are two anodic peaks in the first charge process for both materials. The first peak appears at ~4.10 V and is attributed to the oxidation of Ni<sup>2+/4+</sup> and Co<sup>3+/4+</sup> in the layered phase [103]. The second peak appearing at ~4.67 V is due to the activation of Li<sub>2</sub>MnO<sub>3</sub> [113,114], which is consistent with what is observed in Figure 3.3.

The corresponding cathodic peaks of Ni<sup>4+/2+</sup> and Co<sup>4+/3+</sup> are observed at ~4.25 V and ~3.75 V, respectively. The discharge regions below 3.6 V, which correspond to the reduction of Mn<sup>4+/3+</sup>, show different plateau regions. LR2 exhibited a longer plateau region than LR1, indicative of that LR2 delivers a higher initial discharge capacity that attributed to the higher surface area of LR2. For the subsequent cycles, LR2 shows a significant disappearance of the anodic peak at ~4.67 V, but LR1 still shows this anodic peak of activation in progression from the 2<sup>nd</sup> to the 10<sup>th</sup> cycle, but shifted to a lower potential ~4.30 V. This is in agreement with what was observed in battery charge cycling in Figure 3.3a, which is that there is no total activation of the Li<sub>2</sub>MnO<sub>3</sub> phase in the first charge cycle, but a slow activation in further cycling.

During the charging process, the CV curves of both materials at ~4.0 V become wider and shift to a lower voltage (~3.75 V), indicative of that the electrode surface area and/or the bulk structure of the synthesized materials may have been changed after the first cycle. The most significant change in this process is that the electrochemical activity of both materials near 3.25 V during charge and discharge processes gradually

develops and shifts to a lower voltage range near 3.0 V following the 10<sup>th</sup> cycle. In addition, the reduction peaks in the discharge curves below 3.5 V can be ascribed to the Li<sup>+</sup> deintercalation process [115,116]. However, LR1 shows more pronounced redox peaks comparing with LR2 cathode material, indicative of that LR1 delivers higher charge/ discharge capacity over cycling. The voltage gaps between the anodic and cathodic peaks of LR1 are smaller than those of LR2, implying that the reversibility is better in LR1 than in LR2.

This corroborates with what was ascribed earlier in this work that less Co/Mn mole ratio could play an important role in hindering the total activation in the first cycle and enhance the backward capacity over cycling.

The difference in interfacial electrochemistry for LR1 and LR2 materials has been studied by EIS in the frequency range from 0.05 Hz to 1MHz (see Figure 3.6). The high-frequency semicircles ascribed represent the electron electrolyte interface (SEI) resistance (RSEI) before 1st cycle, after the 10<sup>th</sup> cycle, and after the 100<sup>th</sup> cycle, respectively. The results are further summarized in Table 3.4. LR2 material with smaller particle size exhibits smaller RSEI1 of 646.78  $\Omega$  than that of LR1 at 806.5  $\Omega$ , consistent with the higher initial discharge capacity of LR2 as seen in Figure 3.2 attributed to its higher surface area [109]. However, further measurements showed different behaviors; LR2 shows higher values of 93.32  $\Omega$  and 209.59  $\Omega$  than those 52.90  $\Omega$  and 123.79  $\Omega$  of LR1 after the 10<sup>th</sup> and 100<sup>th</sup> cycles (RSEI2 and RSEI3), respectively. From these results, it is evident that the small particle size and high surface area of LR2 lead to an increase in the SEI layer formation over cycling due to increased side reactions with the electrolyte. This result is in agreement with the result in Figure 3.4, which suggests that LR1 has higher stability at various discharge rates.

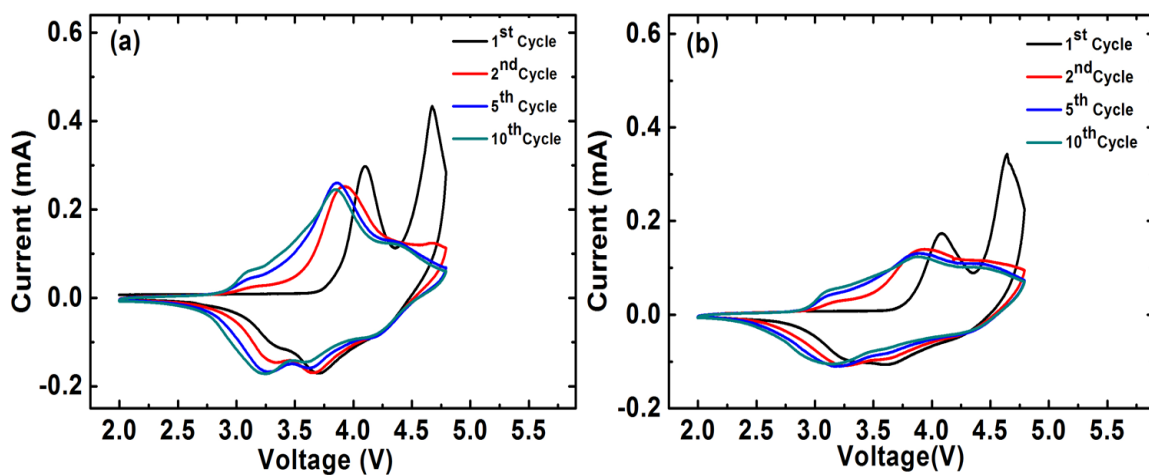


Figure 3. 5 Cyclic voltammograms between 2.0–4.8 V at a scan rate 0.1 mV/s, (a) LR1 and, (b) LR2.

Table 3. 4.  $R_{SEI}$  values of LR1 and LR2 materials at different cycles.

Component	$R_{SEI1}(\Omega)$	$R_{SEI2}(\Omega)$	$R_{SEI3}(\Omega)$
	before 1 <sup>st</sup> cycle	after 10 <sup>th</sup> cycle	after 100 <sup>th</sup> cycle
LR1	806.50	52.90	123.79
LR2	646.78	93.32	209.59



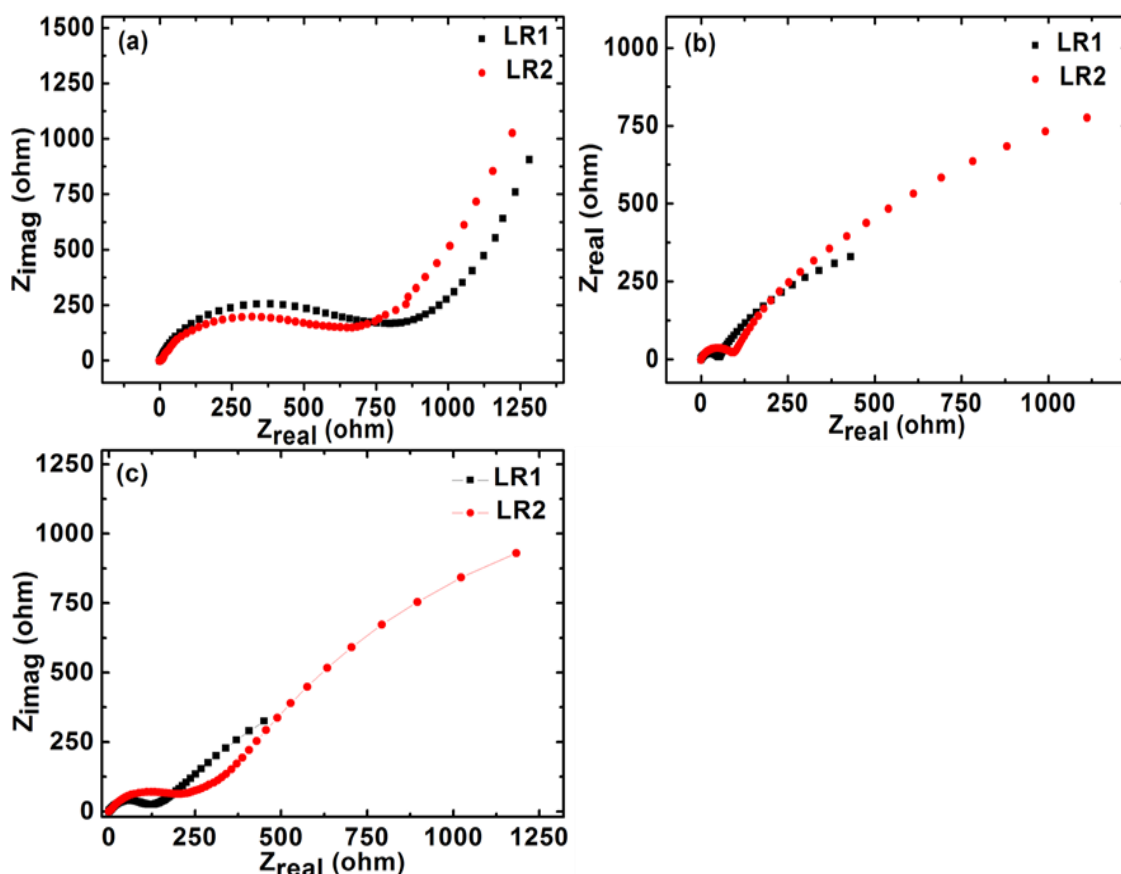


Figure 3. 6 Nyquist plots of EIS spectra of LR1 and LR2 materials at different cycles; (a) before the first cycle, (b) after the 10<sup>th</sup> cycle and, (c) after the 100<sup>th</sup> cycle.

### 3.5. Conclusions

Two lithium-rich cathode materials  $\text{Li}_{1.2}\text{Mn}_{0.51}\text{Ni}_{0.145+x}\text{Co}_{0.145-x}\text{O}_2$  ( $x = 0$  or  $0.0725$ ) were successfully prepared with a newly developed sol gel technique using glycerol as a solvent and reagent. Both materials have typical Li-rich material phases with good crystallinity, but the particle size and morphology are different. LR1 sample has less Co and produced larger particles of  $0.35\text{--}0.88\ \mu\text{m}$ , as compared to LR2 of  $0.18\text{--}0.36\ \mu\text{m}$ . LR1 showed an increasingly improved discharge capacity at a  $0.1\text{C}$  rate up to 15<sup>th</sup> cycle, followed by 93.5% capacity retention up to 48<sup>th</sup> cycle. In addition, at  $1\text{C}$  discharge rate LR1 capacity increased steadily from  $127\ \text{mAh/g}$  (1<sup>st</sup> discharge cycle) to  $152\ \text{mAh/g}$  (80<sup>th</sup> discharge cycle) and ended at  $149\ \text{mAh/g}$  (98% capacity retention) in

the 100<sup>th</sup> cycle. The superior performance in LR1 was attributed to the continuous activation of the  $\text{Li}_2\text{MnO}_3$ . Rapid capacity fading in LR2 was attributed to small particle size and high surface area leading to deterioration of the electrode/electrolyte interface. Overall, the obtained results suggest that LR1 could be a performing Li-rich material for Li-ion battery that requires both cycling stability and high rate capability.

### 3.6 Acknowledgements

The authors would like to thank Dr. Eric Bohannon for help with obtaining XRD results, Dr. Honglan Shi with ICP-MS analysis, Prof. Muthanna Al-Dahhan, Dr. Hyder Al-Nasri and Dr. Ali Rownaghi for BET analysis, and Dr. Jin-Yun Liao with SEM imaging. This material is based upon work partially supported by the Department of Energy, Office of Energy Efficiency and Renewable Energy (EERE), under Award Number DE-EE0007282. They also acknowledge partial financial support from the University of Missouri. K.I.H thank the Higher Committee for Education Development in Iraq (HCED) for providing a scholarship.

## **Chapter 4. Manganese-Based Li-rich Cathode Materials Prepared Using Precursor Salts with Acetate and Nitrate Anions**

### **4.1 Abstract**

Lithium-rich layered oxide cathode materials of  $\text{Li}_{1.2}\text{Mn}_{0.5100}\text{Ni}_{0.2175}\text{Co}_{0.0725}\text{O}_2$  have been synthesized using salts with different anions as metal precursors and glycerol as a solvent. The effects of the precursor metal salts on particle size, morphology, cationic ordering, and ultimately, the electrode performance of the cathode powders have been studied. As verified by FTIR analysis, the use of cornstarch as a gelling agent along with nitrate-based metal salt results in a reduction of particle size, leading to higher surface area and initial discharge capacity. However, this material suffers from rapid capacity fade over cycling, in contrast to the material made with acetate salt. The latter forms acetyl groups during synthesis, effectively preventing cornstarch from capping the particles, thus leading to larger particles. When nitrate and acetate salts are mixed in the synthesis of cathode powders, the new cathode powders demonstrate good initial discharge capacity, promising a potential Li-rich cathode material for lithium-ion batteries.

### **4.2 Introduction**

Lithium-ion batteries (LIBs) have drawn the attention of many researchers in the recent years due to their long cycle life and high energy density [117,118], making them a major power source for portable electronic devices [119]. Additionally, global warming and depletion of fossil fuels pave the way for use of low-emission electric vehicles (EVs) or hybrid electric vehicles (HEVs). LIBs have been selected as the most

important candidate for HEVs and EVs [120–122]. However, the inadequate specific capacity of most traditional cathode materials (e.g.,  $\text{LiCoO}_2$  (~150 mAh/g) [7]) cannot provide the desired energy for EVs with long drive ranges. Extensive studies have been dedicated to developing new cathode materials that have higher specific capacity, better discharge rate capability, lower cost and are environmentally friendly.

Due to their high specific capacity (>200 mAh/g), high working voltages (4.6~4.8V) and adequate safety, Li-rich oxides of  $x\text{Li}_2\text{MnO}_3 \cdot (1-x)\text{LiMO}_2$  ( $0 < x < 1$ , M = Mn, Co, Ni, Fe, etc.) formula have been widely used [73,79,123]. However, several disadvantages diminish their potential for practical applications. For example, large irreversible capacity loss was observed in the first cycle [76,79,124]. Rate capability is not satisfactory [79,125,126], and fast capacity fade occurs during cycling [77,124,127]. The largely irreversible capacity loss in the first cycle has been mainly ascribed to the activation reaction of  $\text{Li}_2\text{MnO}_3$  during the first charging process above 4.5V, resulting in a release of  $\text{Li}^+$  and oxygen in the form of  $\text{Li}_2\text{O}$ . Consequently, oxygen-ion and lithium-ion vacancies are generated and partially occupied by transition metal ions (e.g., Ni ions) [73,74]. This leads to blocking of  $\text{Li}^+$  insertion sites in the active material and thus the large capacity loss during the discharge process [128]. In subsequent cycles, the material structure continues to degrade, which results in continuous capacity deterioration. Fortunately, attempts have been effectively made to improve the performance and structural stability of Li-rich cathode materials, such as surface modification [129,130] and structure and morphology controlling [131,132].

It is noteworthy that the synthesis method has a definite influence on particle size, cationic ordering, and the electrochemical performance of the synthesized electrode materials [28,30,44]. The sol-gel synthesis approach has been adopted because it

ensures uniform distribution and atomic-level mixing of the reactants when used with a gelling agent. It is believed that using cornstarch as a gelling agent can play a dual role in particle formation. Cornstarch is a polysaccharide of glucose and consists of two kinds of polymeric chains: amylopectin and amylose. The amylopectin kind (branched) acts as a gelling agent with acetate based materials. The amylose kind (linear) reacts predominately with the nitrate-based materials and liberates  $\text{NO}_x$  and  $\text{CO}_x$  gases, leading to a fluffy mass with a porous structure [66]. Additionally, it was found that using glycerol as a solvent to replace water resulted in production of a well-ordered layered structure of  $\text{LiMn}_{1/3}\text{Ni}_{1/3}\text{Co}_{1/3}\text{O}_2$  cathode material that requires less time and energy [90].

Taking into account the relatively toxic and expensive Co content in previously studied Li-rich cathode materials, we recently studied a new Li-rich cathode material with a much lower Co/Mn mole ratio (1:7.134) than the reported one of 1:6 [82]. Besides decreasing the toxicity of Li-rich cathode materials, the increase in Ni content from 0.1450 to 0.2175 (in moles) and a decrease in Co content from 0.1450 to 0.0725 led to an increase in particle size from 0.36 to 0.88  $\mu\text{m}$ . This enlargement was found to be beneficial in increasing the discharge capacity from 185 to 213 mAh/g after 20 cycles [133]. The increase of the discharge capacity upon cycling has been reported by other researchers. For example, a recent paper by Sung *et al.* reported that the continuous activation of the remaining  $\text{Li}_2\text{MnO}_3$  is the reason for the increase in the specific capacity of their materials in the first 20 cycles from 187 to 194 mAh/g [89]. Another study by Kang *et al.* proposed that the large particle size is the reason for a gradual increase in the specific capacity of Ni-doped cathode materials in the first 40 cycles [134].

In this paper, we report a detailed study on the role of cornstarch as a gelling agent and glycerol as a solvent in the synthesis of Li-rich cathode materials. The study is focused on making the Li-rich cathode material,  $\text{Li}_{1.2}\text{Mn}_{0.5100}\text{Ni}_{0.2175}\text{Co}_{0.0725}\text{O}_2$ , using pure acetate salt (sample abbreviated as LRAC), pure nitrate salt (LRNI), and identical amounts (in mole) of acetate and nitrate salts (LRACNI). The effects of gelling in different metal salts on particle size, particle morphology, structure orders, and electrochemical performance have been studied further.

### 4.3 Experimental section

$\text{Li}_{1.2}\text{Mn}_{0.5100}\text{Ni}_{0.2175}\text{Co}_{0.0725}\text{O}_2$  cathode materials were synthesized by the sol-gel method using glycerol as a solvent and cornstarch as a gelling agent. For the acetate-based LRAC, stoichiometric amounts of lithium acetate dihydrate, nickel acetate tetrahydrate, cobalt acetate tetrahydrate, and manganese acetate tetrahydrate were used as raw materials. For the nitrate-based LRNI, stoichiometric amounts of lithium nitrate trihydrate, nickel nitrate hexahydrate, cobalt nitrate hexahydrate, and manganese nitrate tetrahydrate were used as raw materials. The LRACNI cathode material was made of 0.5 moles of acetate-based salts and the same amount of nitrate-based salts. A 10% excess of lithium was added to compensate for lithium loss during the high-temperature calcination process. The raw materials were dissolved in glycerol at about 100°C with stirring to form a deep eutectic solvent phase [90]. An appropriate amount of cornstarch (molar ratio of cornstarch:  $\text{M}^+ = 1.0:4.0$ ) was added to the clear solution at 80°C with a high-speed mixing. After 4 hours of continuous heating and stirring, a gel forms, and the viscosity of the precursor suddenly increases to the point that the material cannot be stirred further.

Three different heat treatments were carried out to obtain the final crystalline particles. The first stage was done at 250°C for 3 hours, right after the gel formed, to obtain a relatively dry powder. In the second stage, the dry powder was pelletized and heated to 400 °C with a 5 °C/min heating rate for 8 hours to get rid of organic components fully. In the third stage, it was heated to 900 °C for 12 hours. Afterward, the synthesized powder was cooled down to room temperature naturally. It was ground for further characterizations.

The electrodes were prepared by mixing 80 wt% active materials, 10 wt% carbon black, and 10 wt% polyvinylidene fluoride (PVDF). An appropriate amount of N-methyl-2-pyrrolidinone (NMP) was added to the mixture and mixed thoroughly until a uniform black slurry was obtained. The slurry was cast on an Al foil current collector and dried at 80 °C for 2 hours, followed by drying in a vacuum furnace at 120 °C for 12 hours. A 7/16 inch prepared electrode was punched out, pressed between two aluminum discs at 10 kN, and used to assemble a battery in the glovebox (MBRAUN). The assembled battery was composed of the prepared electrode (cathode), Li foil (anode), a porous polypropylene separator (Celgard), and 1.0 M LiPF<sub>6</sub> in dimethyl carbonate (DMC) - ethylene carbonate (EC) (DMC:EC = 1:1, v/v) electrolyte.

Fourier Transform Infrared Spectroscopy (FTIR) was carried out using a Nicolet 380 spectrometer (Thermo Scientific). The spectrum of each sample has an average result of 64 interferogram scans with a resolution of 2 cm<sup>-1</sup> with the scan range of 400-4000 cm<sup>-1</sup>. Thermal analysis of acetate, nitrate, and acetate-nitrate based materials with cornstarch was conducted by thermogravimetric analysis (TGA) using a thermobalance model TGA Q500 (TA USA) in the temperature range of 30-950 °C with a heating rate of 10 °C/min. Mole ratios of Li, Mn, Ni, and Co were analyzed by using a

bNexION 350D ICP-MS (PerkinElmer) instrument. Surface morphology and particle distribution of the synthesized cathode materials were investigated using FEI Quanta 600 FEG Environmental Scanning Electron Microscope (ESEM). The phase characterization and cationic ordering was studied by X-ray diffraction (XRD) (PANalytical X'Pert Multi-Purpose Diffractometer) with the scanning rate of  $0.02^\circ/\text{s}$  and  $2\theta$  value ranging from  $10^\circ$  to  $90^\circ$ . The charge-discharge study at different current rates for all the electrodes was carried out using an Arbin cyler (Model BT-2043) at room temperature between 2.0 and 4.8 V. Gamry Reference 3000 was used to further investigate the electrochemical characteristics. Cyclic voltammetry (CV) between 2.0 and 4.8 V at a scan rate of 0.1 mV/s and electrochemical impedance spectroscopy (EIS) from 0.05 Hz to 1 MHz were performed.

#### 4.4 Results and discussion

FTIR analysis was used to analyze both the gel and the subsequent dry powder, as shown in Figure 4.1 a and b, respectively. In the acetate sample LRAC, an ester acetyl peak near  $1750\text{ cm}^{-1}$  (C=O) and an acetate peak closer to  $1600\text{ cm}^{-1}$  can be seen (see Figure 4.1(a)). The presence of the ester peak indicates that the -OH groups on cornstarch have, at least partially, been replaced with acetyl groups [135], as illustrated in Figure 4.2. This would change its ability to cap any particles formed. None of those peaks are present for the nitrate sample LRNI. The sample that has a mixture of acetate and nitrate (LRACNI) similarly shows a small ester acetyl peak near  $1750\text{ cm}^{-1}$ . Together, the FTIR results show that the capping agent is different between the acetate and nitrate samples. This provides evidence as to why there are different sizes of particles made with acetate and nitrate salts. Additionally, we can look for C-N peaks



in the LRNI sample (around  $1100\text{ cm}^{-1}$ ). Ideally, they should not be there, as the peaks for the cornstarch overlay directly on the nitrate sample. The results show that the cornstarch in the nitrate sample is unchanged and acting as a capping agent on its own.

For dry powder Figure 4.1(b), we can also see there is an -OH peak in the acetate sample. If all of the -OH groups have been removed, the peak (near  $3300\text{ cm}^{-1}$ ) should be small. This indicates that not only the surfactant properties are changing with acetylation, but the formed gel is likely different enough to change how the particles aggregate (H-bonding, in particular, disappears).

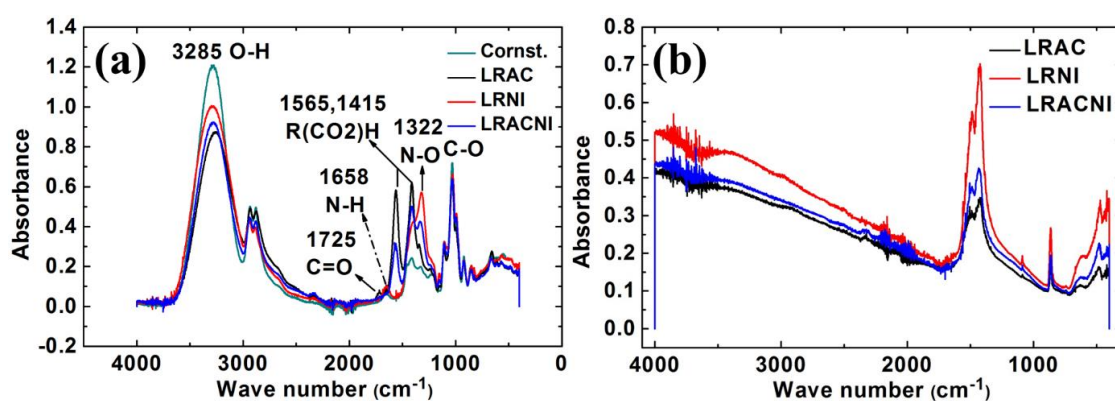


Figure 4. 1 FTIR of (a) gel, and (b) dry powder.

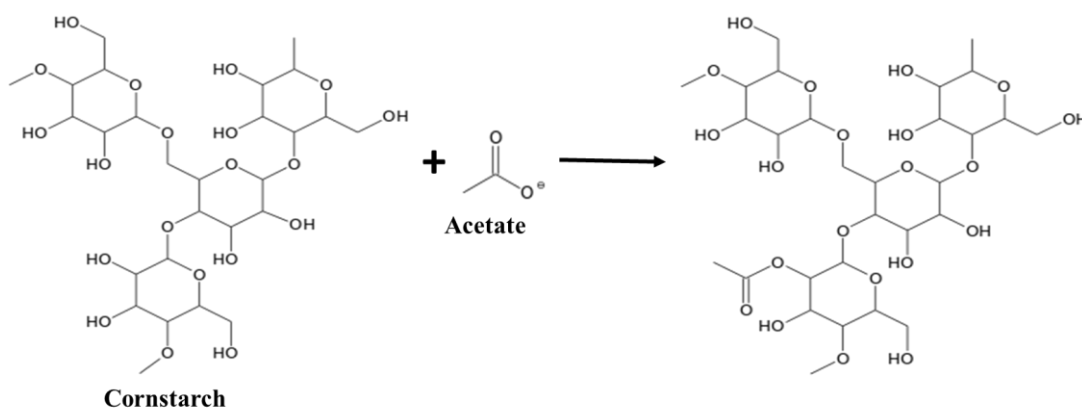


Figure 4. 2 Acetylation mechanism of cornstarch with metal acetates.

#### 4.4.1 Thermal analysis - TGA.

Figure 4.3 shows the thermal analysis results of the dry powders of LRAC, LRNI, and LRACNI. It is interesting that all three figures show a similar thermal behavior up to 250 °C. The 25–120 °C region corresponds to the weight loss of physically absorbed water; there is no weight loss in the region between 125-250°C. The reason would correspond to decomposition of the acetate precursor with cornstarch, indicating their absence as they already were decomposed. However, the LRAC sample shows quite different thermal behavior from the other two samples as depicted in Figure 4.3(a). The formation and dissolution of the metastable chelating complex are more likely to happen at 363 °C and 440 °C, respectively, while with water solvent, the formation occurred at 380 °C and 450 °C, respectively [66]. In addition, the desired product of  $\text{Li}_{1.2}\text{Mn}_{0.5100}\text{Ni}_{0.2175}\text{Co}_{0.0725}\text{O}_2$  formed at 466 °C as indicated in Figure 4.1(a). LRNI and LRACNI show three distinct weight loss regions during heat treatment as follows: liberation of  $\text{NO}_x$  and  $\text{CO}_x$  gases between 250-329 °C, completion of the cornstarch-nitrate combustion process in the reaction region between 329-425 °C, and the final product formation between 425-490 °C, in particular, at 466 °C as illustrated in Figure 4.3.

One notable result from the thermal analysis of the three materials is that the weight loss of LRACNI is higher than LRNI and lower than LRAC, which reveals the strongest bond (N-O) of LRNI and weakest bond of LRAC (acetate bond). The higher released energy from the breaking of the N-O bond in LRNI results in evaporation of more organic components, which leads to a reduction in the weight loss in the subsequent heat treatment processes. Furthermore, the cornstarch-nitrate combination confirms what was explained earlier in Figure 4.2, that cornstarch is a capping agent of nitrate-

based particles and prevents the formation of large particles. In addition, cornstarch could perform a dual role in the synthesis, both as a gelling agent and as an exothermic combustible fuel. It was noted in this present study that the use of cornstarch for the preparation of lithium rich cathode materials has exhibited the same thermal behavior as in a previous report on the preparation of  $\text{Li}_2\text{MnO}_4$  and  $\text{LiCoO}_2$  using cornstarch as a combustion-assisting component [136].

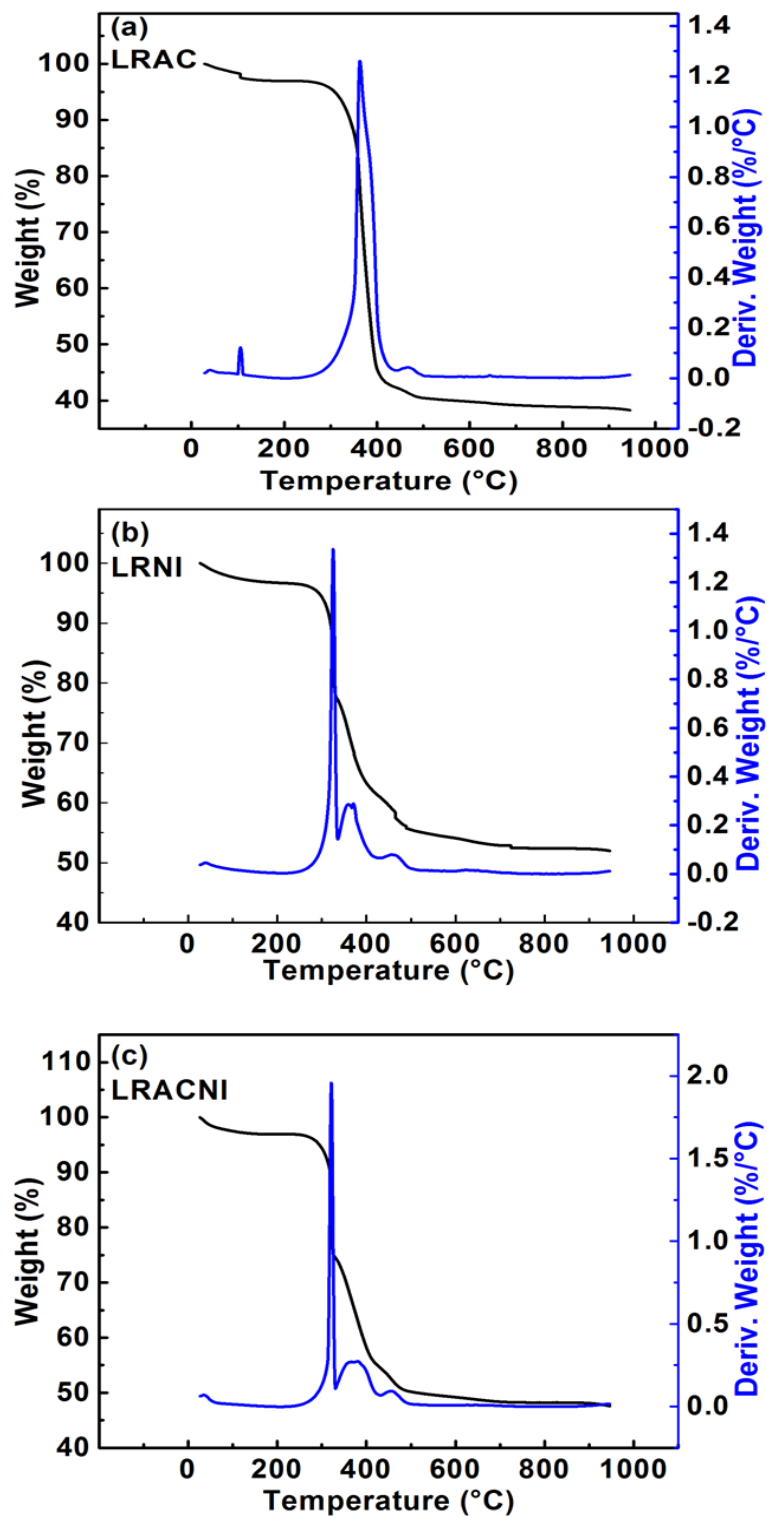


Figure 4. 3 Thermal analysis of cornstarch with; (a) LRAC, (b) LRNI, and (C)LRACNI.

An ICP-MS analyzer was used to confirm the concentrations of the forming LRAC, LRNI, and LRACNI materials. Table 4.1 shows the concentration of each element in the mole ratio. The results demonstrate good agreement between the nominal values for elements Mn, Ni, and Co. On the other hand, LRNI exhibits a higher lithium loss of ~8.6 % than LRAC at ~1.8% and LRACNI at ~3%. This is mainly attributed to the higher agglomeration of acetate-based salt powder that could hinder Li loss by decreasing the surface area. On the contrary, the nitrate-based salt will release NO<sub>x</sub> and CO<sub>x</sub> gases resulting in more likely fluffy structure [66] and increased outer surface area, which results in increased Li loss during different preparation steps.

Table 4. 1 ICP-MS data for LRAC and LRAC and LRNI cathode materials

Element	Nominal values	Experimental values		
		LRAC	LRNI	LRACNI
Li	1.2	1.1782	1.0970	1.1637
Mn	0.5100	0.5201	0.5073	0.5212
Ni	0.2175	0.2069	0.2203	0.2063
Co	0.0725	0.0730	0.0724	0.0725

#### 4.4.2 Materials Morphology

As can be seen from the SEM images in Figure 4.4(a), LRAC has a particle size ~ 0.8 μm with rectangular prismatic nanorod and hexagonal nanorod particles. It is well known that branched-type cornstarch forms gels with acetate, but the linear form usually reacts with the nitrate to release CO<sub>x</sub> and NO<sub>x</sub>, forming a fluffy mass [66]. The fluffy mass in LRNI possesses a reduced particle size of ~ 0.4 μm with spherical grains as shown in Figure 4.4(b). It is also evident from the SEM images that the presence of

nitrate and acetate (LRACNI) produces an intermediate particle size of  $\sim 0.6 \mu\text{m}$  (Figure 4.4(c)).

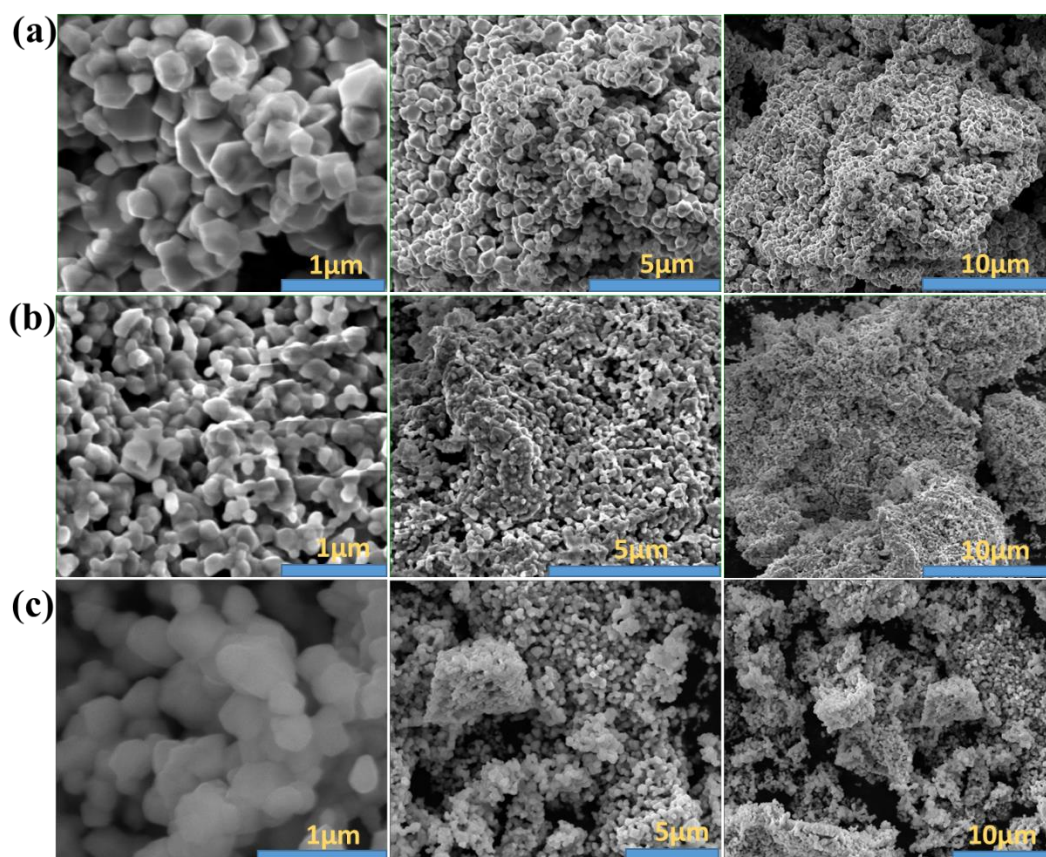


Figure 4. 4 Typical SEM images of (a) LRAC, (b) LRNI, and (c) LRACNI, at different magnifications.

#### 4.4.3 Phase analysis-XRD

Figures 4.5 (a) and (b) show the XRD patterns and local details of LRAC, LRNI, and LRACNI compounds. As shown in Figure 4.1 (a), all the prepared samples possess a typical rhombohedral symmetry in space group  $R\bar{3}m$  for layered phase  $\text{LiMO}_2$ , and monoclinic symmetry in space group  $C2/m$  for not impurity phase of  $\text{Li}_2\text{MnO}_3$  [103,137,138]. Additionally, the almost-identical structures of all the prepared samples indicate that the initial root material has no apparent effect on the crystal structure. All

the diffraction peaks can be indexed to the layer structure of  $\alpha$ -NaFeO<sub>2</sub> type, except for the weak diffraction peaks between 20° and 25°, which are indexed to the effect of superlattice monoclinic structure (C2/m) of Li<sub>2</sub>MnO<sub>3</sub> [139]. The apparent splits of (006)/(012) and (108)/(110) peaks for all the prepared samples demonstrate excellent crystallinity and well-defined layered structures for the synthesized materials [140,141]. From Figure 4.1(b), the (003) peak first shifts to a higher angle using a pure nitrate content (LRNI), and then moves to a lower angle with pure acetate raw material (LRAC), which manifests the shrinking and expansion in lattice dimensions and confirms further what has been explained earlier in Figure 4.1.

Lattice parameters of the samples were calculated using XRD data, and the results are listed in Table 4.2. The results show a slight increase in the lattice parameters  $a$  and  $c$  in nitrate-based materials, indicative of some lithium-ion electronegative vacancies generated to balance the loss of Li<sup>+</sup> during preparation steps. As shown in ICP-MS results in Table 4.1, the lithium loss increases with increasing nitrate content, and LRNI has the most lithium-ion electronegative vacancies and LRAC has the least. Accordingly, the lattice parameters increase with increasing nitrate contents. From Table 2,  $c/a > 4.9$  and  $I(003)/I(104) > 1.2$ , suggesting that a well-ordered hexagonal structure with good crystallinity and no undesirable cation mixing is present in all of the samples [96]. Compared with LRAC and LRNI, LRACNI shows the highest  $I(003)/I(104)$  value of 1.9351, suggesting that LRACNI has better cationic ordering.

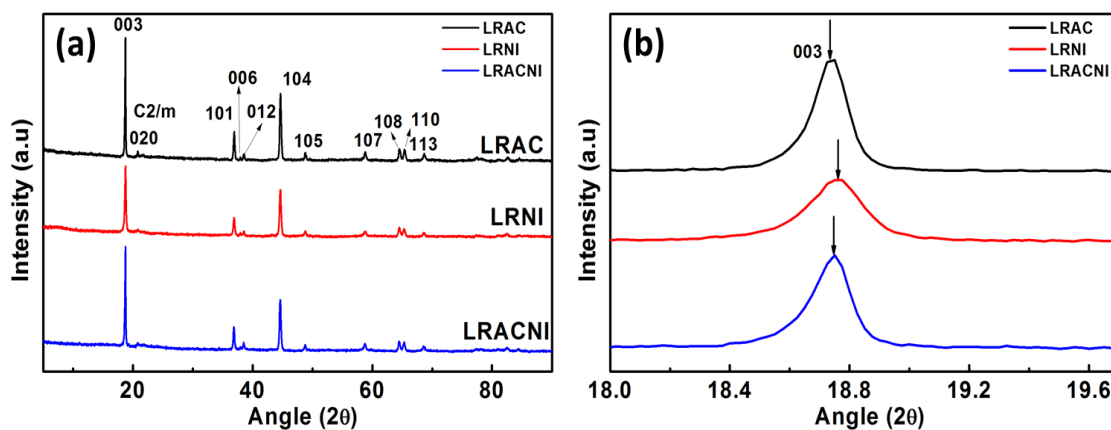


Figure 4. 5 XRD patterns of LRAC, LRNI, and LRACNI in the  $2\theta$  range of (a) 5-90° and (b) 18-19.7°.

Table 4. 2 Lattice parameters of LRAC, LRNI and LRACNI samples.

Component	$a$ (Å)	$c$ (Å)	$c/a$	I (003)/I (104)
LRAC	2.8552	14.2299	4.984	1.7736
LRNI	2.8604	14.2419	4.979	1.4446
LRACNI	2.8588	14.2399	4.981	1.9351

#### 4.4.4 Electrochemical characterizations

The 1<sup>st</sup>, 2<sup>nd</sup>, 10<sup>th</sup>, and 30<sup>th</sup> charge/discharge tests for the LRAC, LRNI, and LRACNI materials were carried out in the potential range of 2.0-4.8V at 0.1C (1C=200 mA/g) as displayed in Figure 4.6. The 1<sup>st</sup> charge cycle shows two plateau regions. The first plateau results from the oxidation of Ni<sup>2+</sup>/Ni<sup>4+</sup> and Co<sup>3+</sup>/Co<sup>4+</sup> [119,120]. Because of the higher surface area in LRNI (the reaction occurs on the surface), the plateau in LRNI is much longer than that in LRAC and LRACNI, meaning that LRNI provides higher specific capacity. The second plateau region above ~4.5V is related to the activation of Li<sub>2</sub>MnO<sub>3</sub>[121,122]. LRNI shows higher activation of Li<sub>2</sub>MnO<sub>3</sub>, which is attributed to more reactive sites associated with the higher surface area of this sample, resulting in



higher transformation of the layered phase to the spinel phase. However, for LRACNI and LRAC, the oxidation reaction region of  $\text{Li}_2\text{MnO}_3$  decreases, indicating of that the larger particle size could minimize full phase transformation in the first cycle. Consequently, LRNI provides the highest initial charge/discharge capacity of 374.00/256.85 mAh/g, compared to 275.86/185.09 mAh/g and 338.52/248.32 mAh/g of LRAC and LRACNI, respectively. For the subsequent cycles, the plateau above ~4.5V disappeared entirely. This is attributed to irreversible Li loss in the first charge cycle accompanied by oxygen from lithium and transition metal layers in the form of  $\text{Li}_2\text{O}$  [73,142].

The voltage fade of LRAC in the first discharge cycle is much greater than that of LRNI or LRACNI. However, for the 5<sup>th</sup>, 10<sup>th</sup>, and 30<sup>th</sup> cycles, this voltage fade decreases gradually, until it becomes overlapped with LRNI and slightly less than LRACNI. This noticeable voltage fade behavior could be attributed to the incomplete extraction of  $\text{Li}^+$  from the LRAC sample in the first discharge cycle, resulting in a low  $\text{Li}_2\text{MnO}_3$  reaction region associated with high discharge voltage fade. The larger particle size can deter phase change, which in turn increases the charge/discharge specific capacity and working voltage over cycling [134]. Synthesizing intermediate sized particles as in LRACNI delivers a high initial discharge capacity relative to LRAC and LRNI samples illustrated in Figure 4.6.

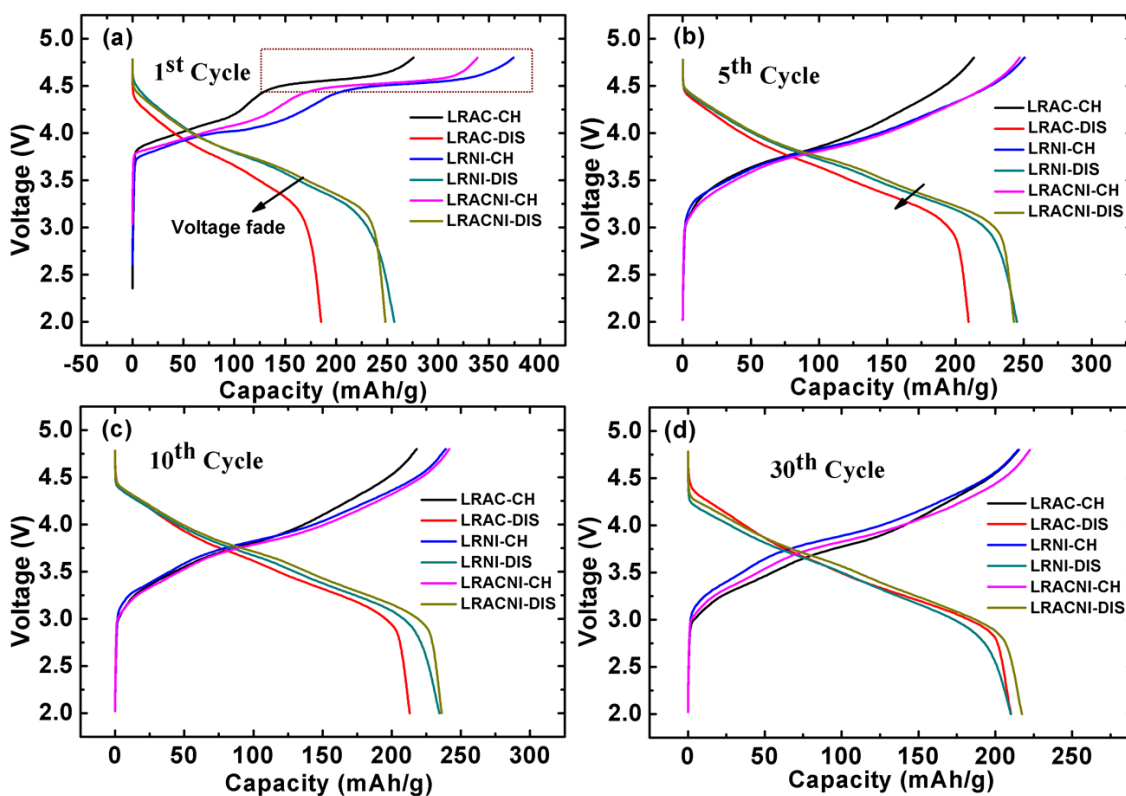


Figure 4. 6(a) 1<sup>st</sup>, (b) 5<sup>th</sup>, (c) 10<sup>th</sup>, and (d) 30<sup>th</sup>; charge/discharge curves for LRAC, LRNI and LRACNI cathode materials.

The electrochemical performances of the materials were further studied by cycling the cells at a current rate of 0.1C as shown in Figure 4.7 (a). The coulombic efficiencies were calculated as shown in Figure 4.7 (b). The results display different performance categories, which are mostly influenced by the particle size. The 1<sup>st</sup>/30<sup>th</sup> discharge capacities of LRAC, LRNI, and LRACNI were 185.09/210.25, 256.85/210.09 and 248.32/217.28 mAh/g, respectively. LRACNI shows the highest coulombic efficiency in the first cycle of 73.35%, as compared to 67.1 and 68.7% for LRAC and LRNI, respectively. The higher reversible capacity of the LRACNI sample is mainly attributed to the lower cationic mixing of Ni<sup>+2</sup> and Li<sup>+</sup>, which can effect Li<sup>+</sup> diffusion during the intercalation/deintercalation processes. This can be argued by the highest I(003)/I(104) value among the three samples [143]. After the 1<sup>st</sup> cycle, the coulombic efficiencies of the three tested samples show an almost symmetrical trend.

The cells were discharged at 1C (200 mA/g) with a 2.0-4.8V voltage range for 200 cycles, as displayed in Figure 4.7(c). The 1<sup>st</sup>/200<sup>th</sup> discharge cycles were 127.32/87.15 (68.45% capacity retention), 199.14/121.04 (60.78%) and 187.41/144.93 (77.33%), for LRAC, LRNI and LRACNI, respectively. Figure 4.7(d) shows the rate performance of samples when they were discharged between 2.0-4.8 V. Due to electrode polarization at high rates, the discharge capacities of the tested electrodes fade with increasing discharge current rates [144]. However, LRAC and LRACNI electrodes exhibit remarkably improved rate capabilities when compared to the LRNI electrode. Of the three tested electrodes, LRACNI exhibits the optimal rate performance up to 1C, giving discharge capacities of 248.32, 235.63, and 184.33 mAh/g at 0.1, 0.2, and 1C, respectively. This is clearly better than the LRAC sample (196.60, 195.48, 159.29 mAh/g at 0.1, 0.2, and 1C, respectively). This outstanding rate performance of the LRACNI electrode is mainly ascribed to the enlargement of Li<sup>+</sup> diffusion channels. This is caused by the low cationic mixing of Ni<sup>2+</sup> and Li<sup>+</sup>, which is favorable during insertion/extraction of Li<sup>+</sup> [96]. However, at 2C and 5C, LRAC shows a much better rate performance than LRACNI. The deterioration in rate capability of LRACNI at higher C rates can be mainly attributed to a thicker SEI layer that is associated with smaller particle size [58].

To confirm the cycling performance of the synthesized materials, cyclic voltammetry (CV) was carried out within a potential range of 2.0-4.8 V at 0.1 mV/s scan rate for the initial ten cycles as displayed in Figure 4.8 (a, b, and c). All three samples show distinctive CV curves of Li-rich cathode materials [140,145]. The first charge cycle shows two peaks. The one at ~4.0 V corresponds to the oxidation of Ni<sup>2+</sup>/Ni<sup>4+</sup> and Co<sup>3+</sup>/Co<sup>4+</sup> in the layered phase [146]. The 2<sup>nd</sup> peak at ~4.7 V is ascribed to the activation of Li<sub>2</sub>MnO<sub>3</sub>, which disappeared in subsequent cycles, indicating irreversible

removal of  $\text{Li}^+$  in the form of  $\text{Li}_2\text{O}$  from  $\text{Li}_2\text{MnO}_3$  [113,114]. The corresponding cathodic peaks of  $\text{Ni}^{4+}/\text{Ni}^{3+}$  and  $\text{Co}^{4+}/\text{Co}^{3+}$  are observed at  $\sim 4.25$  V and  $\sim 3.75$  V, respectively. Interestingly, LRACNI exhibits smaller differences between anodic and cathodic peaks of 0.27 V and 0.17 V in the 1<sup>st</sup> and 10<sup>th</sup> cycles, respectively, compared to 0.29 V and 0.23 V and 0.31 V and 0.315 V of LRAC and LRNI at the 1<sup>st</sup> and 10<sup>th</sup> cycles, respectively. This result indicates that LRACNI has significantly better reversibility than the other samples, consistent with what was explained earlier for Figure 4.5 and Figure 4.7(b). For LRAC and LRACNI, there are oxidation peaks at  $\sim 3.25$  V. These peaks gradually become more evident and shift to  $\sim 3.0$  V over cycling. This oxidation peak is mainly attributed to a lithium deintercalation process from the  $\text{Li}_2\text{MnO}_3$  layer [115,116], which explains the incomplete activation of the  $\text{Li}_2\text{MnO}_3$  layer of these samples in the first cycle. On the other hand, there is no evidence for such a peak for LRNI, suggesting that LRNI suffers from capacity fading over cycling due to the total activation of  $\text{Li}_2\text{MnO}_3$  in the first cycle. The cathodic peaks at  $\sim 3.25$  V are attributed to  $\text{Mn}^{4+/3+}$ . The appearance of the  $\sim 3.25$  V peaks in LRAC and LRACNI electrodes with noticeable developments over cycling, manifests gradual increasing of capacity of this material over cycling. These results are consistent with the cycling performances shown in Figure 4.7.

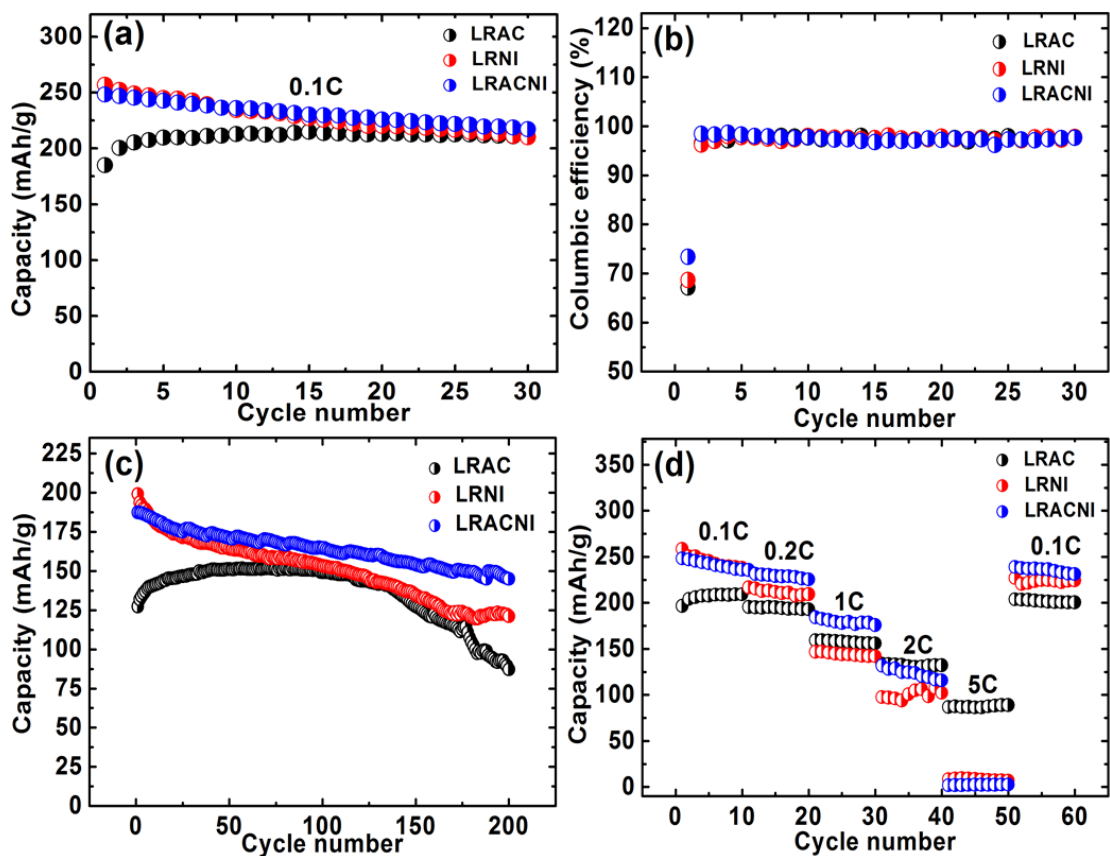


Figure 4. 7(a) Discharge capacities at 0.1C, (b) Columbic efficiency at 0.1C, (c) Discharge Capacities at 1C, and (d) Rate capability at different current densities; of LRAC, LRNI, and LRACNI between 2.0-4.8V.

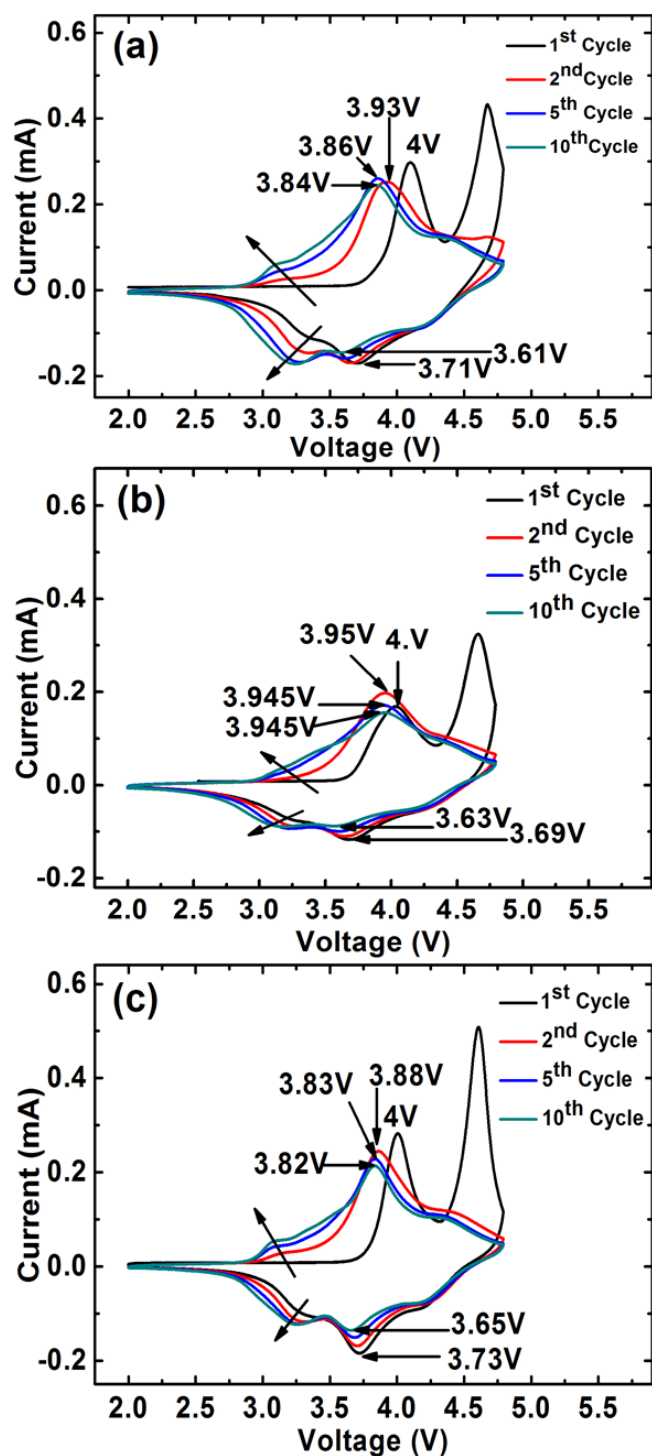


Figure 4. 8 Cycle voltammetries of (a) LRAC, (b) LRNI, and (c) LRACNI; at a scan rate of 0.1 mV/s, between 2.0 - 4.8 V.

Figure 4.9 shows the EIS spectra for LRAC, LRNI, and LRACNI electrodes after the 10<sup>th</sup> cycle in the frequency range from 0.05 Hz to 1 MHz. The measurements were

carried out in the charged state at 2.0 V and a scan rate of 0.1 mV/s. The EIS measurement is necessary to show the electrochemical, kinetic characteristic of each electrode material. The high-frequency semicircles represent the solid electrolyte interface resistance ( $R_{SEI}$ ). LRACNI shows the lowest  $R_{SEI}$  value of  $45.23\Omega$ , compared to 54.11 and  $231.79\Omega$  for LRAC and LRNI, respectively. It is clearly revealed that high surface area, associated with small particles of LRNI, gives the highest electrode-electron resistivity. It suggests that side reactions occur between the active material and the electrolyte, leading to greatly increased in interfacial resistance [100].

It can be concluded from this study that mixing 50% (in mole) acetate-based salts with the same amount of nitrate-based salts can produce an effective cathode material, LRACNI, with much-improved cycling stability due to the reduction in the interfacial, electrochemical reaction activity between the electrode and electrolytes.

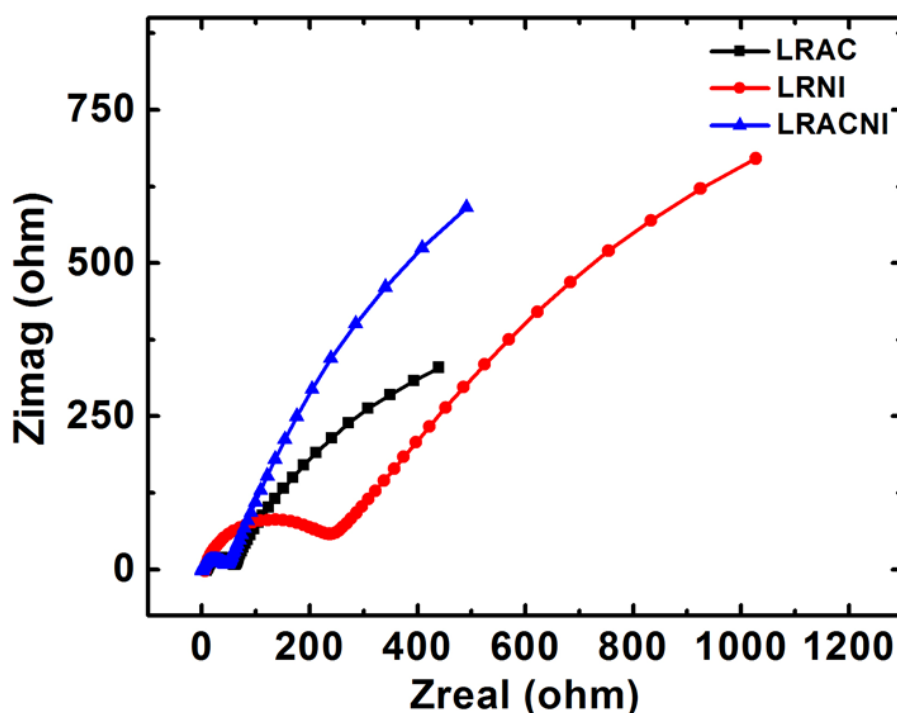


Figure 4.9 EIS spectra for LRAC, LRNI and LRACNI electrodes, after the 10<sup>th</sup> cycle.

## 4.5 Conclusion

The acetate (LRAC), nitrate (LRNI), and 50/50% (in mole) acetate/nitrate (LRACNI) based materials have been used to synthesize  $\text{Li}_{1.2} \text{Mn}_{0.51} \text{Ni}_{0.2175} \text{Co}_{0.0725} \text{O}_2$  cathode materials for a lithium-ion battery. The sol-gel method using glycerol as a solvent was effectively used as the synthesis approach in this study. The results from gel and dry powder forms (FTIR) (Figure 4.1 (a, b)), dry powder thermal analysis (TGA) (Figure 4.3), and the final crystalline synthesized powder (SEM) (Figure 4), explain the mechanism to synthesize  $\text{Li}_{1.2} \text{Mn}_{0.51} \text{Ni}_{0.2175} \text{Co}_{0.0725} \text{O}_2$  as a cathode material for lithium ion batteries using raw materials with different metallic bases. Smaller particles are produced in LRNI due to the effect of corn starch as a capping agent in this material. The formation of acetyl groups on LRAC material has restrained cornstarch from being a capping agent. Therefore, the metallic base affects the size of the resulted nanoparticles. The nanoparticle size was  $> 0.8 \mu\text{m}$ ,  $> 0.6 \mu\text{m}$ , and  $> 0.4 \mu\text{m}$  for LRAC, LRACNI, and LRNI, respectively.

Additionally, the electrochemical performance of the synthesized electrodes has been affected. Using the advantages of smaller particles, which give high initial charge/discharge capacity of LRNI, and bigger particles, which suppress the total phase change in the first cycle of LRAC, LRACNI shows a significant improvement in electrochemical performance up to 1C. Compared to 68.45 and 60.78% capacity retention of LRAC and LRNI, respectively, after 200 cycles at 1C current density and, the LRACNI electrode shows excellent capacity retention of 77.33%. Thus, LRACNI is expected to be used further to improve the structural stability of Li-rich cathode material for lithium ion batteries.



## Chapter 5. High Retention-Rate NCA Cathode Material Synthesized Using Glycerol Solvent

Khaleel I. Hamad <sup>a</sup>, and Yangchuan Xing <sup>a\*</sup>

<sup>a</sup> Department of Chemical Engineering, University of Missouri, Columbia, MO, 65211

### 5.1 Abstract

This communication reports a high retention-rate  $\text{LiNi}_{0.8}\text{Co}_{0.15}\text{Al}_{0.05}\text{O}_2$  (NCA) cathode material for Li-ion batteries synthesized with glycerol as a solvent and a reactant. Early crystallization in the NCA material at low temperatures was believed to hinder cationic mixing that would occur at higher temperatures during calcination. As a result, cycling of the NCA material shows a very stable capacity. The NCA material displays 97% capacity retention at 1C (1C = 200 mA/g) after 50 cycles, 87.6% at 0.3C after 100 cycles, and 93.6% at 0.1C after 70 cycles, which are better than those reported previously.

### 5.2 Introduction

Up to now, many synthesis approaches, such as co-precipitation[147,148], sol-gel method [149], solution combustion [150] and solid state reaction[151], have been tried to prepare the  $\text{LiNi}_{0.8}\text{Co}_{0.15}\text{Al}_{0.05}\text{O}_2$  (NCA) cathode material to be used in lithium ion batteries (LIBs). Despite all the progress made in synthesis techniques, one of the most challenging problems is still to make an NCA material stable enough for commercial-scale applications.

Sol-gel synthesis route is one of the promising techniques that has been widely used to synthesize different Li-ion cathode materials. Although most of the recent studies have

not paid much attention to the sol-gel techniques to synthesis NCA cathode materials, this synthesis approach has still been considered an efficient way to prepare nanoscale materials. Such synthesis techniques display an effective way to transform the highly soluble chemical compounds in organic solvents into chemically reactive transparent forms of hydrated oxides on hydrolysis processing [152]. These oxides show considerable stability in the solution which makes the reproducibility of the materials easy, and the final products are easily purified which in turns gives high chemical quality to the final products. However, there are still some limitations of using this technique nowadays because of the smaller secondary particle size that is produced by using water as a solvent in the sol-gel method. Our previous work with using glycerol instead of water in this regard shows a bigger particle size and better electrochemical activity compared with other proposed cathode materials [90,133].

In this communication, we report an NCA cathode material synthesized using glycerol. The glycerol is beneficial, unlike water, in forming crystalline structures at earlier stages in the synthesis, as observed in scanning electron microscopy (SEM) and X-ray diffraction (XRD). This is believed to reduce the cationic mixing during calcination at high temperatures afterword. Consequently, the produced powders show very high retention-rate during cycling.

### 5.3 Experimental

NCA powders were synthesized by using a previously developed method[90,133], in which stoichiometric amounts of Li  $(\text{CH}_3\text{COO})_2 \cdot 2\text{H}_2\text{O}$ , Ni  $(\text{CH}_3\text{COO})_2 \cdot 4\text{H}_2\text{O}$ , Co  $(\text{CH}_3\text{COO})_2 \cdot 4\text{H}_2\text{O}$ , and Al  $(\text{NO}_3)_3 \cdot 9\text{H}_2\text{O}$  were dissolved in glycerol, a deep eutectic solvent (DES) precursor, at 80 °C with stirring. The DES precursor has a metal salt to glycerol molar ratio of 1:3 ( $\text{M}^+/\text{Glycerol}$ ) and is a clear salt solution. To this DES

precursor solution, cornstarch is added as a gelling agent at the same temperature with continuous stirring with a molar ratio of 4:1 ( $M^+$ /cornstarch). The gel forms afterward and the heating temperature was increased to 400 °C to obtain a dry NCA powder. The dry powder was then pelletized and introduced to a high temperature heat treatment of 750 °C for 12 hours in air at a heating rate of 5 °C/min. The calcined powder was grounded and used for further characterization studies.

#### 5.4 Results and discussion

SEM images of the dry powder and the calcined powder are displayed in Figure 5.1. The results of the dry powder before calcination shows that there are pre-crystalline nanoparticles. The calcined powder (at 750 °C for 12 hr) show hexagonal and rectangular prism nanorod shapes with size ranging from 0.26 to 0.80  $\mu\text{m}$ .

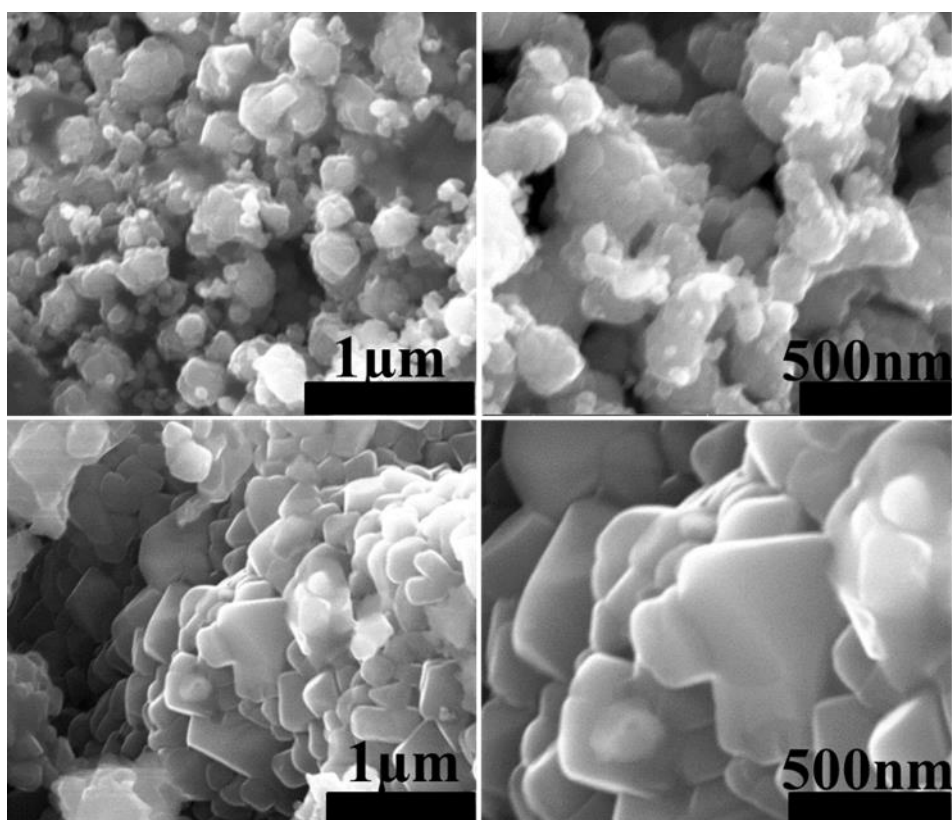


Figure 5. 1 The SEM images of the dry powder (top), and the sintered one at 750 °C/ 12hr (bottom).

Figure 5.2 (a) and (b) are the XRD patterns for both the dry powder and the calcined powder. As seen in Figure 5.2(a) clear crystalline peaks appeared at different angles, albeit they cannot be indexed at this time. In Figure 5.2(b) for the calcined powder, the diffraction peaks can be indexed to a well-defined layered structure of  $\alpha$ -NaFeO<sub>2</sub> type with a space group of R-3m.

One of the most well-known issues in the layered structure material is the cationic mixing. NCA material has 80% Ni, and as addressed in the literature, Ni<sup>2+</sup> is hard to be completely oxidized to Ni<sup>3+</sup>, which results in the presence of Ni<sup>2+</sup> in the NCA material [153,154]. The similar size in ionic radii of both Li<sup>+</sup> and Ni<sup>2+</sup> would trigger Ni<sup>2+</sup> migration to the Li layer, impeding Li<sup>+</sup> diffusion during the charge/discharge processes [155]. The intensity ratio of  $I_{(003)}/I_{(104)}$  in the layered structure was found to be related to the cationic mixing, and the value above 1.2 indicates a lower cationic mixing and vice versa [156]. The intensity ratio of 1.38 was found in our NCA material, indicating that the synthesized material has a low degree of cationic mixing. A clear hexagonal structure of the NCA material can be defined based on the distinct splitting peaks of (006)/(102) and (018)/(110).[96] These results suggest that the synthesized powder using the DES precursor has a much better cationic ordering.

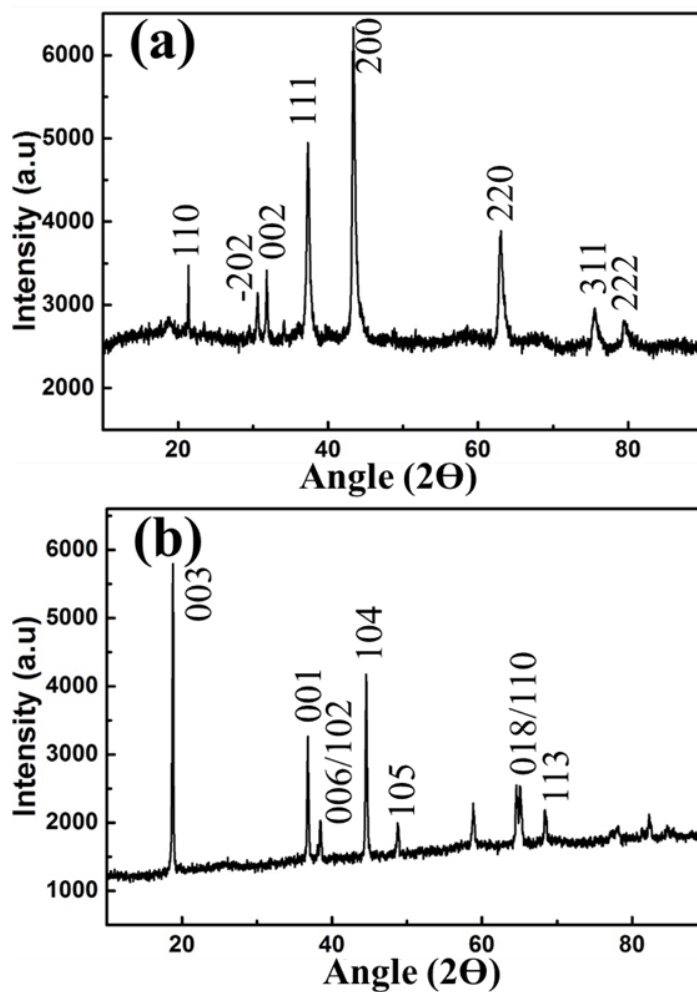


Figure 5. 2 XRD patterns for; (a) dry powder NCA (400 C), and (b) sintered powder at 750°C/ 12hr.

To demonstrate the electrochemical stability and performance, electrochemical tests are conducted in the voltage range of 2.7-4.3 V as displayed in Figure 5.3. The initial charge-discharge curves at 0.1C are presented in Figure 5.3(a). The NCA material delivers an initial discharge capacity of 174.82 mAh/g. Further tests were conducted at different rates of 0.3C and 1C for 100 cycles, as shown in Figure 5.3(b).

The results show very high capacity retention rates of 87.6% at 0.3C (163.00 mAh/g at 1<sup>st</sup> and 142.88 mAh/g at 100<sup>th</sup>) and 87.3% at 1C (131.92 mAh/g at 1<sup>st</sup> and 115.22 mAh/g at 100<sup>th</sup>). The rate capability of the cell is carried out at different current

densities and returns to the 0.1C for 70 cycles (60-120<sup>th</sup> cycle) with superior capacity retention of 93.6% as shown in Figure 5.3(c).

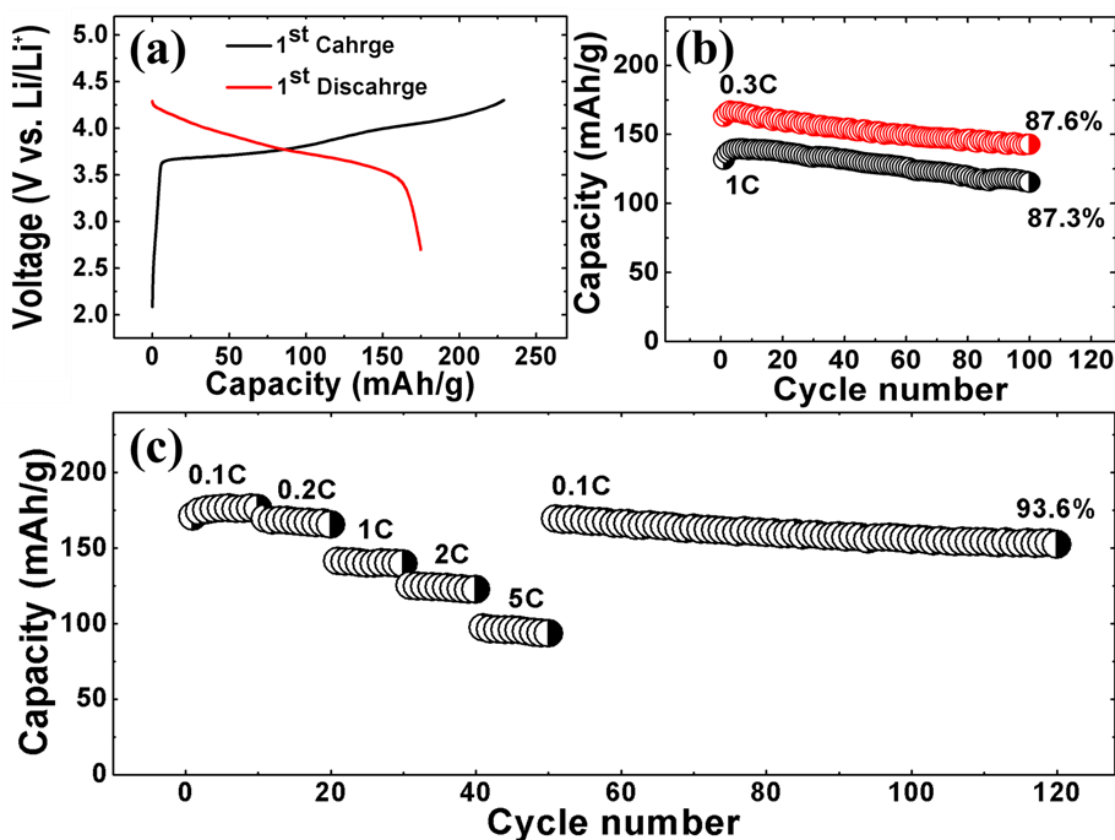


Figure 5. 3, (a) Initial charge/discharge capacity at 0.1C, (b) Discharge capacity at 0.3 and 1C, and (c) rate capability at different C-rates.

The high stability of the NCA cathode material could be attributed to the better cationic ordering of the NCA cathode material using glycerol, which diminishes cationic mixing when crystalline structures are formed at early stages in heat treatment as explained earlier. Comparing with other NCA cathode materials made using different methods, this synthesis approach using a DES precursor has shown an appreciated improvement in electrochemical performance as can be further seen in Table 5.1.

Table 5. 1 Comparison of NCA cathode material electrochemical performance with previous work.

Synthesis method	Retention Rate	Reference
Ball-milling	80.9%, 1C at 100 cycles	[157]
Co-precipitation	79.9%, 0.5C after 100cycles	[158]
Co-precipitation	86.1%, 1C at 60 cycles	[159]
Solid-state at 750 °C/24 h	77.36%, 1C at 60 cycles	[160]
Solid-state at 750 °C/24 h	92%, 1C at 60 cycles	[161]
Sol-gel at 800 °C/24 h	91%, 0.5C at 50 cycles	[149]
DES precursor at 750 °C/12 h	93.6%, 0.1C at 50-120 cycles  93.2% and 87.6%, 0.3 C at 50 and 100 cycles  97% and 87.3%, 1C at 50 and 100 cycles	This study

Figure 5.4 (a) shows the voltammograms of NCA in the potential range of 2.7-4.3V (vs. Li<sup>+</sup>/Li) for the 1<sup>st</sup>, 2<sup>nd</sup>, and the 10<sup>th</sup> cycles. There are three anodic and three cathodic peaks observed in this figure. The peaks are attributed to the phase transitions from the hexagonal phase to the monoclinic phase, the monoclinic phase to the hexagonal phase, and the hexagonal phase to the hexagonal phase during the charge/discharge processes [162–164]. The electrode polarization is minimized as it moves from the 1<sup>st</sup> cycle to the 2<sup>nd</sup> and then the 10<sup>th</sup> cycles, indicative of larger reversibility of Li<sup>+</sup> during the intercalation/ deintercalation processes [165]. Notably, the second and third oxidation peaks are more evident in the 10<sup>th</sup> cycle than the 1<sup>st</sup> and 2<sup>nd</sup> cycles. This could be attributed to the lowest cationic mixing that is associated with the highest reversibility in phase transitions [166]. Figure 5.4(b) illustrates the electrochemical impedance spectra (EIS) for the NCA cathode material at a fully discharged state of 2.7 V after the

10<sup>th</sup> cycle. The charge resistance ( $R_{ct}$ ) of the cathode material shows a very low resistance of 13.4  $\Omega$  after the 10<sup>th</sup> cycle.

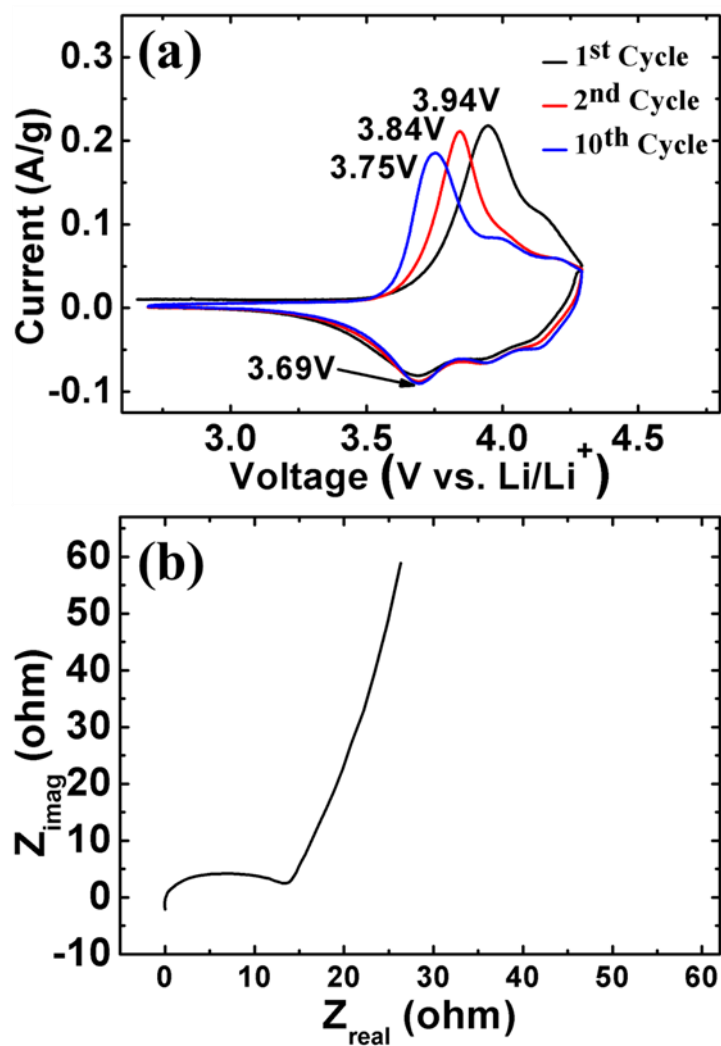


Figure 5. 4, (a) Cyclic voltammetry for the 1<sup>st</sup>, 2<sup>nd</sup> and the 10<sup>th</sup> cycles, (b) Nyquist plot after the 10<sup>th</sup> cycle; of NCA cathode material.



## 5.5 Summary

Layered NCA cathode material synthesized by using glycerol solvent was shown to have a good retention rate. The electrochemical results show 97/87.3%, 87.6/93.2% discharge capacity retention after 50/100 cycles at 1C and 1/3C, respectively in the voltage range between 2.7-4.3V. After cycling the cell at different current density for 50 cycles and going back to 0.1C discharge rate, 93.6% of the 51<sup>st</sup> discharge capacity has been retained at the end of the 120<sup>th</sup> cycle. The superior performances are ascribed to the well-ordered metal oxides with less cationic mixing and higher reversibility, which is a result of early crystallization in the NCA material synthesized using glycerol as solvent.

## 5.6 Acknowledgements

This material is based upon work partially supported by the Department of Energy, Office of Energy Efficiency and Renewable Energy (EERE), under Award Number DE-EE0007282. The authors also acknowledge partial financial support from the University of Missouri. K.I.H would like to thank the Higher Committee for Education Development in Iraq (HCED) for providing a scholarship. The authors would like to thank Dr. Eric Bohannan for his help with obtaining the XRD results.

## Chapter 6. Conclusions and future work

### 6.1 Conclusions

This study reported new, interesting results for an alternative method of using glycerol as a solvent in the sol-gel approach. Developing new techniques to produce cathode materials for lithium-ion batteries, with higher efficiency and lower energy consumption, is a worldwide interest. This is due to the increase in new energy storage devices that can reduce the demand and consumption of other energy resources like oil, which causes environmental problems. This study shows promising results in terms of economic aspects and working efficiency, by using glycerol as a solvent in the synthesis of cathode materials for lithium-ion batteries.

The first layered cathode material ( $\text{LiMn}_{1/3}\text{Ni}_{1/3}\text{Co}_{1/3}\text{O}_2$ ) was successfully synthesized. The necessary time to synthesize nanocrystalline cathodes was 8 hours, compared to 12 or more hours to synthesize the same material using water. Additionally, the sample prepared at  $900^\circ\text{C}/8$  hours shows a good crystalline structure with better cationic ordering. Moreover, an exceptional initial discharge capacity of 177.1 mAh/g at C/10, and a discharge capacity of 148.2 mAh/g after 100 cycles with 83.7% capacity retention has been achieved. Furthermore, high current density rate shows an 80.9 mAh/g discharge capacity after 50 cycles at 5C. A possible explanation for such achievement is that the higher energy released from glycerol during combustion steps helped to synthesize the material in a short time. Besides, partially crystalline nanoparticles are more likely to be produced at low temperature. So, a shorter heat treatment is required to get a fully crystalline structure. Longer heat treatment may result in blocking  $\text{Li}^+$  diffusion paths,  $\text{Ni}^{+2}$  and  $\text{Li}^+$  have almost the same ionic radius, because  $\text{Ni}^{+2}$  can move to lithium layer and substitute  $\text{Li}^+$ .

The use of such improvement in synthesizing cathode materials to modify another layered structure has been demonstrated. Lithium-rich cathode materials with the formula  $\text{Li}_{1.2} \text{Mn}_{0.51} \text{Ni}_{0.145+x} \text{Co}_{0.145-x} \text{O}_2$  ( $x=0$  (LR2), 0.0725 (LR1)) have been investigated. The results show bigger particle size in LR1 than that in LR2 cathode material. LR1 has an interesting increase in discharge capacity at 0.1C discharge rate up to the 15<sup>th</sup> cycle followed by 93.5% capacity retention up to 48<sup>th</sup> cycle. In addition, a 1C discharge rate for 100 cycles showed that LR1 capacity increased steadily from 127 mAh/g (1<sup>st</sup> discharge cycle) to 152 mAh/g (80<sup>th</sup> discharge cycle), ending at 149 mAh/g (98% capacity retention) in the 100<sup>th</sup> discharge cycle. The superior activity of the LR1 cathode material is suggested to be related to the bigger particles that can hinder the total activation of  $\text{Li}_2\text{MnO}_3$ , which is the main reason for structure transformation from layered to spinel. The study demonstrates that the use of LR1 cathode material with higher activity and less cobalt contents decreases the toxicity and the price of energy storage devices.

Li-rich cathode materials made with different metallic-based salts and cornstarch were studied further, in order to develop new Li-rich cathode materials and understand the nanoparticle formation mechanism. Cornstarch has a dual role in nanoparticle formation: a gelling agent in LR-acetate (LRAC), and a combustible fuel in LR nitrate salt-based cathode material (LRNI). Smaller particles are produced in LRNI based materials due to the role of corn starch as a capping agent in this material, while the formation of acetyls groups on LRAC material has restrained corn starch from being a capping agent. Therefore, the metallic base affects the particle size of the resultant nanoparticles. The nanoparticle size is larger in the LRAC cathode material.

Additionally, the electrochemical performance of the synthesized electrodes was affected. Using advantages of smaller particles, which give high initial

charge/discharge capacity in LRNI, and bigger particles which suppress the total phase change in the first cycle of LRAC, in one material, LRACNI, shows a significant improvement in the electrochemical performance. LRACNI exhibits a superior discharge capacity retention over 77.33% at 1C after 200 cycles. Additionally, the crystal structure of LRACNI was better, as shown by the XRD results, than the other synthesized Li-rich synthesized cathode materials.

Nowadays, Ni-rich cathode material is one of the most commercialized Li-ion battery materials. Our modified synthesis techniques showed an efficient way to improve the performance of this material. The NCA cathode material shows a significant capacity retention of up to 87% at 1C (1C = 200 mA/g) after 100 cycles, 87.6% at 0.3C after 100 cycles, and 93.6% at 0.1C after 70 cycles.

Overall, our modified way of using glycerol as a substitute for water was proven to provide more structural stability, reduce heat treatment time and energy requirements, and is useful to consistently prepare different types of Li-ion battery materials.

## 6.2 Future Work

Since glycerol has been proven to work as an excellent solvent to prepare a DES for different LIBs applications, our next goal is to improve the synthesized materials. Although the synthesized materials showed better capacity retention over cycling at different rates, improving the capacity retention for over 1000 cycles requires some kind of surface protection treatment. There are different mechanisms being reported to improve the structural stability for LIBs cathode materials, such as coating and doping. Metals oxides like  $\text{Al}_2\text{O}_3$ ,  $\text{ZnO}$ , and  $\text{Nb}_2\text{O}_5$  were used in a coating process as surface protective layers that could help prolong battery performance over cycling. There are

also some dopant materials like Mo and W that have been approved as pillars for the cathode materials. So, we can use these approved methods to enhance our materials durability over 1000 cycles.

The reason why glycerol has shown better stability over cycling compared to other solvents needs to be addressed comprehensively. Different tests on our cathode materials have to be carried out to emphasize how the preferred, lower cationic mixing has resulted. In-situ XRD is one efficient technique that has been used to characterize structural evolution and cationic mixing during cycling. High-resolution transition electron microscopy (HRTEM) is another technique that is used to visualize cationic metals in the powder. X-ray photoelectron spectroscopy (XPS) is used to measure the elemental composition of the powder after cycling. Thus, these three tests could help determine the mechanism of the cationic ordering during cycling, and ultimately on the advantage of using glycerol to synthesize LIBs cathode materials.

Finally, NCA cathode material has been identified as being sensitive to moisture. Although our NCA cathode material showed superior capacity retention compared to others, the initial discharge capacity is still unsatisfactory. Using pure oxygen during high-temperature heat treatments helps to minimize the cationic mixing. Our next goal is to improve the NCA cathode materials with initial discharge capacity to about 180 mAh/g at 1C by introducing pure oxygen during calcination at high temperatures.

## Bibliography

- [1] J.-M. Tarascon, M. Armand, *Nature* 414 (2001) 359–367.
- [2] M. Wang, *Transp. Res. Rec. J. Transp. Res. Board* 1664 (1999) 9–17.
- [3] N. Nitta, F. Wu, J.T. Lee, G. Yushin, *Mater. Today* 18 (2015) 252–264.
- [4] B. J. Landi, M. J. Ganter, C. D. Cress, R. A. DiLeo, R. P. Raffaele, *Energy Environ. Sci.* 2 (2009) 638–654.
- [5] P.W. Gruber, P.A. Medina, G.A. Keoleian, S.E. Kesler, M.P. Everson, T.J. Wallington, *J. Ind. Ecol.* 15 (2011) 760–775.
- [6] J. Speirs, M. Contestabile, Y. Houari, R. Gross, *Renew. Sustain. Energy Rev.* 35 (2014) 183–193.
- [7] M.S. Whittingham, *Chem. Rev.* 104 (2004) 4271–4302.
- [8] J. Gao, S.-Q. Shi, H. Li, *Chin. Phys. B* 25 (2016) 018210.
- [9] D. Guyomard, 9 (2000).
- [10] A. Du Pasquier, I. Plitz, S. Menocal, G. Amatucci, *J. Power Sources* 115 (2003) 171–178.
- [11] A. Rougier, P. Gravereau, C. Delmas, *J. Electrochem. Soc.* 143 (1996) 1168–1175.
- [12] H. Arai, S. Okada, Y. Sakurai, J. Yamaki, *Solid State Ion.* 109 (1998) 295–302.
- [13] M. Gu, I. Belharouak, J. Zheng, H. Wu, J. Xiao, A. Genc, K. Amine, S. Thevuthasan, D.R. Baer, J.-G. Zhang, N.D. Browning, J. Liu, C. Wang, *ACS Nano* 7 (2012) 760–767.
- [14] J. Tu, X.B. Zhao, G.S. Cao, D.G. Zhuang, T.J. Zhu, J.P. Tu, *Electrochimica Acta* 51 (2006) 6456–6462.
- [15] M. Wohlfahrt-Mehrens, C. Vogler, J. Garche, *J. Power Sources* 127 (2004) 58–64.
- [16] N. Lebedeva, F.D. Persio, L. Boon-Brett, (n.d.) 80.

- [17] K. Kam, M. Doeff, *Mater. Matters* 7 (2012) 56–60.
- [18] P. Rozier, J.M. Tarascon, *J. Electrochem. Soc.* 162 (2015) A2490–A2499.
- [19] P. Strobel, B. Lambert-Andron, *J. Solid State Chem.* 75 (1988) 90–98.
- [20] J.-S. Kim, C.S. Johnson, J.T. Vaughey, M.M. Thackeray, S.A. Hackney, W. Yoon, C.P. Grey, *Chem. Mater.* 16 (2004) 1996–2006.
- [21] Y.S. Meng, G. Ceder, C.P. Grey, W.-S. Yoon, M. Jiang, J. Bréger, Y. Shao-Horn, *Chem. Mater.* 17 (2005) 2386–2394.
- [22] J. Bréger, M. Jiang, N. Dupré, Y.S. Meng, Y. Shao-Horn, G. Ceder, C.P. Grey, *J. Solid State Chem.* 178 (2005) 2575–2585.
- [23] P. Kalyani, S. Chitra, T. Mohan, S. Gopukumar, *J. Power Sources* 80 (1999) 103–106.
- [24] H.-J. Noh, S. Youn, C.S. Yoon, Y.-K. Sun, *J. Power Sources* 233 (2013) 121–130.
- [25] Y. Talyosef, B. Markovsky, R. Lavi, G. Salitra, D. Aurbach, D. Kovacheva, M. Gorova, E. Zhecheva, R. Stoyanova, *J. Electrochem. Soc.* 154 (2007) A682–A691.
- [26] R. Santhanam, B. Rambabu, *J. Power Sources* 195 (2010) 4313–4317.
- [27] N. Bensalah, H. Dawood, (2016).
- [28] Z.-D. Huang, X.-M. Liu, S.-W. Oh, B. Zhang, P.-C. Ma, J.-K. Kim, *J. Mater. Chem.* 21 (2011) 10777–10784.
- [29] X.-M. Liu, W.-L. Gao, B.-M. Ji, *J. Sol-Gel Sci. Technol.* 61 (2012) 56–61.
- [30] P. He, H. Wang, L. Qi, T. Osaka, *J. Power Sources* 160 (2006) 627–632.
- [31] K.M. Shaju, G.V. Subba Rao, B.V.R. Chowdari, *Electrochimica Acta* 48 (2002) 145–151.
- [32] T.H. Cho, S.M. Park, M. Yoshio, T. Hirai, Y. Hideshima, *J. Power Sources* 142 (2005) 306–312.

- [33] G.T.-K. Fey, C.-S. Chang, T.P. Kumar, *J. Solid State Electrochem.* 14 (2010) 17.
- [34] C.J. Brinker, G.W. Scherer, *Sol-Gel Science: The Physics and Chemistry of Sol-Gel Processing*, Academic Press, 2013.
- [35] B. Scrosati, *Nature* 373 (1995) 557–558.
- [36] T. Ohzuku, Y. Makimura, *Chem. Lett.* 30 (2001) 642–643.
- [37] J.K. Ngala, N.A. Chernova, M. Ma, M. Mamak, P.Y. Zavalij, M.S. Whittingham, *J. Mater. Chem.* 14 (2004) 214–220.
- [38] T. Ohzuku, Y. Makimura, *Chem. Lett.* 30 (2001) 744–745.
- [39] N.N. Sinha, N. Munichandraiah, *ACS Appl. Mater. Interfaces* 1 (2009) 1241–1249.
- [40] W. Luo, X. Li, J.R. Dahn, *Chem. Mater.* 22 (2010) 5065–5073.
- [41] F. Wu, M. Wang, Y. Su, S. Chen, *J. Power Sources* 189 (2009) 743–747.
- [42] S. Yang, Y. Song, K. Ngala, P.Y. Zavalij, M. Stanley Whittingham, *J. Power Sources* 119–121 (2003) 239–246.
- [43] Z.-D. Huang, X.-M. Liu, S.-W. Oh, B. Zhang, P.-C. Ma, J.-K. Kim, *J. Mater. Chem.* 21 (2011) 10777–10784.
- [44] C. Zhang, P. Yang, X. Dai, X. Xiong, J. Zhan, Y. Zhang, *Trans. Nonferrous Met. Soc. China* 19 (2009) 635–641.
- [45] J. Guo, L.F. Jiao, H. Yuan, L.Q. Wang, H.X. Li, M. Zhang, Y.M. Wang, *Electrochimica Acta* 51 (2006) 6275–6280.
- [46] L. Lacerda, M. da Silva Carvalho Filho, I. Demiate, G. Bannach, M. Ionashiro, E. Schnitzler, *J. Therm. Anal. Calorim.* 93 (2008) 445–449.
- [47] M.E. Gomes, V.I. Sikavitsas, E. Behraves, R.L. Reis, A.G. Mikos, *J. Biomed. Mater. Res. A* 67A (2003) 87–95.



- [48] Gangulibabu, D. Bhuvaneshwari, N. Kalaiselvi, N. Jayaprakash, P. Periasamy, J. Sol-Gel Sci. Technol. 49 (2009) 137–144.
- [49] J. Wang, X. Yao, X. Zhou, Z. Liu, J. Mater. Chem. 21 (2011) 2544–2549.
- [50] Y. Idemoto, T. Matsui, Solid State Ion. 179 (2008) 625–635.
- [51] P. Reale, D. Privitera, S. Panero, B. Scrosati, Solid State Ion. 178 (2007) 1390–1397.
- [52] L.Q. Wang, L.F. Jiao, H. Yuan, J. Guo, M. Zhao, H.X. Li, Y.M. Wang, J. Power Sources 162 (2006) 1367–1372.
- [53] J.M. Paulsen, C.L. Thomas, J.R. Dahn, J. Electrochem. Soc. 147 (2000) 861–868.
- [54] J.P. Peres, C. Delmas, A. Rougier, M. Broussely, F. Perton, P. Biensan, P. Willmann, J. Phys. Chem. Solids 57 (1996) 1057–1060.
- [55] C.-H. Lu, T.-Y. Wu, H.-C. Wu, M.-H. Yang, Z.-Z. Guo, I. Taniguchi, Mater. Chem. Phys. 112 (2008) 115–119.
- [56] M. Sathiya, A.S. Prakash, K. Ramesha, A.K. Shukla, Mater. Res. Bull. 44 (2009) 1990–1994.
- [57] H. Xia, H. Wang, W. Xiao, L. Lu, M.O. Lai, J. Alloys Compd. 480 (2009) 696–701.
- [58] M. Jo, Y.-S. Hong, J. Choo, J. Cho, J. Electrochem. Soc. 156 (2009) A430–A434.
- [59] J.C. Arrebola, A. Caballero, L. Hernán, J. Morales, J. Power Sources 180 (2008) 852–858.
- [60] T.J. Patey, R. Büchel, M. Nakayama, P. Novák, Phys. Chem. Chem. Phys. 11 (2009) 3756–3761.
- [61] L. Zhang, X. Wang, T. Muta, D. Li, H. Noguchi, M. Yoshio, R. Ma, K. Takada, T. Sasaki, J. Power Sources 162 (2006) 629–635.

- [62] S.J. An, J. Li, C. Daniel, D. Mohanty, S. Nagpure, D.L. Wood, *Carbon* 105 (2016) 52–76.
- [63] Y. Xu, Q. Liu, Y. Zhu, Y. Liu, A. Langrock, M.R. Zachariah, C. Wang, *Nano Lett.* 13 (2013) 470–474.
- [64] W. Meng, *Int. J. Mater. Sci. Appl.* 5 (2016) 136.
- [65] G. Babu, N. Kalaiselvi, D. Bhuvaneshwari, *J. Electron. Mater.* 43 (2014) 1062–1070.
- [66] Gangulibabu, D. Bhuvaneshwari, N. Kalaiselvi, *J. Solid State Electrochem.* 17 (2013) 9–17.
- [67] S.J. Shi, J.P. Tu, Y.J. Mai, Y.Q. Zhang, Y.Y. Tang, X.L. Wang, *Electrochimica Acta* 83 (2012) 105–112.
- [68] K. Mizushima, P.C. Jones, P.J. Wiseman, J.B. Goodenough, *Mat Res Bull* 15 (1980) 783–789.
- [69] S. Patoux, M.M. Doeff, *Electrochem. Commun.* 6 (2004) 767–772.
- [70] L. Tan, H. Liu, *Solid State Ion.* 181 (2010) 1530–1533.
- [71] Y.-S. He, Z.-F. Ma, X.-Z. Liao, Y. Jiang, *J. Power Sources* 163 (2007) 1053–1058.
- [72] S. Kim, W. Cho, X. Zhang, Y. Oshima, J.W. Choi, *Nat. Commun.* 7 (2016) 13598.
- [73] M. M. Thackeray, C. S. Johnson, J. T. Vaughey, N. Li, S. A. Hackney, *J. Mater. Chem.* 15 (2005) 2257–2267.
- [74] C.S. Johnson, N. Li, C. Lefief, M.M. Thackeray, *Electrochem. Commun.* 9 (2007) 787–795.
- [75] C.S. Johnson, J.-S. Kim, C. Lefief, N. Li, J.T. Vaughey, M.M. Thackeray, *Electrochem. Commun.* 6 (2004) 1085–1091.
- [76] Z. Lu, J.R. Dahn, *J. Electrochem. Soc.* 149 (2002) A815–A822.

- [77] A.R. Armstrong, M. Holzapfel, P. Novák, C.S. Johnson, S.-H. Kang, M.M. Thackeray, P.G. Bruce, *J. Am. Chem. Soc.* 128 (2006) 8694–8698.
- [78] D. Mohanty, S. Kalnaus, R.A. Meisner, K.J. Rhodes, J. Li, E.A. Payzant, D.L. Wood, C. Daniel, *J. Power Sources* 229 (2013) 239–248.
- [79] M. M. Thackeray, S.-H. Kang, C. S. Johnson, J. T. Vaughey, R. Benedek, S. A. Hackney, *J. Mater. Chem.* 17 (2007) 3112–3125.
- [80] R. Wang, X. He, L. He, F. Wang, R. Xiao, L. Gu, H. Li, L. Chen, *Adv. Energy Mater.* 3 (2013) 1358–1367.
- [81] H. Yu, H. Zhou, *J. Phys. Chem. Lett.* 4 (2013) 1268–1280.
- [82] K. Ozawa, Y. Nakao, T. Mochiku, Z. Cheng, L. Wang, H. Iwai, Y. Tsuchiya, H. Fujii, N. Igawa, *J. Electrochem. Soc.* 159 (2012) A300–A304.
- [83] C. Ban, Z. Wu, D.T. Gillaspie, L. Chen, Y. Yan, J.L. Blackburn, A.C. Dillon, *Adv. Mater.* 22 (2010) E145–E149.
- [84] S. Laruelle, S. Grugeon, P. Poizot, M. Dollé, L. Dupont, J.-M. Tarascon, *J. Electrochem. Soc.* 149 (2002) A627–A634.
- [85] J. Hong, D.-H. Seo, S.-W. Kim, H. Gwon, S.-T. Oh, K. Kang, *J. Mater. Chem.* 20 (2010) 10179–10186.
- [86] J.-M. Kim, S. Tsuruta, N. Kumagai, *Electrochem. Commun.* 9 (2007) 103–108.
- [87] E.-S. Lee, A. Huq, H.-Y. Chang, A. Manthiram, *Chem. Mater.* 24 (2012) 600–612.
- [88] J. Cabana, S.-H. Kang, C.S. Johnson, M.M. Thackeray, C.P. Grey, *J. Electrochem. Soc.* 156 (2009) A730–A736.
- [89] S.-H. Yu, T. Yoon, J. Mun, S. Park, Y.-S. Kang, J.-H. Park, S.M. Oh, Y.-E. Sung, *J. Mater. Chem. A* 1 (2013) 2833–2839.
- [90] Hamad Khaleel I., Liao Jin-Yun, Smith Taylor W., Xing Yangchuan, *Energy Technol.* 6 (2017) 710–717.

- [91] K. Park, J.-H. Park, S.-G. Hong, B. Choi, S. Heo, S.-W. Seo, K. Min, J.-H. Park, *Sci. Rep.* 7 (2017) 44557.
- [92] K.S. Yoo, Y.H. Kang, K.R. Im, C.-S. Kim, *Materials* 10 (2017) 1273.
- [93] A.D. Robertson, P.G. Bruce, *Chem. Mater.* 15 (2003) 1984–1992.
- [94] W.-S. Yoon, S. Iannopollo, C.P. Grey, D. Carlier, J. Gorman, J. Reed, G. Ceder, *Electrochem. Solid-State Lett.* 7 (2004) A167–A171.
- [95] J. Gao, A. Manthiram, *J. Power Sources* 191 (2009) 644–647.
- [96] Z. Lu, L.Y. Beaulieu, R.A. Donaberger, C.L. Thomas, J.R. Dahn, *J. Electrochem. Soc.* 149 (2002) A778–A791.
- [97] D. Wang, Y. Huang, Z. Huo, L. Chen, *Electrochimica Acta* 107 (2013) 461–466.
- [98] J. Katana Ngala, N. A. Chernova, M. Ma, M. Mamak, P. Y. Zavalij, M. Stanley Whittingham, *J. Mater. Chem.* 14 (2004) 214–220.
- [99] Z. Ma, G. Shao, Y. Fan, G. Wang, J. Song, T. Liu, *ACS Appl. Mater. Interfaces* 6 (2014) 9236–9244.
- [100] J.M. Zheng, X.B. Wu, Y. Yang, *Electrochimica Acta* 56 (2011) 3071–3078.
- [101] T.A. Arunkumar, Y. Wu, A. Manthiram, *Chem. Mater.* 19 (2007) 3067–3073.
- [102] Y.J. Park, Y.-S. Hong, X. Wu, M.G. Kim, K.S. Ryu, S.H. Chang, *J. Electrochem. Soc.* 151 (2004) A720–A727.
- [103] B. Song, M.O. Lai, L. Lu, *Electrochimica Acta* 80 (2012) 187–195.
- [104] C. Fu, G. Li, D. Luo, J. Zheng, L. Li, *J. Mater. Chem. A* 2 (2014) 1471–1483.
- [105] Z.Q. Deng, A. Manthiram, *J. Phys. Chem. C* 115 (2011) 7097–7103.
- [106] R.V. Chebiam, A.M. Kannan, F. Prado, A. Manthiram, *Electrochem. Commun.* 3 (2001) 624–627.
- [107] S. Venkatraman, Y. Shin, A. Manthiram, *Electrochem. Solid-State Lett.* 6 (2003) A9–A12.

- [108] J.M. Zheng, X.B. Wu, Y. Yang, *Electrochimica Acta* 56 (2011) 3071–3078.
- [109] Y. Jin, Y. Xu, L. Xiong, X. Sun, L. Li, L. Li, *Solid State Ion.* 310 (2017) 62–70.
- [110] L. Zhou, J. Liu, L. Huang, N. Jiang, Q. Zheng, D. Lin, *J. Solid State Electrochem.* 21 (2017) 3467–3477.
- [111] B. Xu, C. R. Fell, M. Chi, Y. Shirley Meng, *Energy Environ. Sci.* 4 (2011) 2223–2233.
- [112] H. Chen, Q. Hu, W. Peng, H. Guo, G. Yan, X. Wu, *Ceram. Int.* 43 (2017) 10919–10926.
- [113] H. Koga, L. Croguennec, M. Ménétrier, K. Douhil, S. Belin, L. Bourgeois, E. Suard, F. Weill, C. Delmas, *J. Electrochem. Soc.* 160 (2013) A786–A792.
- [114] A. Boulineau, L. Simonin, J.-F. Colin, C. Bourbon, S. Patoux, *Nano Lett.* 13 (2013) 3857–3863.
- [115] N. Yabuuchi, K. Yoshii, S.-T. Myung, I. Nakai, S. Komaba, *J. Am. Chem. Soc.* 133 (2011) 4404–4419.
- [116] J.M. Zheng, Z.R. Zhang, X.B. Wu, Z.X. Dong, Z. Zhu, Y. Yang, *J. Electrochem. Soc.* 155 (2008) A775–A782.
- [117] J.B. Goodenough, Y. Kim, *Chem. Mater.* 22 (2010) 587–603.
- [118] V. Etacheri, R. Marom, R. Elazari, G. Salitra, D. Aurbach, *Energy Environ. Sci.* 4 (2011) 3243–3262.
- [119] Y. Nishi, *Chem. Rec.* 1 (2001) 406–413.
- [120] J.B. Goodenough, K.-S. Park, *J. Am. Chem. Soc.* 135 (2013) 1167–1176.
- [121] B. Xu, D. Qian, Z. Wang, Y.S. Meng, *Mater. Sci. Eng. R Rep.* 73 (2012) 51–65.
- [122] J. Xu, S. Dou, H. Liu, L. Dai, *Nano Energy* 2 (2013) 439–442.
- [123] A. Ito, D. Li, Y. Ohsawa, Y. Sato, *J. Power Sources* 183 (2008) 344–346.

- [124] C.S. Johnson, J.-S. Kim, C. Lefief, N. Li, J.T. Vaughey, M.M. Thackeray, *Electrochem. Commun.* 6 (2004) 1085–1091.
- [125] H. Yu, Y. Wang, D. Asakura, E. Hosono, T. Zhang, H. Zhou, *RSC Adv.* 2 (2012) 8797–8807.
- [126] H. Z. Zhang, Q. Q. Qiao, G. R. Li, S. H. Ye, X. P. Gao, *J. Mater. Chem.* 22 (2012) 13104–13109.
- [127] S.-H. Kang, P. Kempgens, S. Greenbaum, A. J. Kropf, K. Amine, M. M. Thackeray, *J. Mater. Chem.* 17 (2007) 2069–2077.
- [128] A. Manthiram, J.C. Knight, S.-T. Myung, S.-M. Oh, Y.-K. Sun, *Adv. Energy Mater.* 6 (2016) n/a-n/a.
- [129] X. Liu, T. Huang, A. Yu, *Electrochimica Acta* 163 (2015) 82–92.
- [130] C. Lu, H. Wu, Y. Zhang, H. Liu, B. Chen, N. Wu, S. Wang, *J. Power Sources* 267 (2014) 682–691.
- [131] D. Wang, I. Belharouak, L.H. Ortega, X. Zhang, R. Xu, D. Zhou, G. Zhou, K. Amine, *J. Power Sources* 274 (2015) 451–457.
- [132] F. Fu, Y.-P. Deng, C.-H. Shen, G.-L. Xu, X.-X. Peng, Q. Wang, Y.-F. Xu, J.-C. Fang, L. Huang, S.-G. Sun, *Electrochem. Commun.* 44 (2014) 54–58.
- [133] K.I. Hamad, Y. Xing, *J. Electrochem. Soc.* 165 (2018) A2470–A2475.
- [134] J. Hong, D.-H. Seo, S.-W. Kim, H. Gwon, S.-T. Oh, K. Kang, *J. Mater. Chem.* 20 (2010) 10179–10186.
- [135] J. Guan, M.A. Hanna, *Biomacromolecules* 5 (2004) 2329–2339.
- [136] P. Kalyani, N. Kalaiselvi, N. Muniyandi, *J. Power Sources* 111 (2002) 232–238.
- [137] Y.X. Wang, K.H. Shang, W. He, X.P. Ai, Y.L. Cao, H.X. Yang, *ACS Appl. Mater. Interfaces* 7 (2015) 13014–13021.
- [138] J. Zheng, X. Wu, Y. Yang, *Electrochimica Acta* 105 (2013) 200–208.

- [139] G. Xu, Q. Xue, J. Li, Z. Li, X. Li, T. Yu, J. Li, X. Wang, F. Kang, *Solid State Ion.* 293 (2016) 7–12.
- [140] W. He, D. Yuan, J. Qian, X. Ai, H. Yang, Y. Cao, *J. Mater. Chem. A* 1 (2013) 11397–11403.
- [141] X. Liu, J. Liu, T. Huang, A. Yu, *Electrochimica Acta* 109 (2013) 52–58.
- [142] B. Song, Z. Liu, M. On Lai, L. Lu, *Phys. Chem. Chem. Phys.* 14 (2012) 12875–12883.
- [143] J. Kim, P. Fulmer, A. Manthiram, *Mater. Res. Bull.* 34 (1999) 571–579.
- [144] M. Chen, D. Chen, Y. Liao, X. Zhong, W. Li, Y. Zhang, *ACS Appl. Mater. Interfaces* 8 (2016) 4575–4584.
- [145] Y.X. Wang, K.H. Shang, W. He, X.P. Ai, Y.L. Cao, H.X. Yang, *ACS Appl. Mater. Interfaces* 7 (2015) 13014–13021.
- [146] B. Song, M.O. Lai, L. Lu, *Electrochimica Acta* 80 (2012) 187–195.
- [147] W.M. Liu, G.R. Hu, Z.D. Peng, K. Du, Y.B. Cao, Q. Liu, *Chin. Chem. Lett.* 22 (2011) 1099–1102.
- [148] N. Wu, H. Wu, W. Yuan, S. Liu, J. Liao, Y. Zhang, *J. Mater. Chem. A* 3 (2015) 13648–13652.
- [149] C.J. Han, J.H. Yoon, W.I. Cho, H. Jang, *J. Power Sources* 136 (2004) 132–138.
- [150] S.B. Majumder, S. Nieto, R.S. Katiyar, *J. Power Sources* 154 (2006) 262–267.
- [151] S. Xia, Y. Zhang, P. Dong, Y. Zhang, *Eur. Phys. J. - Appl. Phys.* 65 (2014).
- [152] S. Sakka, H. Kozuka, *Handbook of Sol-Gel Science and Technology. 1. Sol-Gel Processing*, Springer Science & Business Media, 2005.
- [153] X. Li, Z. Xie, W. Liu, W. Ge, H. Wang, M. Qu, *Electrochimica Acta* 174 (2015) 1122–1130.

- [154] C. Hua, K. Du, C. Tan, Z. Peng, Y. Cao, G. Hu, J. Alloys Compd. 614 (2014) 264–270.
- [155] V. Bianchi, D. Caurant, N. Baffier, C. Belhomme, E. Chappel, G. Chouteau, S. Bach, J.P. Pereira-Ramos, A. Sulpice, P. Wilmann, Solid State Ion. 140 (2001) 1–17.
- [156] L. Tan, H. Liu, Solid State Ion. 181 (2010) 1530–1533.
- [157] Y. Li, H. Yu, Y. Hu, H. Jiang, C. Li, J. Energy Chem. 27 (2018) 559–564.
- [158] G. Wu, Y. Zhou, J. Energy Chem. 28 (2019) 151–159.
- [159] L. Tian, K. Liang, X. Wen, K. Shi, J. Zheng, J. Electroanal. Chem. 812 (2018) 22–27.
- [160] S. Xia, F. Li, F. Chen, H. Guo, J. Alloys Compd. 731 (2018) 428–436.
- [161] Z. Qiu, Y. Zhang, P. Dong, S. Xia, Y. Yao, Solid State Ion. 307 (2017) 73–78.
- [162] S.N. Lim, W. Ahn, S.-H. Yeon, S.B. Park, Electrochimica Acta 136 (2014) 1–9.
- [163] Y. Kojima, S. Muto, K. Tatsumi, H. Kondo, H. Oka, K. Horibuchi, Y. Ukyo, J. Power Sources 196 (2011) 7721–7727.
- [164] S.H. Oh, S.M. Lee, W.I. Cho, B.W. Cho, Electrochimica Acta 51 (2006) 3637–3644.
- [165] X. Xiong, D. Ding, Z. Wang, B. Huang, H. Guo, X. Li, J. Solid State Electrochem. 18 (2014) 2619–2624.
- [166] T.-J. Park, J.-B. Lim, J.-T. Son, Bull. Korean Chem. Soc. 35 (2014) 357–364.



## VITA

Khaleel Idan Hamad was born on November 10, 1982 in Salahaddin, Iraq. He graduated from the University of Tikrit in July 2004 with a Bachelor of Science Degree in Chemical Engineering. He then attended the graduate school at the University of Tikrit under the guidance of Dr. Abdulkahar AL-Samarraiee pursuing a Master of Science degree, and graduated in July 2012. He then attended graduate school at the University of Missouri under the guidance of Professor Yangchuan Xing. He completed the requirements for a Doctor of Philosophy in Chemical Engineering at the University of Missouri in July 2019.